1992

Low Temperature Spectroscopic and Annealing Studies of Disordered Organic Solids

Dwayne L. LaBrake
Loyola University Chicago

LOW TEMPERATURE SPECTROSCOPIC AND ANNEALING STUDIES OF

DISORDERED ORGANIC SOLIDS

by

Dwayne L. LaBrake

A Dissertation Submitted to the Faculty of the Graduate

School of Loyola University of Chicago in Partial Fulfillment

of the Requirements for the Degree of

Doctor of Philosophy

January 1992

ACKNOWLEDGMENT

LIST OF FIGURES

LIST OF ABBREVIATIONS

α	Dispersion parameter of model II
BZP	Benzophenone
$BZP\text{-}d_{10}$	Deuterated benzophenone
C	Acceptor mole fraction
E_{max}	Energy of maximum intensity of the 0-0 vibrational band of an emitting specie
FWHM	Full width half maximum
$I_{0\text{-}2}/I_{0\text{-}0}$	Intensity of the 0-2 vibrational band relative to the 0-0 vibrational band of benzophenone
$I_{NAP}/(I_{BZP}+I_{NAP})$	Intensity of the naphthalene 0-0 vibrational band divided by the sum of the benzophenone 0-1 vibrational band intensity with naphthalene 0-0 vibrational band intensity
I_{tot}	Total integrated intensity of the BZP spectrum in the range 25,000 to 18,181 cm^{-1}
k	Natural decay rate
k_0	Average radiative decay rate of model I
<n>	Average number of sites visited by an exciton defining the average transfer domain size
NAP	Naphthalene
σ	Variance of the radiative decay rates of model I

TABLE OF CONTENTS

CHAPTER I

INTRODUCTION

Crystallization processes have been investigated for many years.[2,3,14,25,26]   These investigations have been primarily concerned with the thermodynamic and transport properties material to the ordered assembly of large numbers of molecules at defect sites. Bulk processes such as these appear to be fairly well understood. However, microscopic interactions operative during crystal growth are not well understood. This is exemplified by the fact that few correlations have been made between the structure of crystals and the structure of constituent molecules.

This thesis focuses attention on some of the microscopic processes operative during crystallization by way of annealing and spectroscopic studies of low temperature films. It is motivated by the fact that microscopic interactions play critical roles during crystallization.

In this project, experiments were directed at microscopic processes involved in the crystallization of a specific system. To this end, organic molecules were vapor quenched thereby forming an amorphous solid at low temperature. Cyclic-annealing and optical emission spectroscopic studies were conducted in order to examine precisely how the system

passes from the amorphous to crystalline phase space.

Several reasons exist for choosing optical emission spectroscopy for this project. A particularly important reason is that optical emission spectroscopy is an extremely sensitive technique for probing the microscopic interactions, dynamics and changes thereof in the condensed phase. This is largely due to the extreme sensitivity of exciton transport to small variations in condensed phase structure. Energy transport phenomena have been established as diagnostic of small energetic and structural changes among organic molecules in the condensed phase.[18,19,20-22,50]

Low temperature optical emission spectroscopy is suitable for this project in a number of respects. Low temperature simplifies spectroscopic observables by minimizing the population of lattice vibrations. In addition, low temperatures enable the preservation and manipulation of unstable, disordered molecular systems. This enhances the ability to control their crystallization process through the use of cyclic-annealing.

This project makes extensive use of optical emission spectroscopy and cyclic-annealing techniques at low temperatures in order to investigate a specific case of molecules passing from amorphous phase space to crystalline phase space. Specifically described are investigations concerning the crystallization of a select molecular system and methods by which its crystallization were examined. The

aromatic compounds, specifically benzophenone (BZP), benzophenone-d_{10} (BZP-d_{10}) and mixtures of naphthalene (NAP) and BZP were the molecular systems chosen for this study. Single crystalles composed of these molecules have been well characterized [12,17,23,52]. Disordered forms have also received some attention [24,40,42,44]. Experiments with BZP-d_{10} included in this thesis were selected to determine the sensitivity of crystallization to isotopic substitution. Experiments with mixtures of NAP/BZP were included in this thesis to examine the importance of local environment on crystallization. All of these systems were prepared in the amorphous phase using vapor-quench techniques at low temperature. Cyclic-annealing was carried out in a sequential manner to progressively higher temperatures. These sequences led the passage of these systems to the crystalline state in a step wise manner. Emission spectra, radiative decay and light scattering measurements were carried out usually at the same temperature following the quench process and each cyclic-annealing event. Spectroscopic and energy transport properties were analyzed directly from spectra or through modeling radiative decay measurements. Radiative decay curves were modeled using two complementary models. These data served to develop a picture of the microscopic processes which took place during the crystallization of BZP.

Experimental and theoretical strategies similar to those implemented in this project have been used previously by other

researchers.[18-22,27-29,36,44,49-51]   However, the combination of techniques directed precisely at crystallization processes at a microscopic level are believed to be new. The experimental and theoretical techniques of this thesis are general with regard to molecular solids and can therefore be applied to a diverse number of molecular systems.   This belief then suggests the two important contributions of this thesis work: (1) New knowledge concerning the microscopic processes involved in the crystallization of BZP.   (2) Development of methods which can be used to study the crystallization of a large variety of molecules.

Chapter   II   describes   annealing   and   spectroscopic experiments.   Chapter III presents experimental results. Chapter IV develops two models used to understand radiative decay curves. The results of fitting the model equations to decay curves are also presented.   Chapter V discusses the experimental results and how they relate to the microscopic processes involved in the crystallization of BZP.

CHAPTER II

EXPERIMENTAL PROCEDURES AND COMPONENTS

A. *EXPERIMENTAL OVERVIEW*

This thesis attempts to enhance understanding of the intrinsic microscopic processes which occur during the crystallization of BZP. To this end vapor quenched films of BZP, BZP-d_{10} and NAP/BZP mixtures were prepared at low temperatures. This required specialized vacuum and cryogenic equipment. Passage of these molecular films to the crystalline state was directed using cyclic annealing techniques. This required a specific type of temperature controller. The sequential probing of the effects of each annealing cycle was accomplished using optical emission spectroscopy. This required the use of several types of excitation sources and sensitive optical detection equipment. The data were recorded subsequent to each annealing cycle in the form of emission spectra, light scattering intensity and radiative decay profiles.

The following observables were extracted directly from the emission spectra recorded at the same temperature, (18 K) as a function of annealing temperature: the energy of maximum

intensity (E_{max}) of the 0-0 band, the full width at half maximum (FWHM) of the 0-0 band, the intensity distribution as indicated by the intensity of the 0-2 band relative to that of the 0-0 band (I_{0-2}/I_{0-0}), and the total integrated intensity in the range 25,000 to 18,181 cm^{-1} (I_{tot}). All of these parameters were observed to change with annealing. They are related to alterations in microscopic condensed phase structure, and in turn, the interactions between constituent molecules. The functionality of the data with annealing temperature provides information on how crystallization occurs at a microscopic level.

Light scattering by the samples was examined. Radiative decay measurements were analyzed using two models, the parameters of which also correlate with the crystallization of BZP when plotted as functions of annealing temperature. The development and significance of the parameters is presented in Chapter 4.

Analysis of these data required the use of computers, especially for the analysis of radiative decay curves where nonlinear regression analysis was required.

This chapter describes in detail how the molecular compounds were obtained, how the sequential annealing cycles were implemented, and what spectroscopic measurements were involved following each annealing cycle. In addition, the construction of the specialized equipment used in this project is described.

B. EXPERIMENTAL PROCEDURES

Vapor deposited films of BZP, BZP-d_{10} and mixtures of NAP/BZP were studied in this project. The experimental procedures by which the crystallization of these film was examined are outlined below.

1. *Samples*

The organic molecules which were the subject of this study were deposited on the surface of a wafer of highly oriented pyrolytic graphite (HOPG). The graphite was obtained from Union Carbide of Parma, Ohio.

BZP was obtained from Aldrich (Gold Label 99+%) and was purified by zone refining more than 200 passes before use. BZP-d_{10} was obtained from MSD Isotopes (98.8 atom % D) and used without further purification. NAP was obtained from Aldrich (scintillation grade, 99+%) and used without further purification.

The cryogenic solutions used to control the vapor pressure of the NAP sample source were thiophene, o-xylene and water. The thiophene was obtained from Aldrich (99%+, Gold Label) and mixed with liquid nitrogen to form a slurry having a temperature of -38 C. The o-xylene was obtained from Aldrich (97%) and mixed with liquid nitrogen to form a slurry

having a temperature of -29 C. Water was mixed with ice to form a 0 C slurry.

2. *Deposition Procedure*

The deposition rates of the aromatic compounds of this project were determined using an interferometric technique. The experimental setup used to record deposition rates is illustrated in figure 1. The deposition procedure was carried out as follows. The aromatic compound of interest was loaded into a sample delivery chamber connected to the vacuum shroud of a helium refrigerator. Once the vacuum chamber was evacuated the sample chamber was evacuated. The sample was then cooled to 18 K. In addition, the sample delivery chamber was brought to a constant temperature with either a refrigerated circulating bath or a cryogenic solution. The refrigerator vacuum shroud was positioned with the sample delivery port normal to the sample surface in the case of the shroud with one sample delivery port or 45 degrees with respect to the sample surface in the case of the shroud with two sample delivery ports.

Neat films of BZP and BZP-d_{10} were deposited from a sample source held at 20 C using the refrigerated circulating bath. Mixed films of NAP/BZP were deposited with the BZP sample source held at 20 C and the NAP sample source held at either 0, -29 or -38 C depending on the desired mole fraction.

Figure 1. Deposition Experimental Setup. S= sample support, A= aperture, MC= monochromator, PRV= high voltage power supply for Peltier refrigerators, PMTV= high voltage power supply for photomultiplier tube, AD= amplifier/discriminator, PMT= photomultiplier tube mounted in refrigerated housing, C= computer, RC= remote control panel for MC, AL= argon ion laser.

S

MC

A

PRV

PMTV

PMT

AD

AL

RC

count = 5000

C
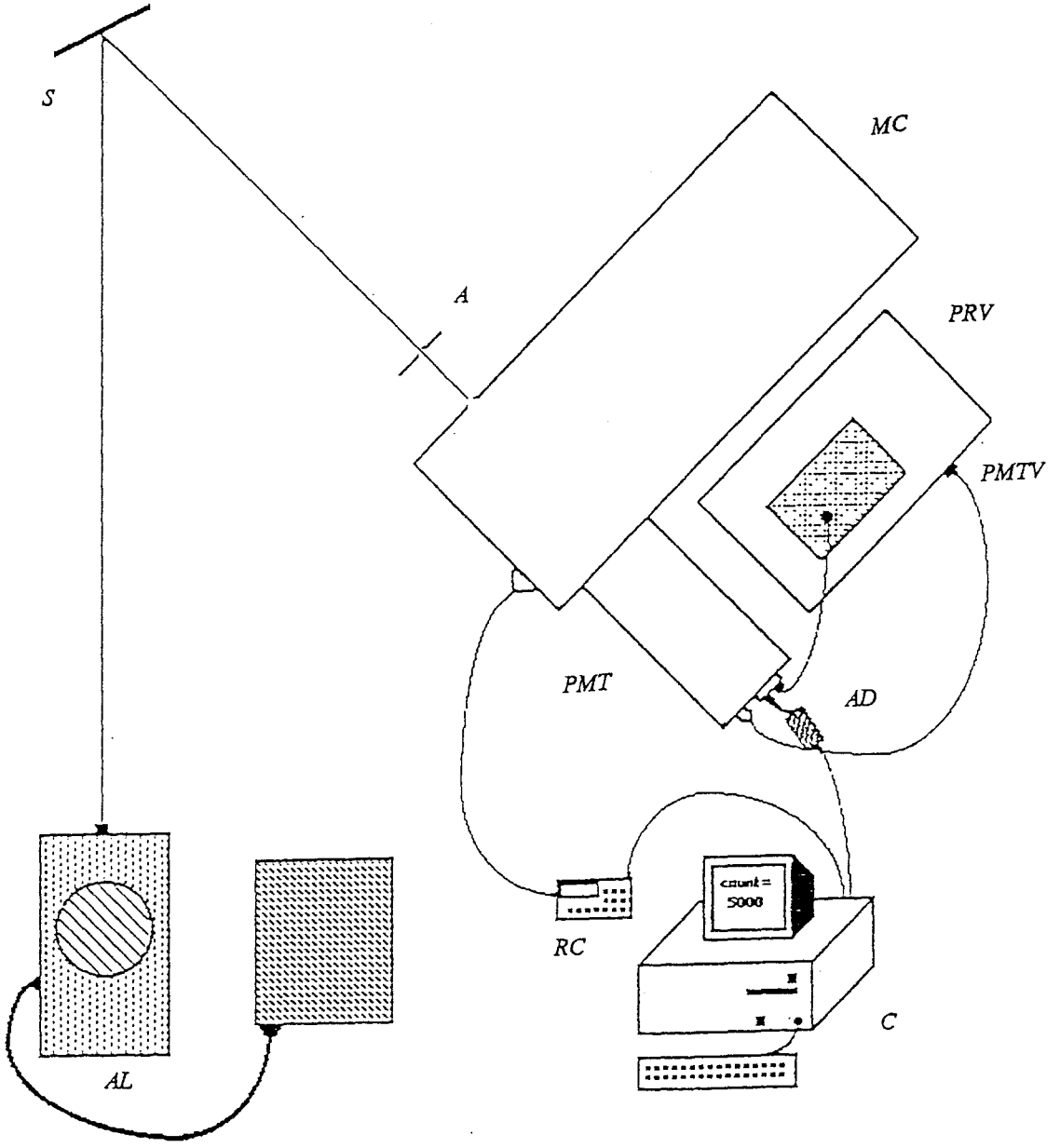
The 18 K sample support surface was cleaned using pulsed laser induced thermal desorption. The energy was supplied by 9 nanosecond laser pulses from the 1066 nm fundamental of a Nd:YAG laser (Quantel YG660A).

An argon ion laser was reflected from the surface to the monochromator slits for dispersion and subsequent detection. A computer controlled data acquisition system was used to record the number of photons incident on the monochromator slits with respect to time during sample deposition. Just prior to activating the computer the sample delivery stopcock was fully opened initiating deposition.

3. *Emission Spectra, Radiative Decay and Light Scattering Procedures*

The emission spectra, radiative decay, and light scattering experiments were initiated in the same manner as the deposition experiment. After a 1000 Å thick neat or mixed film had been deposited, the sample delivery stopcock was closed and the shroud rotated so as to provide optical access.

Emission spectra, decay measurements and scattered light intensity were all recorded for the as-deposited sample using the light sources and optical setups described in section II.B. Figures 2 and 3 depict the experimental setups used to record emission spectra, light scattering intensity and radiative decay curves, respectively. Subsequent to optical

Figure 2. Emission Spectra and light scattering experimental setup. S= sample support, L= lens, MC= monochromator, PRV= high voltage power supply for Peltier refrigerators, PMTV= high voltage power supply for photomultiplier tube, AD= amplifier/discriminator, PMT= photomultiplier tube mounted in refrigerated housing, C= computer, RC= remote control panel for MC, HNL= helium-neon laser, XAL= xenon arc lamp, A= aperture.

S

L

L

A

L

XAL

HNL

MC

PRV

PMTV

PMT

AD

RC

C
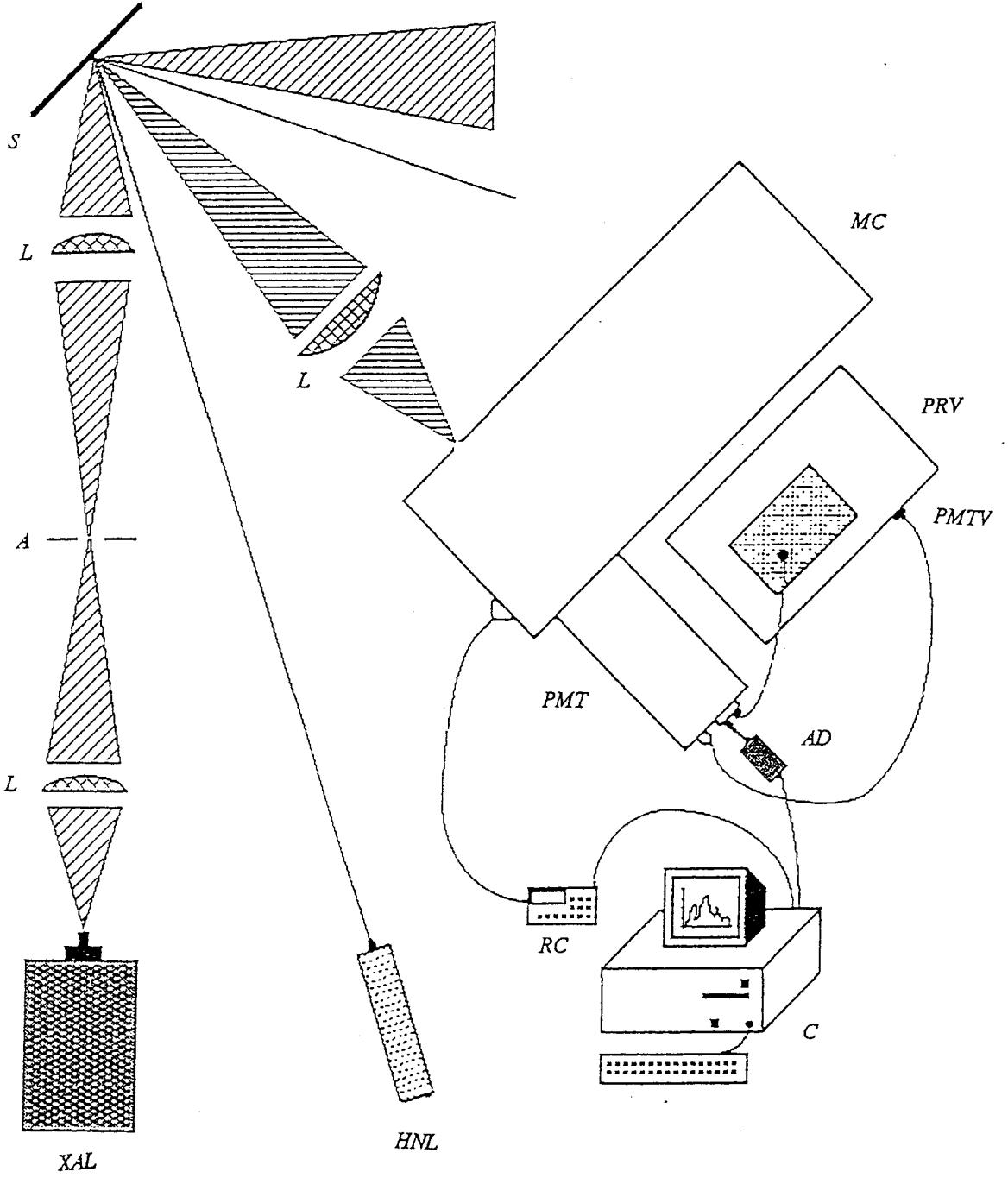
Figure 3. Radiative Decay Experimental Setup. S= sample support, L= lens, MC= monochromator, PRV= high voltage power supply for Peltier refrigerators, PMTV= high voltage power supply for photomultiplier tube, AD= amplifier/discriminator, PMT= photomultiplier tube mounted in refrigerated housing, OS= oscilloscope, RC= remote control panel for MC, PG= pulse generator, NL= nitrogen laser, FG= function generator, A= aperture.

S

A

L

MC

PRV

PMTV

PMT

AD

FG

NL

RC

PG

OS
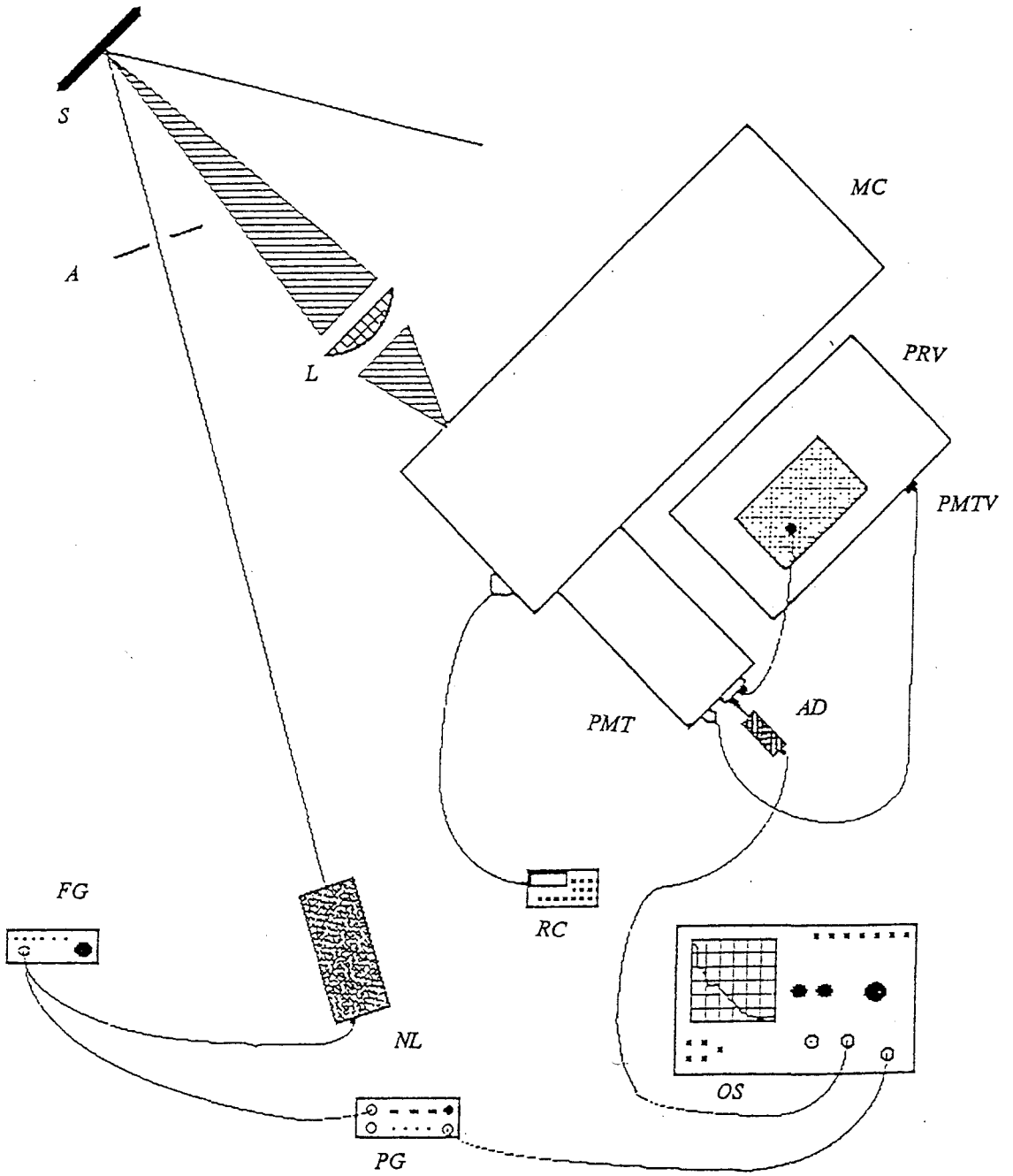
interrogation of the as-deposited sample, the sample support temperature was increased by some temperature T_{ex} using a temperature controller and then allowed to return to 18 K. This constituted an annealing cycle, after which spectroscopic measurements were repeated. Annealing cycles were carried out sequentially, increasing T_{ex} with each cycle. In the course of annealing experiments, optical measurements took place at 18 K immediately after each cycle. Experiments were usually stopped after T_{ex} had reached 180 K.

C. EXPERIMENTAL COMPONENTS

1. Optical Components

a. Deposition rates

Deposition rates of the various samples were determined using an interferometric technique. An argon ion laser (Omnichrome 1532, 488 nm line (20,492 cm^{-1})) was directed at such an angle with respect to the sample support so the reflected beam would enter the monochromator slits (CVI Laser, Digikrōm 480) set to 25 μm (1 cm^{-1}). As the sample material deposited on the sample support, the reflected beam intensity was modulated by constructive and destructive interference. The interference resulted as the laser beam interacted with the sample film and support surfaces. No collection optics

were used in this configuration. An end-on photomultiplier tube (either a Hamamatsu R649 or an EMI 9658R) based detection system detected the photons incident on the monochromator slits with time. The resulting cosine curve was used to calculate the sample deposition rate.

b. *Emission Spectra*

Sample emission was excited by either a 1000 watt, high pressure xenon short-arc lamp (Schoeffel LPS-255HR power supply and LH-151N/3 lamp housing) or pulsed nitrogen laser (LSI VSL-337ND).

The nitrogen laser beam was directed to the sample support surface at such an angle so as to minimize the proportion of scattered light incident on the monochromator slits. The unfocused 337 nm (29,674 cm^{-1}) laser beam was then passed through a 300-400 nm (33,333-25,000 cm^{-1}) band pass filter (Oriel). The filter prevented visible plasma lines of the laser from scattering off the surface and interfering with emission spectra measurements.

The xenon arc lamp beam required considerable manipulation and filtering prior to sample excitation. The lamp housing has a 9.5 cm O.D. light pipe perpendicular to the lamp axis. Two fused silica, plano-convex lenses with their flat surfaces parallel served to collect and collimate the lamp light. The first lens (14 cm focal length) had its

curved surface facing the lamp while the second lens (11 cm focal length) had its curved surface facing the sample. The parallel surfaces of the lenses were 1 cm apart. The image point of this lens system was adjustable via the light pipe containing the lenses.

The collimated lamp light was then passed through a custom built filter (figure 4). The filter had been configured of a 6.5 cm long pyrex tube with 3.5 cm diameter fused silica windows epoxied to each end. A water-based, nickel sulfate and cobalt chloride filtering solution was pumped through the filter via two 1.3 cm O.D. pyrex tubes perpendicular to the filter optical axis. A 500 ml Erlenmeyer flask was used as a reservoir for the filter solution. The solution was held at 0 celsius using an ice bath. The filter body was held in place by a custom built holder attached to the lamp light pipe (figure 4). A 400 nm (25,000 cm^{-1}) short pass filter (Oriel) was placed at the exit side of the filter.

The transmittance spectra of the filter solutions are illustrated in figure 5 and the emission spectrum of the filtered lamp light is in figure 6. As is evident in figure 6, the filters eliminated all traces of interfering light. The aqueous solution also eliminated the infrared emission of the lamp.

The filtered lamp light was further collimated by two fused silica plano convex lenses (Melles Griot) with their flat sides facing the lamp. The first lens was 15 cm from

Figure 4. Lamp filter and filter holder. LF= lamp filter, LFH= lamp filter holder.

LFH

9.5 cm

3.6 cm

10.5 cm

6.5 cm

3.5 cm

2.0 cm

O.D.

3.5 cm

6.5 cm

LF

1.3 cm

O.D.

4.5 cm

1.0 cm
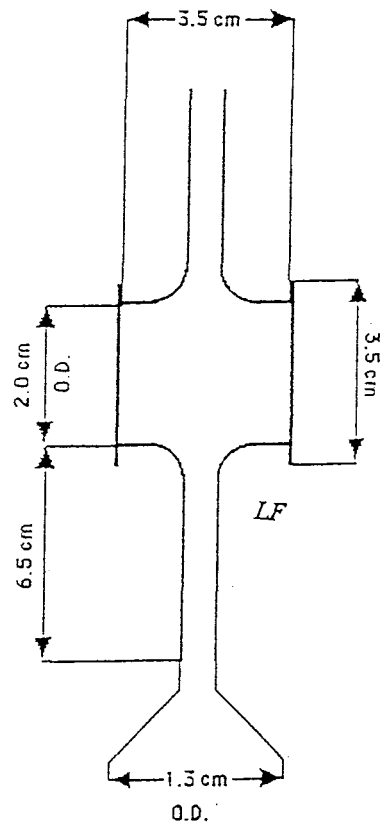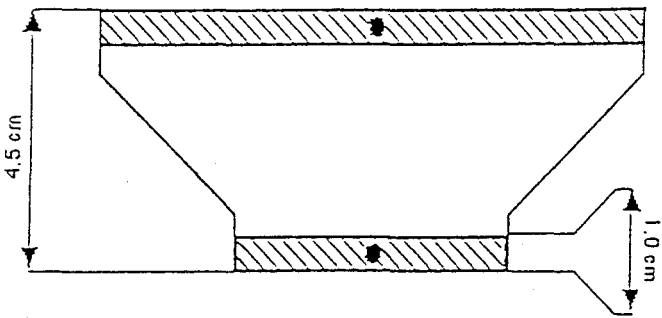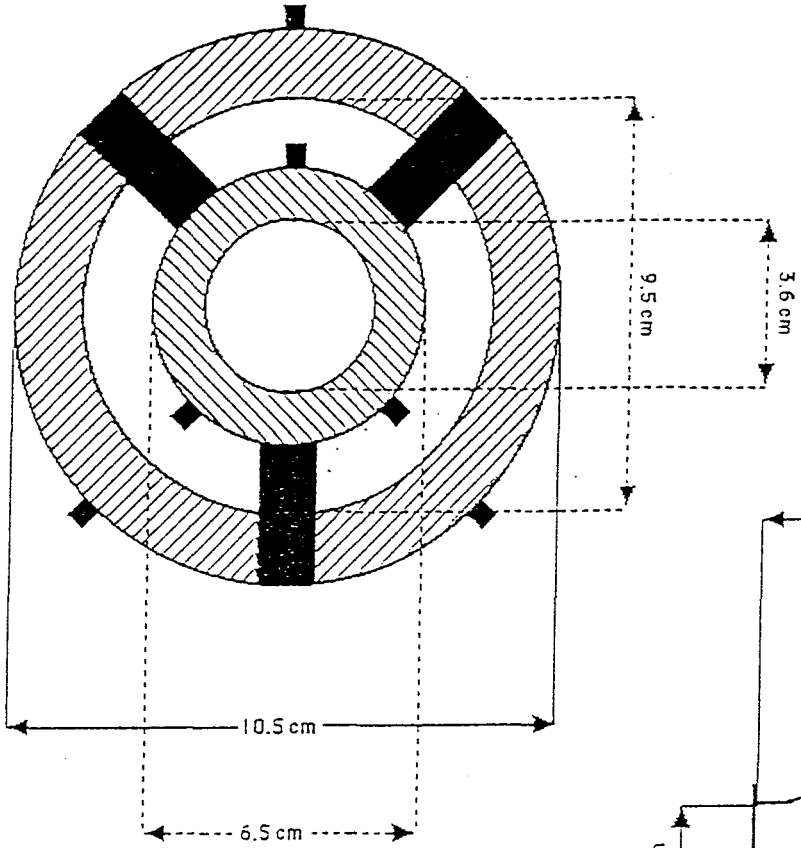
Figure 5. Transmittance spectra of lamp filter components.
The components are nickel sulfate (top) and cobalt chloride
(bottom).

%T

WAVELENGTH(nm)

230   800
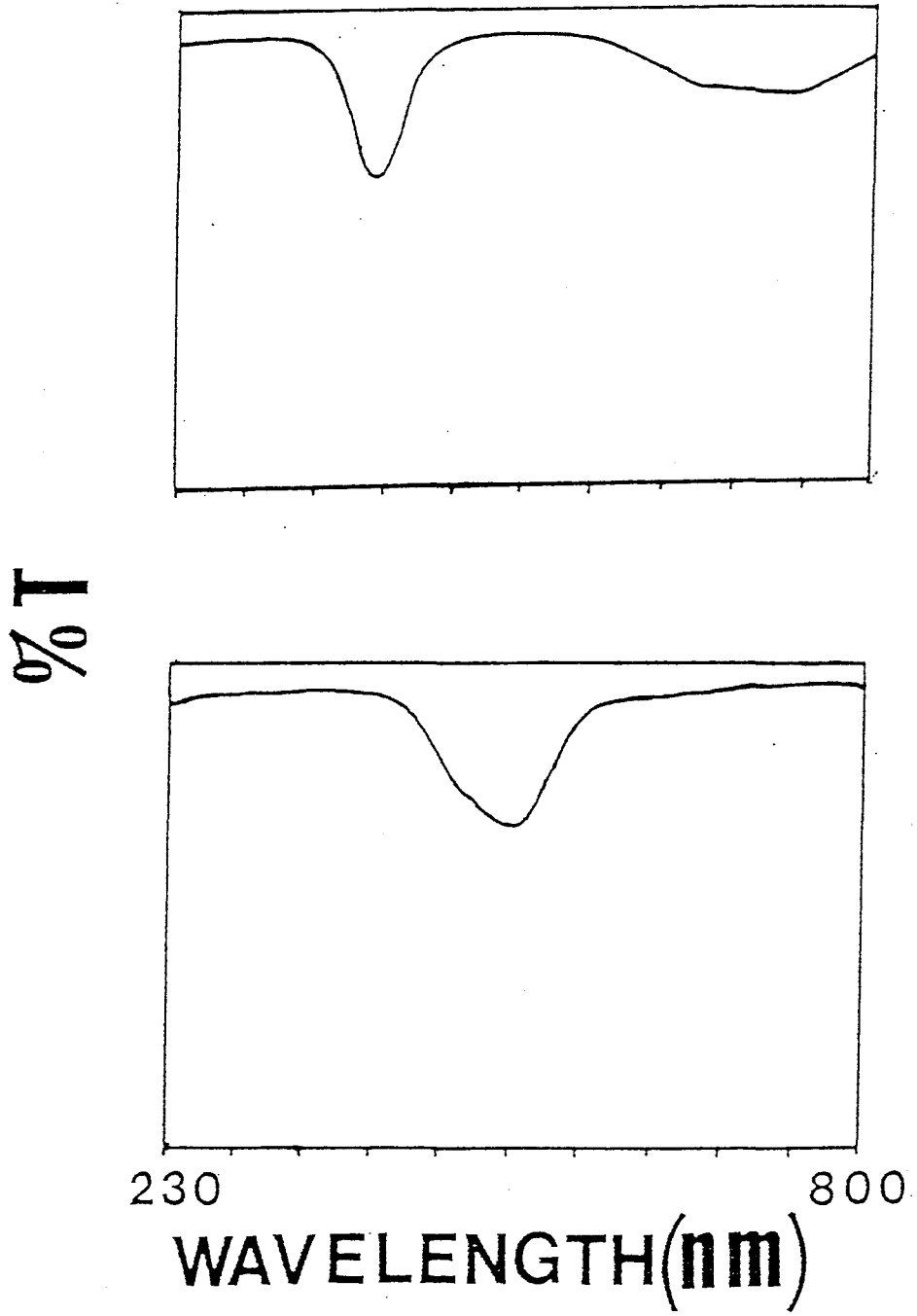
Figure 6. Emission spectrum of filtered lamp emission.
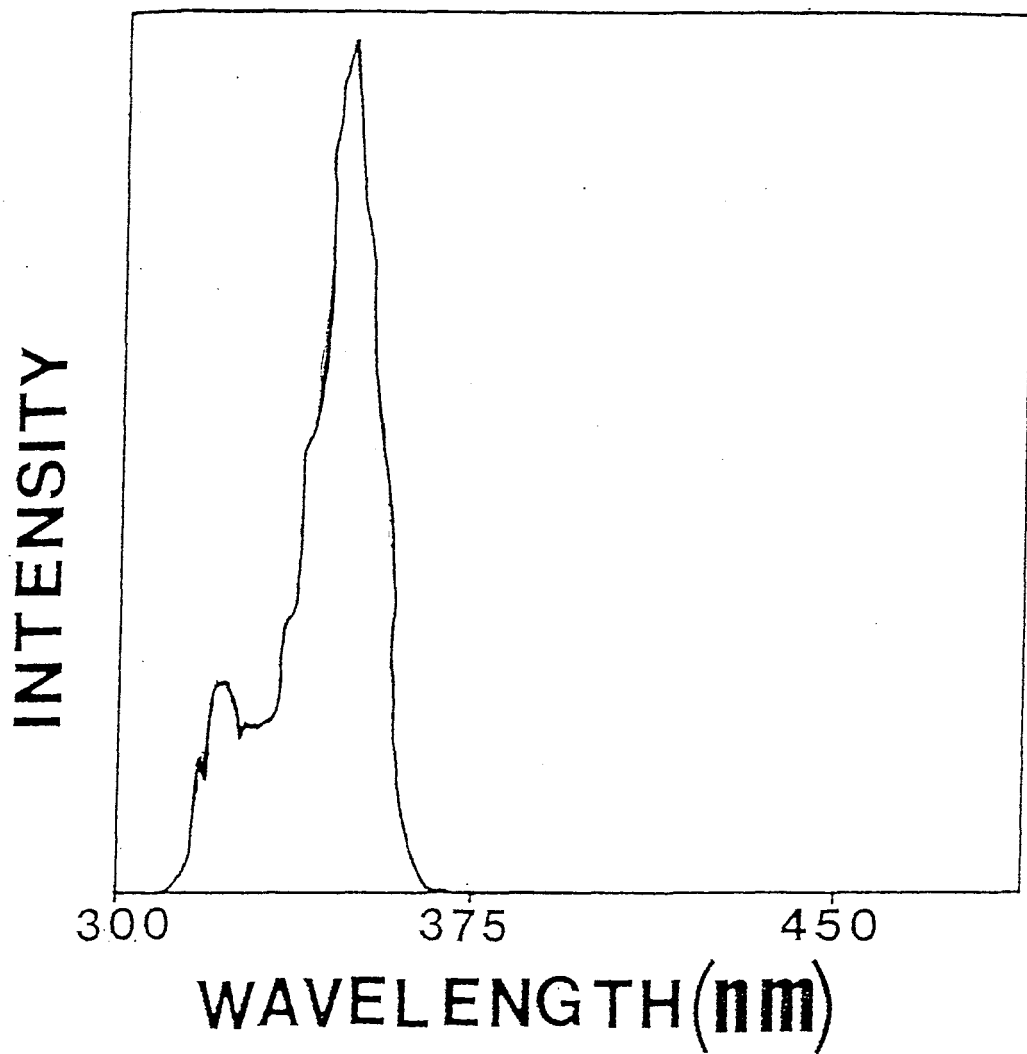
the lamp filter and had a 4.5 cm focal length. The second
lens had a 7.5 cm focal length and was located 27 cm from the
first lens and 9.5 cm from the sample support surface. An
aperture was positioned between these two lenses in order to
minimize light scattering and limit the beam size. The lamp
beam was directed to the surface at an angle so as to minimize
light scattering to the monochromator slits. Due to the
inefficiency of collimating a point source, the scattered
light from the sample support surface was not insignificant.
However, this did not present a problem for recording spectra
in the wavelength range 360 - 640 nm (27,778-15,625 cm^{-1}).

Sample emission was collimated and focused on the
monochromator slits. Spectra were recorded using a computer
controlled data acquisition system. All cw spectra were
recorded with a 1 sec. integration time and ± 5 Å (±28 cm^{-1})
resolution. Time resolved spectra were recorded using the
nitrogen laser and an integration time of 50 ms.

c. Radiative Decay Measurements

The 3 nanosecond pulse width of the nitrogen laser was
used to excite samples for radiative decay measurements. The
nitrogen laser average power was usually 3.5 milliwatts
(depending on the repetition rate) and its peak power was 70
kilowatts. The unfocused beam was passed through a 300-400
nm (33,333-25,000 cm^{-1}) band pass filter (Oriel) to minimize

interference due to visible cavity modes. Just after the band pass filter, the beam traversed an aperture used to limit the beam size to that of the excitation sources discussed above, e.g. the lamp. As with the other light sources, the incidence angle was chosen so as to minimize light scattering to the monochromator slits. The nitrogen laser was anchored in a custom built aluminum rack.

Radiative decay measurements were recorded using the nitrogen laser pulsing with a 10 Hz. repetition rate and a 100 ns delay with respect to signal acquisition. The sample emission was detected at 23,697 $\pm$90 cm^{-1}. The photomultiplier tube signal was recorded using a digital storage oscilloscope (Tektronix 3010, 100 MHz. bandwidth) operating in the signal average mode with a scan window of 50 ms.

d. *Light Scattering*

The 633 nm (15,798 cm^{-1}) unfocused beam of the helium-neon laser was passed through an aperture to limit the beam size on the sample surface. The angle of incidence was chosen so as to place the direct reflected beam far from the monochromator slits. The light scattered normal to the surface was detected by the monochromator/phototube at 15,798 $\pm$1 cm^{-1}. The helium-neon laser had also been anchored to the rack along with the nitrogen laser.

The emission, decay rate and light scattering experiments

were all carried out simultaneously using the same collimating lens. The plano-convex lens was made of optical quality glass with a 4 cm focal length (Edmund Scientific). It was positioned with its curved surface facing toward the monochromator slits. The lens was positioned 15 cm from the support surface and 12.5 cm from the monochromator slits. These distances ensured the light of the sample was imaged on the monochromator slits. This was found to be the most efficient light collimating system.

2. *Optical Detection Configurations*

a. *Light Detection*

Sample emission was collected and focused onto the entrance slits of the monochromator with the photomultiplier tube positioned at the exit slits. The PMT was mounted in a thermoelectrically cooled PMT housing (Pacific Instruments 3463,C). This housing contains two Peltier refrigerators capable of cooling the PMT to -30 C. The Peltier refrigerators were powered by a high voltage power supply/temperature controller (Pacific Instruments model 33). The PMT was powered by a high voltage power supply (Pacific Instruments) with operating range between 0 and 2000 volts. The PMT current output was amplified and/or discriminated by a preamplifier (Modern Instrumentation Technology, Combo-100).

The Combo-100 has two outputs: one as an amplified voltage proportional to the PMT current output and the other as TTL transitions associated with the current pulses of the PMT.

b. Data Acquisition and Control

i. Control and Acquisition of Emission Spectra and Scattered Light Intensity

The components for acquisition and control of emission spectra and scattered light intensity were connected to one another with coaxial cable.

The Combo-100 TTL output was connected to the counter/timer clock input 0 (Metrabyte DAS-8). The DAS-8 module is a multifunction computer interface board. The counter/timer gate 0 was connected to an inverter (RCA 7404) output. The inverter input was connected to the IP1 status register (Metrabyte DAS-8) and the gate input of a manually programed time delay module (Evans 4145/4146). The 4145/4146 board was manually operated in binary coded decimal (BCD) format with a time delay window of between 0 and 9.9999999 seconds in 10 nanosecond intervals. The 4145/4146 trigger input was connected to the counter/timer output 2 (Metrabyte DAS-8). Finally the Zenith microcomputer (Z-159) communications output (RS-232C) was connected to the monochromator external control input.

Data acquisition was initiated when a computer program (KROM2.BAS) triggered counter/timer 2 (operating in the software triggered strobe mode) to output a negative going pulse on terminal count. This strobe triggered the 4145/4146 causing the gate to open (negative transition) for the time interval set by the BCD thumb wheels. The 4145/4146 gate status was software monitored by the IP1 status register. This signaled the computer when the counting process had ended so it can proceed. The 4145/4146 gate pulse was inverted and controlled the gate of the counter/timer 0. The counter/timer 0 clock input was used to input the TTL pulses of the Combo-100 preamplifier. Counter/timer 0 was operated in the pulse counting mode and only counted pulses while the gate was open (positive transition). While the 4145/4146 gate was open the counter/timer 0 memory buffer stored the number of pulses counted. Counting ceased after the 4145/4146 gate closed thereby closing the counter/timer 0 gate. The counter/timer 0 memory buffer was software read after the 4145/4146 timeout had been sensed by the computer at the IP1 status register. Finally the monochromator grating was software incremented and the cycle was repeated. The monochromator was not incremented for the light scattering experiment. The counts were recorded over time intervals as apposed to wavelength intervals.

ii. Control and Acquisition of Delayed Emission Spectra

The essential features of this system were the same as those outlined in the section on control and acquisition of emission spectra and scattered light intensity. All additional connections which were required are outlined below. The digital output OP1 (Metrabyte DAS-8) was connected to the computer controlled 4145/4146 trigger input and the nitrogen laser trigger input for external control. The computer controlled 4145/4146 was controlled by a parallel digital I/O interface (Metrabyte PIO-12). The PIO-12 is a digital I/O computer interface board used to set the time on the 4145/4146 programmable time delay module using computer software. Thus time delays between the nitrogen laser firing and data acquisition were software controlled, i.e. using program N2KROM.BAS. The computer controlled 4145/4146 delayed output was connected to the manually controlled 4145/4146 trigger input. The computer controlled 4145/4146 gate was connected the IP2 control register. All other connections were the same as in the previous section except the software triggered strobe counter/timer 2 was not used.

The acquisition of delayed spectra was initiated when the software controlled OP1 digital output (5 volts, positive transition) triggered the nitrogen laser to fire and the software set 4145/4146 timer to generate a delay. The computer controlled 4145/4146 gate (delay time) status was

checked by the IP2 status register. The IP2 register was software read before the IP1 register since the manually controlled 4145/4146 was triggered by the computer controlled 4145/4146 delayed output upon timeout. After the computer controlled 4145/4146 timeout, the data acquisition followed the same course as described above.

iii. Control and Acquisition of Radiative Decay Measurements

Radiative decay measurements were recorded using the pulsed nitrogen laser, the optical detection system described in section II.5.a on light detection, a function generator (B+K Precision Dynascan, 3010), a pulse generator (B+K Precision Dynascan, 3300) and the digital storage oscilloscope. All connections were made with coaxial cable.

The function generator was connected to the nitrogen laser and the pulse generator input. The output of the pulse generator was connected to the external trigger input of the oscilloscope. The combo-100 amplified voltage output was connected to a three way connector which was connected to the oscilloscope channel B input. The other end of the three way connector had a 50 ohm resistor connected between the signal and ground. This was done to impedance-match the Combo-100 output with the oscilloscope. The oscilloscope X-Y plotter output was connected to the computer controlled analog-to-digital (A-D) converter channels 0,1 and 3 (Metrabyte DAS-8).

Channels 1 and 3 were connected to the X and Y outputs, respectively. Channel 0 was connected to the variable 4.5-4.6 volt output.

Acquisition of decay curves was initiated with the function generator operating in the square wave mode. The function generator pulsing at 10 Hertz triggered the nitrogen laser and initiated the pulse generator so as to deliver a delayed pulse to the oscilloscope external trigger input. The oscilloscope was operated in the signal averaging mode. The pulse triggered the oscilloscope to sweep at sometime t_0 after the nitrogen laser fired. This was done to ensure that there was no interference in the radiative decay measurement from the laser pulse. Usually 300 scans were averaged with the number of scans dependent on the signal-to-noise level. Each sweep was usually weighted by a factor of 1/256. The selected weighting factor depended on the signal-to-noise level. After the decay signal had been acquired and stored, the oscilloscope was operated in the plotting mode. Channels 1 and 3 of the A-D were software read using program OSCOPEK.BAS. The software recording process was triggered by the variable output voltage of the oscilloscope read at channel 0 of the A-D converter. The voltage goes low just prior to the X-Y output of oscilloscope. The data transfer process was software terminated upon the positive transition of the voltage signal read at A-D converter channel 0.

3. *Cryogenic Components*

In the course of this thesis work, low temperature conditions were maintained using the final cooling stage of a closed cycle helium refrigerator (Air Products Displex CS202) (Figure 7). The HOPG sample support was mounted to a copper holder which was screwed into the bottom of the final expansion stage of the refrigerator. Sample holder threads were greased (Dow-Corning silicon grease) to enhance thermal contact. While the refrigerator's base temperature is 10 K, no heat shield or reflective shroud was used in the experiments. This limited the actual working temperature range to 18 to 300 K.

Refrigerator temperatures were maintained and monitored using a temperature controller (Lake Shore Cryotronics 805). The temperature controller monitors the temperature by sensing thermally induced voltage changes in a silicon diode (Lake Shore Cryotronics DT-471-10L) as a 10 microampere constant current is passed through it. Voltage-versus-temperature changes are referenced with one of several calibration curves in the temperature controller's memory. "Curve 2" was selected for the DT-471-10L diode used in this project by setting appropriate dip switches at the rear of the instrument. The temperature resolution of the temperature controller is ± 0.005 K below 100.0 K and ± 0.05 K above 99.99 K.

Figure 7. Cryogenic Components. TC= temperature controller, RES= helium refrigerator expansion stages, TD= temperature sensing diode, SH= sample holder, EF= electrical feed through, CM= helium refrigerator compressor, TCG= thermocouple pressure sensor.

The temperature sensing diode was attached to the final cooling stage of the refrigerator using high vacuum silicon grease (Dow-Corning) and wire wrapping. The wire leads to the diode were wrapped around the expansion stages of the refrigerator and passed through a custom made, high vacuum electrical feed-through. The electrical feed-through had been machined from an aluminum tube with two .44 cm holes perpendicular to its axis (cf. figure 7). These holes pass the electrical connections from the temperature sensing diode to the temperature controller. The feed-through was connected to the refrigerator at an existing o-ring sealed port. At the opposite end of the electrical feed-through is a .32 cm pipe-threaded opening for a thermistor pressure gauge.

In the course of this work, temperatures above 18 K were attained using a 46 ohm resistive wire element wrapped around the refrigerator's final cooling stage. Two copper wire leads are wrapped around the expansion stages to a second electrical feed-through. These wires are connected directly to the temperature controller. The temperature controller supplies a preset current to the resistive element which induces ohmic heating at the cryotip. Temperatures above 18 K were maintained by the temperature controller monitoring the time rate of change of the temperature over a predetermined integration period. More or less current is supplied to the resistive element depending on the slope of the temperature change. When the slope is zero a constant current is

maintained. The heater power or maximum current supplied to the cryotip can be selected as a high, medium or low heating rate corresponding to 13.8 (300 milliamps), 4.6 (100 milliamps) or .046 (1 milliamps) watts, respectively.

4. *Vacuum Shrouds*

The vacuum shrouds used to isolate the cooling stages of the helium refrigerator were constructed of pyrex, so as to offer both optical access and bakeability. Two different shroud configurations were utilized for this project. Both had been custom made from a 71/60 ground-glass, straight-seal, sleeve joint and 7 cm I.D. pyrex tubing. The upper lip of the straight seal was sealed against a rubber o-ring sealing the vacuum chamber of the refrigerator. (cf. figure 8 for dimensions).

Two different shroud configurations were used in this project. One has two ports located at an angle of approximately 45 degrees with respect to one another. The first port is a 9 mm I.D. straight o-ring sealed joint (Ace Glass 7646). A 4 cm diameter fused silica window was placed over the o-ring to create an optical access port for excitation sources less than 320 nm. This window was necessary for samples requiring an excitation source of shorter wavelength than the pyrex transmittance cutoff of 320 nm. The second port is a ground glass 18/9 spherical socket

Figure 8. Vacuum shroud and attachments. SH= shroud main body, HVV= high vacuum valve SCP= sample container connector port.
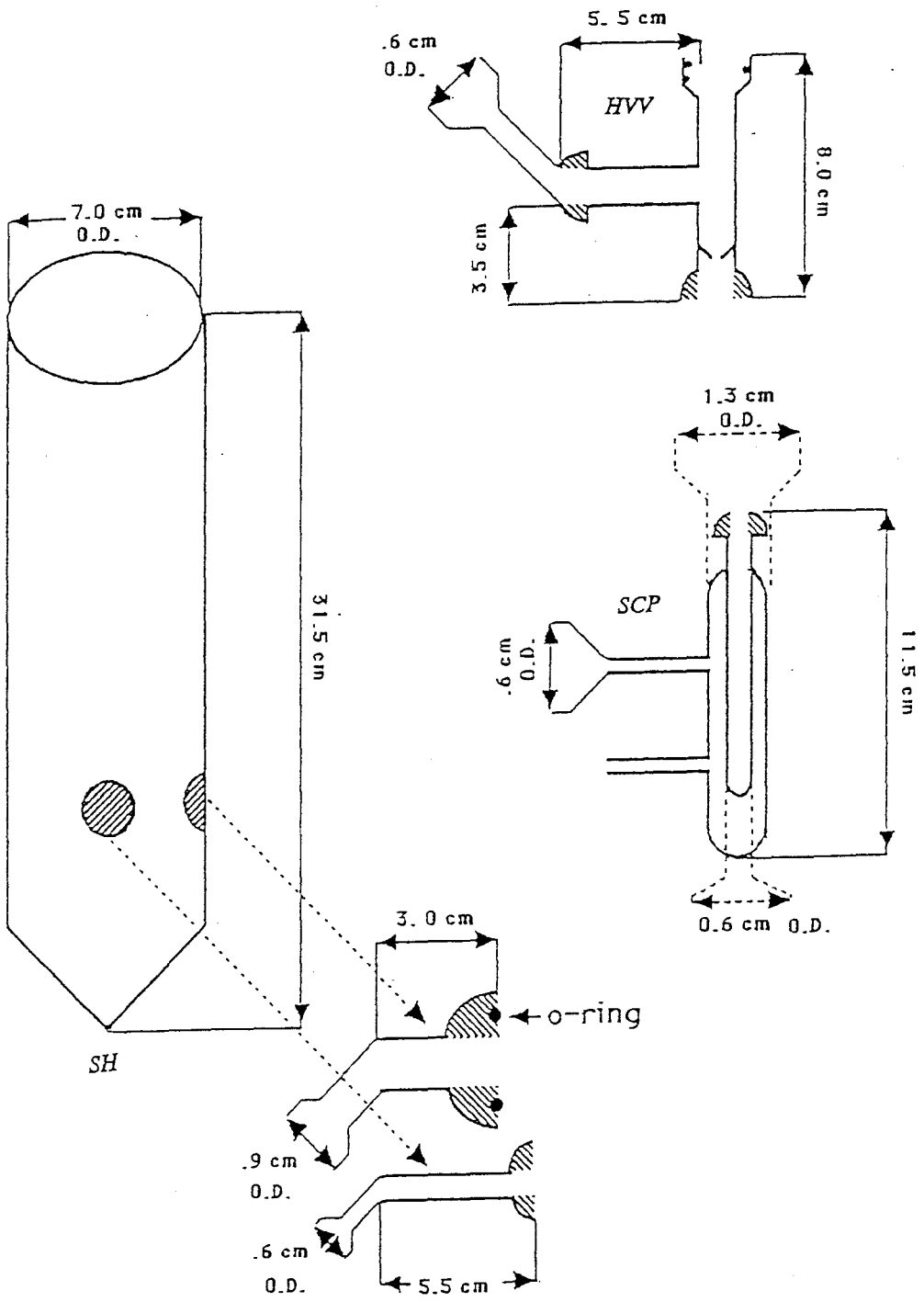
joint (Ace Glass 7655). This port was used for connection of various sample delivery vessels.

The other shroud had been configured with two access ports at an angle of approximately 45 degrees with respect to each other. Both are 18/9 ground glass spherical socket joints. The ports were used to connect sample delivery chambers to the shroud for simultaneous introduction of sample components.

Sample delivery vessels were configured from a high vacuum stopcock (Ace Glass 8194) and sample tube connected in tandem to the ground glass spherical socket joints of the shroud. All these connections were made with 18/9 ground glass ball and socket joints. The custom made sample chambers were either a water-jacketed (6 mm O.D.) or an unjacketed (13 mm O.D.) glass tube.

The water jacketed sample chamber had been used to maintain sample temperatures between 100 and -15 C. A refrigerated circulating bath (Neslab Endocal 012202-23) was used to regulate sample temperatures in this range. The unjacketed sample chamber was submersed in various cryogenic fluids to maintain sample temperatures below -15 C.

5. *Vacuum System*

The vacuum system constructed for this project is shown in figure 9. The mechanical roughing pump (Sargent-Welch

Figure 9. Vacuum system components. BFV= butterfly valve. HHV= hand operated high vacuum valve, T= liquid nitrogen cold trap, RP= roughing pump, DP= diffusion pump, ST= stainless steel cold trap.

BFV

ST

DP

HHV

To refrigerator

RP

T

5.5 cm

1.9 cm
O.D.

10.5 cm

9.0 cm

7.0 cm
O.D.
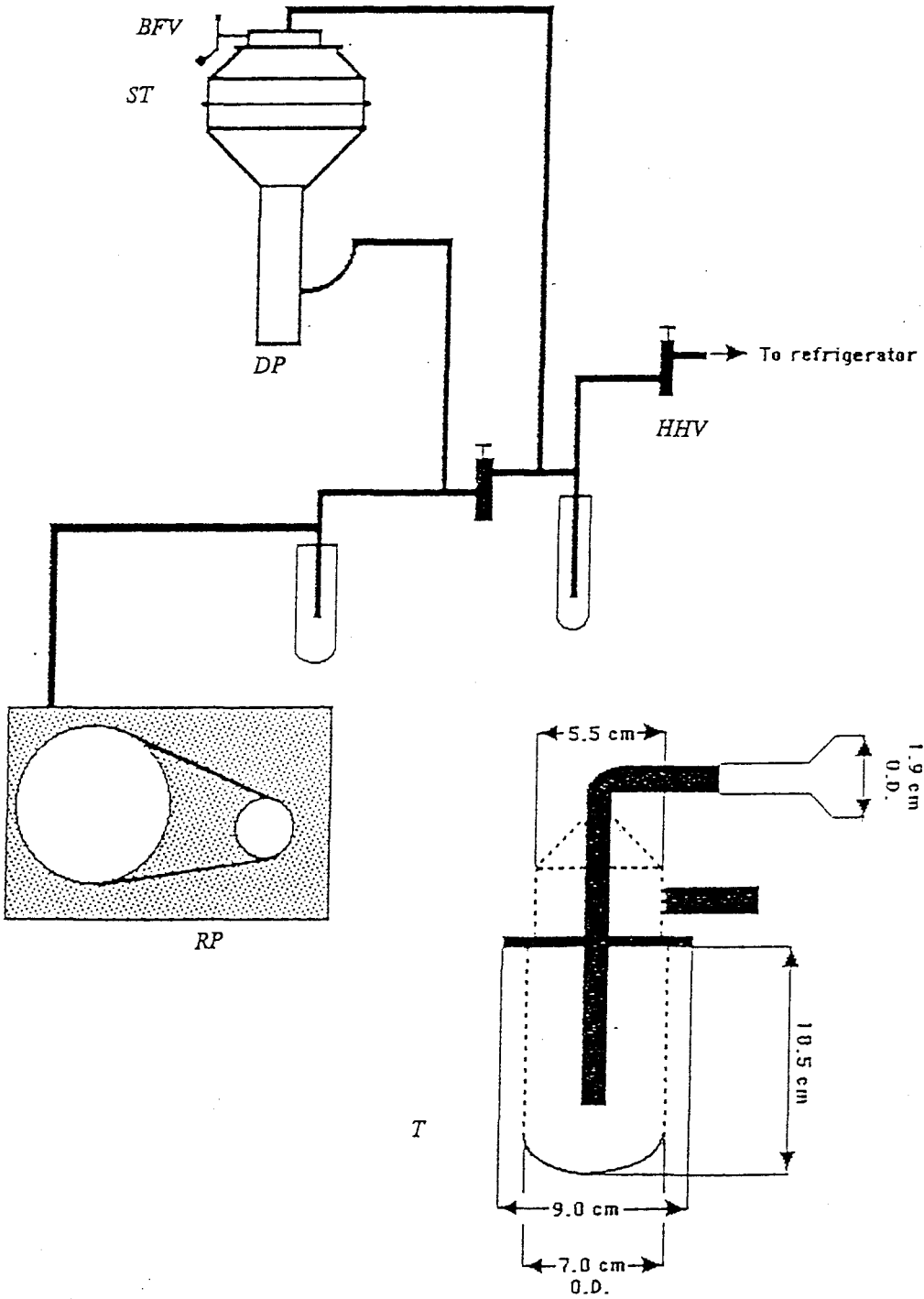
Duo-seal, model 1402) is connected via high vacuum rubber tubing and 3/4 inch copper pipe to the low pressure side of a liquid nitrogen trap. Two liquid nitrogen traps were utilized in this vacuum system. Both are made of copper pipe, machined brass and pyrex (cf. figure 9 for dimensions). The low pressure side of the first trap is connected to the high pressure side of a second liquid nitrogen trap and the low pressure side of a 2 inch air-cooled, oil diffusion pump (Varian HAS). The diffusion pump has a cryotrap (Varian 325) and butterfly flange mounted to its low pressure side. The low pressure side of the diffusion pump is connected to the high pressure side of the second liquid nitrogen trap. The diffusion pump can be isolated using the butterfly flange mounted to its low pressure side. When the pump was in use, the butterfly flange was opened and the hand-operated brass high vacuum valve (Varian) between the liquid nitrogen traps was shut. This directed the gas flow through the two traps and the diffusion pump. The low pressure side of the second liquid nitrogen trap was connected to the helium refrigerators vacuum chamber through a second hand-operated stainless steel, high vacuum valve (Varian). This second valve was used to isolate the helium refrigerator after cooling below 77 K. All interconnecting tubing is 3/4 inch copper pipe with solder connections. The refrigerator and all its components (except the mechanical pump) were mounted in a custom made steel rack.

The vacuum pressure was monitored either by a

thermocouple gauge (Varian TC801 gauge controller and 531 gauge tube) or a residual gas analyzer (Edwards High Vacuum EQ100F). Both were connected directly to the vacuum chamber of the refrigerator. The thermocouple gauge tube was threaded into the .32 cm pipe threaded end of the custom made high vacuum feed-through. Its operating range was between 10^{-3} and 2 torr.

The residual gas analyzer unit was used to monitor pressure changes during experiments, detect vacuum leaks, and check the vacuum for contaminants. Its mass selection range is between 1 and 100 amu and its pressure measurement range is between 10^{-3} and 10^{-12} torr. The base pressure of the vacuum system without the helium refrigerator operating was 10^{-6} torr and with the refrigerator operating 10^{-8} torr.

D. SIMULATION OF RADIATIVE DECAY CURVES

The radiative decay curves recorded during cyclic-annealing experiments were fitted to two equations subsequent to conditioning. The decay curves were acquired as a sequential file with x,y pairs. The data points were the output voltages of the oscilloscope. The x values were converted to the actual time for the experiment and the y values were normalized to between 0 and 10,000. These large y values minimize round-off and repeating decimal errors associated with numbers less than one.

The decay curves of this project were simulated using the simplex nonlinear regression analysis technique. The details of how the simplex algorithm works can be found in the book by Demas (see reference 22). The program in the back of this book is the one used in this project.

CHAPTER III.

LOW TEMPERATURE OPTICAL EMISSION PROPERTIES OF DISORDERED BENZOPHENONE, BENZOPHENONE-d_{10} and NAPHTHALENE/BENZOPHENONE MIXTURES

The cw emission and radiative decay characteristics of vapor-quenched BZP and BZP-d_{10} and the cw emission characteristics of vapor-quenched NAP/BZP mixtures were studied at low temperature as a function of cyclic-annealing. Those spectral properties which relate to the microscopic interactions of the condensed phase were carefully examined. This was done in order to get at how the microscopic interactions change along the crystallization pathway of vapor-quenched BZP and BZP-d_{10}. These changes provide information about the actual crystallization pathway.

A. *LOW TEMPERATURE EMISSION SPECTRA OF DISORDERED BENZOPHENONE AND BENZOPHENONE-d_{10}.*

1. *Light Scattering / Annealing Behavior*

The as-deposited BZP films prepared in this project were of thickness less than the wavelength of visible light and

were visually transparent. No visible changes in the film were observed with cyclic-annealing in the range 18 to 160 K. However, in the annealing range 160 to 180 K BZP films became increasingly opaque. The annealing dependent behavior of the optical density of the BZP films is illustrated in figure 10. In figure 10 the scattered helium-neon laser light intensity (I_s) recorded at 18 K is plotted versus annealing temperature in the range 18 to 180 K. Appreciable light scattering by the sample only occurs if the sample possesses density fluctuations of the same length scale of the incident light. The figure therefore demonstrates that density fluctuations on the length scale of visible light only occur in the sample as it is annealed in the range 160 to 180 K. The results for the BZP-d_{10} sample were similar.

2. *CW spectra / Annealing Behavior*

The annealing dependent visual and light scattering experimental results were in marked contrast with emission spectroscopic experiments. Spectroscopic measurements indicated that distinct condensed phase transformations enroute to crystallization occurred at much lower annealing temperatures than indicated by light scattering experiments. The effects of annealing on the emission spectra of vapor-quenched films of BZP and BZP-d_{10} are presented below.

The phosphorescence emission spectrum of as-deposited,

Figure 10. I_s from a BZP sample versus annealing temperature (in K) in the range 18 to 180 K. The intensity was measured at 15790 cm^{-1} with ±1 cm^{-1} slits. The error bars are on the order of the dot size and correspond to fluctuations in the noise level in the PMT resulting from intensity variations.
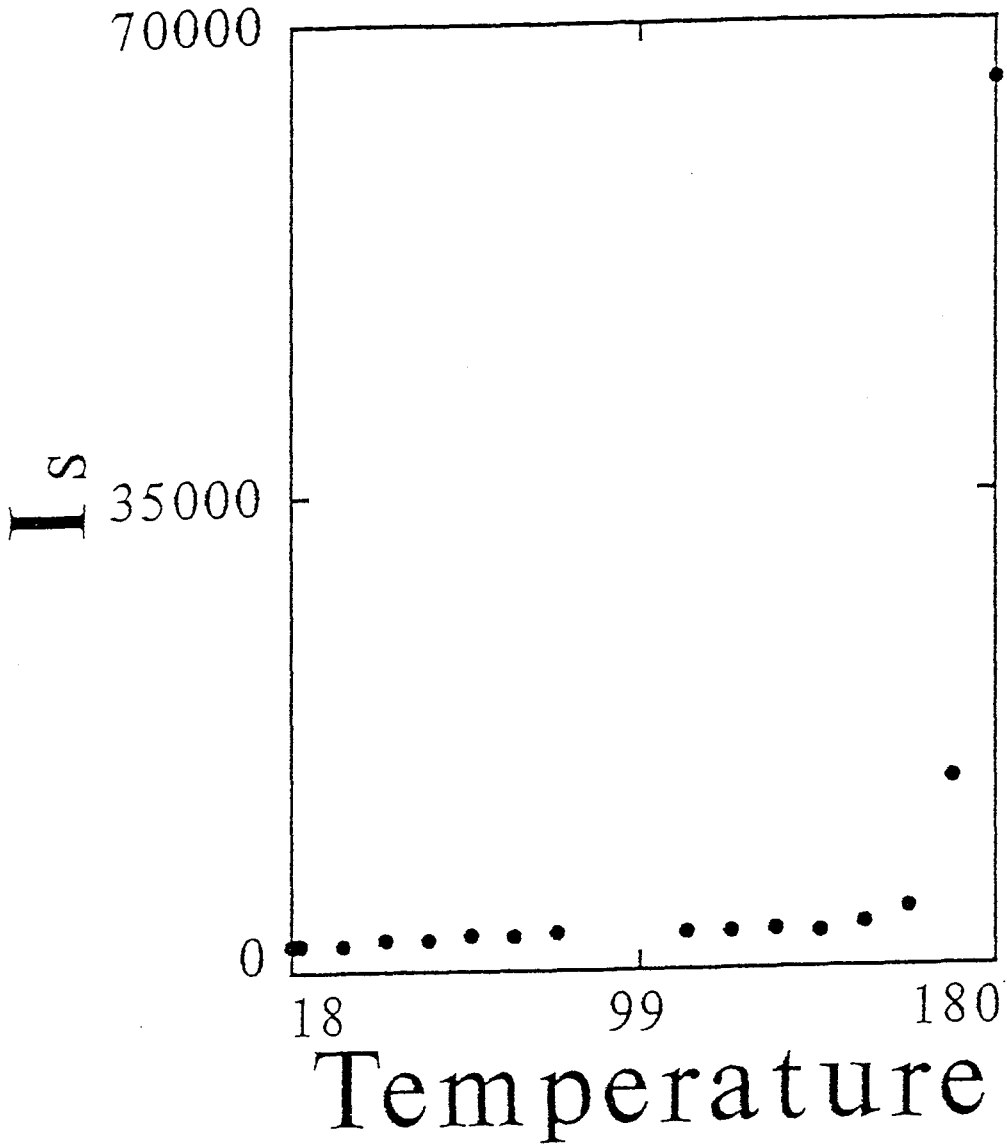
vapor-quenched BZP recorded at 18 K is illustrated in figure 11. The emission origin of the spectrum of lies at 23,602 cm^{-1}. The spectrum is characterized by a 1670 cm^{-1} interval vibrational progression. This progression can be observed up to the fifth overtone. It has been assigned to the 0-0 through 0-5 carbonyl stretching vibrations of BZP molecule. The bandwidths of the spectrum of figure 11 are relatively broad being of order 600 cm^{-1}.

Figure 12 illustrates the spectrum of as-deposited BZP-d_{10}. The conditions used to record the spectrum were the same as those used in figure 11. Figure 12 illustrates the similarity between the emission spectra of BZP and BZP-d_{10}.

The 18 K as-deposited phosphorescence emission spectrum of BZP was observed to be invariant for experiments using slightly different deposition parameters. However, the spectra did change in a number of respects as a function cyclic-annealing. For example, figure 13 allows comparison of the as-deposited sample spectrum of BZP with the spectrum of a sample annealed in the range 18 to 180 K. Comparison of the spectra reveal changes in the phosphorescence origin, band widths, and intensity distribution. Analogous data for BZP-d_{10} are presented in figure 14.

Figure 15 illustrates the changes observed in E_{max} for BZP upon annealing in the range 18 to 180 K. E_{max} increases from a minimum of 23,564 cm^{-1} to a maximum of 23,668 cm^{-1} in the annealing range 40 to 90 K. Figure 16 is the similar plot for

Figure 11. Xenon arc lamp induced phosphorescence spectrum of as-deposited, vapor-quenched BZP. The spectrum was recorded with a resolution of ± 28 cm^{-1} while the sample was held at 18 K.
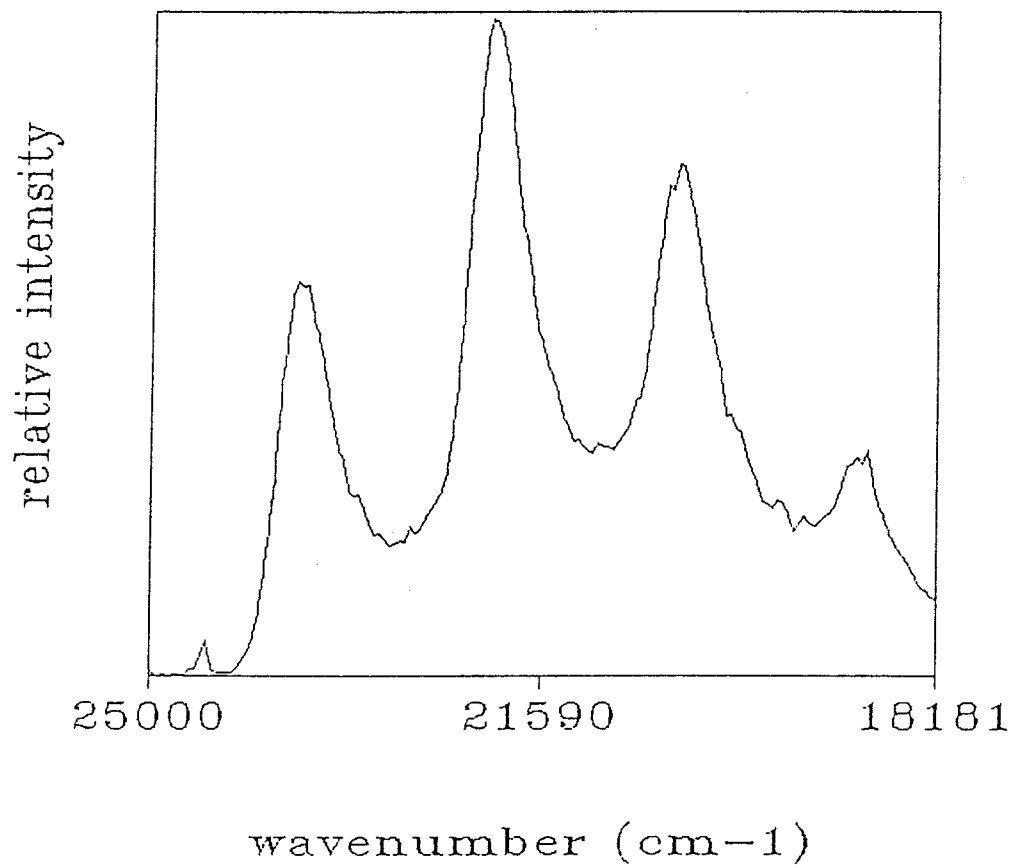
Figure 12. Xenon arc lamp induced phosphorescence spectrum of as-deposited vapor-quenched BZP-d_{10}. The spectrum was recorded with a resolution of ± 28 cm^{-1} while the sample was held at 18 K.
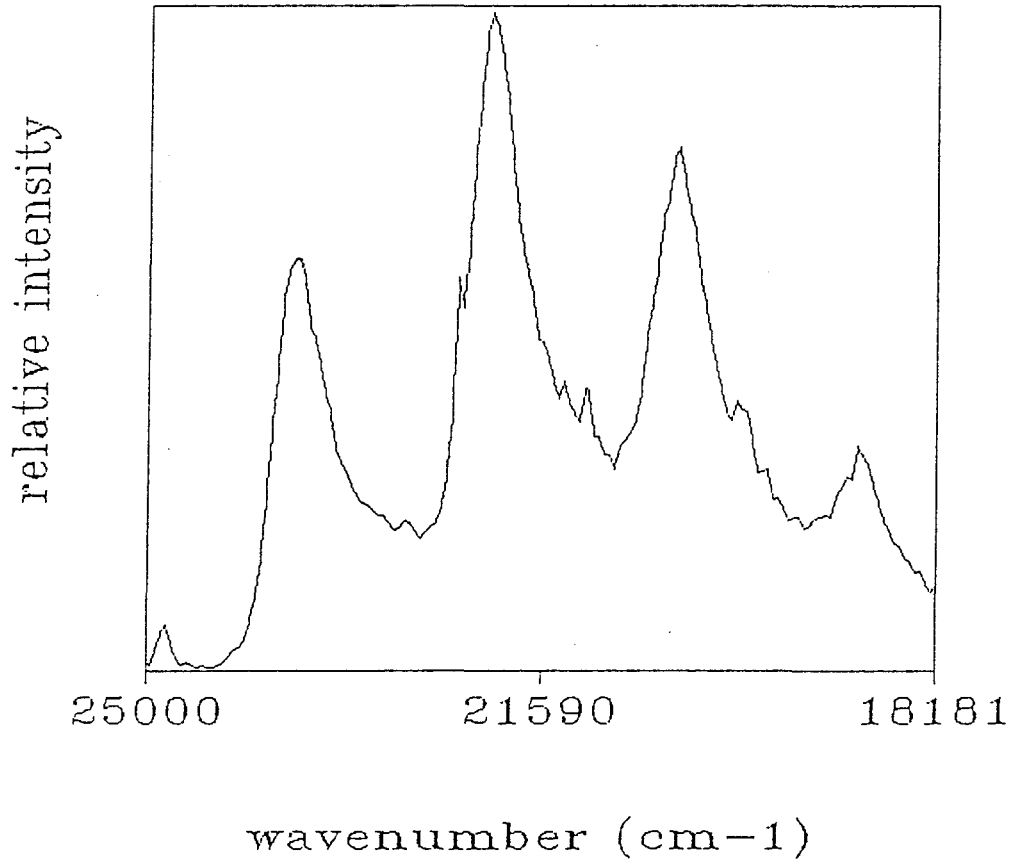
Figure 13. Xenon arc lamp induced phosphorescence spectrum of as-deposited (bottom) and annealed (top) BZP. The top spectrum resulted from annealing in 10 K increments in the range 20 to 180 K. A 2 K increment anneal took place in the range 18 to 20 K. The spectrum was recorded with a resolution of ±28 cm^{-1} while the sample was held at 18 K.

relative intensity

wavenumber (cm−1)

25000   21590   18181
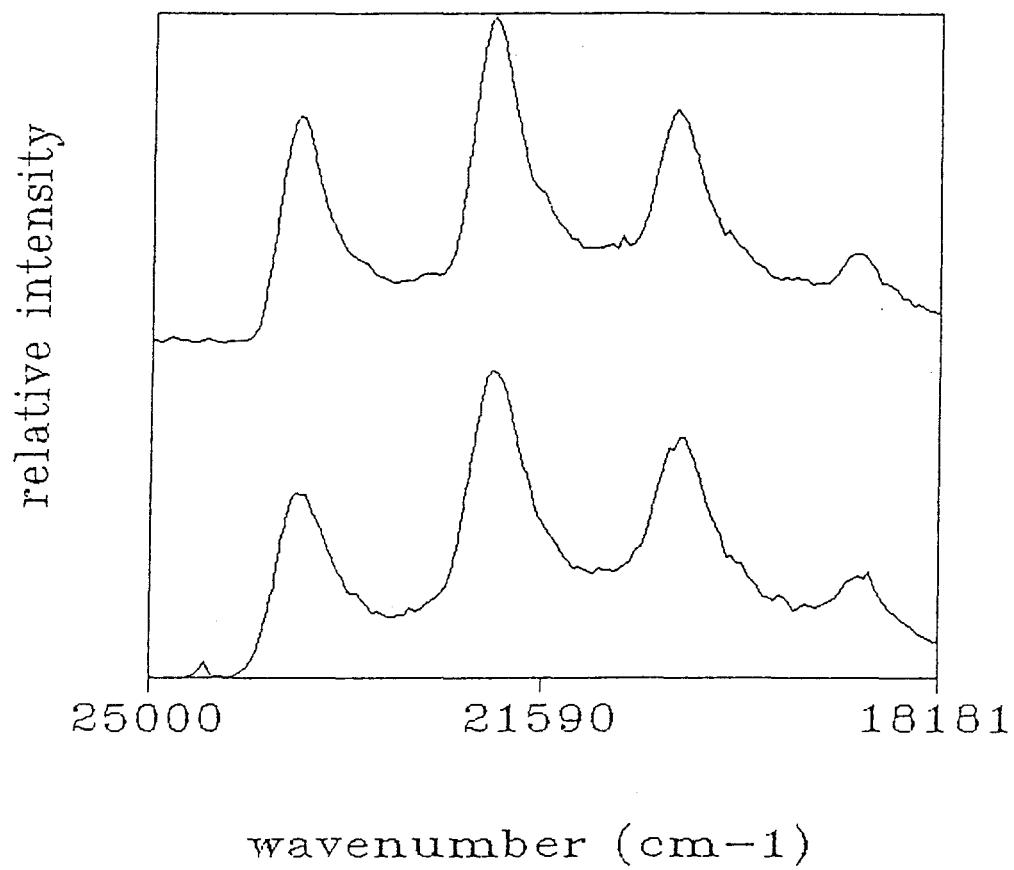
Figure 14. Xenon arc lamp induced phosphorescence spectrum of as-deposited (bottom) and annealed (top) BZP-d_{10}. The top spectrum resulted from annealing in 10 K increments in the range 20 to 180 K. A 2 K increment anneal took place in the range 18 to 20 K. The spectrum was recorded with a resolution of ±28 cm^{-1} while the sample was held at 18 K.

Figure 15. E_{max} (in cm^{-1}) of the 0-0 carbonyl vibrational band of BZP plotted versus annealing temperature (in K). Cyclic-annealing took place in 10 K increments in the range 20 to 180 K with a 2 K increment anneal in the range 18 to 20 K. The error bars are ±28 cm^{-1}. They represent the experimental uncertainty associated with the monochromator resolution.

Figure 16. E_{max} (in cm^{-1}) of the 0-0 carbonyl vibrational band of BZP-d_{10} plotted versus annealing temperature (in K). Cyclic-annealing took place in 10 K increments in the range 20 to 180 K with a 2 K increment anneal in the range 18 to 20 K. The error bars are ± 28 cm^{-1}. They represent the experimental uncertainty associated with the monochromator resolution.

the BZP-d_{10} sample. E_{max} also increases in the range 18 to 180 K. Specifically E_{max} changes from a minimum of 23,598 cm^{-1} to a maximum of 23,703 cm^{-1} with annealing in the range 30 to 120 K.

Figures 15 and 16 illustrate the similar behavior of E_{max} for BZP and BZP-d_{10} with cyclic annealing. For example, the maximum and minimum values of E_{max} are within experimental uncertainty for the two species and E_{max} increases with annealing temperature for both BZP and BZP-d_{10}. The primary difference between the two is that E_{max} increases over a larger cyclic-annealing range for the deuterated sample (30-120 K) than for BZP (40-90 K) under the same conditions.

Plots of E_{max} for BZP and BZP-d_{10} annealed in the range 18 to 50 K are shown in figures 17 and 18. Though measurable differences exist, no recognizable trends for either sample are observed.

The FWHM of BZP was affected by annealing temperature in the range 18 to 180 K in the manner illustrated in figure 19. The FWHM decreases from 625 to 526 cm^{-1} over the annealing range 40 to 120 K and remains relatively constant over the annealing range 120 to 180 K. The annealing behavior of the FWHM of BZP-d_{10} in the same annealing temperature range is illustrated in figure 20. The FWHM decreases gradually from 627 to 491 cm^{-1} in the annealing range of 30 to 160 K and remains constant in the annealing range 160 to 180 K.

Figures 19 and 20 together illustrate that there are

Figure 17. E_{max} (in cm^{-1}) of the 0-0 carbonyl vibrational band of BZP plotted versus annealing temperature (in K) in 2 K increments in the range 18 to 50 K. The error bars are ±28 cm^{-1}. They represent the experimental uncertainty associated with the monochromator resolution.
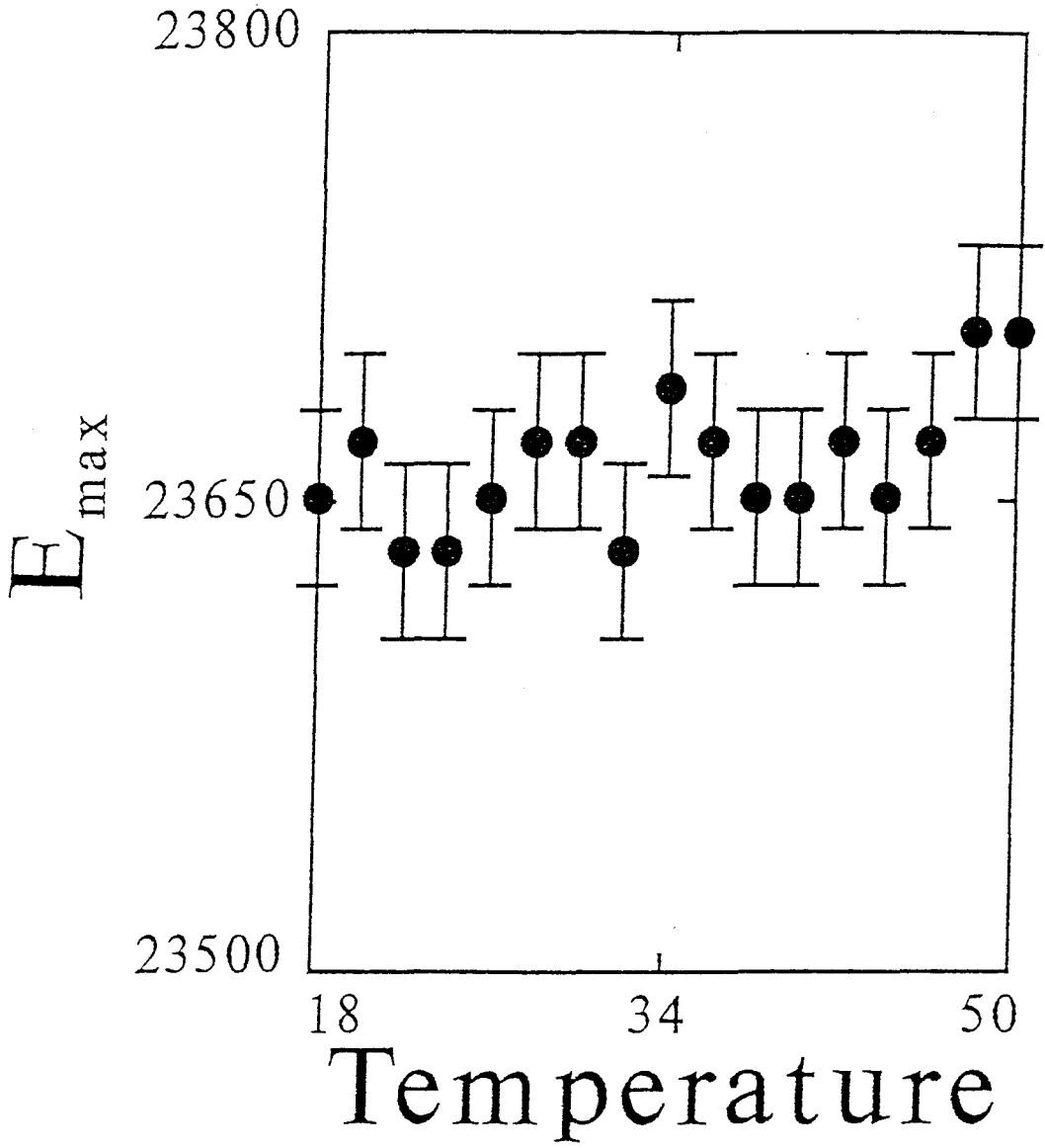
Figure 18. E_{max} (in $cm^{-1)}$ of the 0-0 carbonyl vibrational band of BZP-d_{10} plotted versus annealing temperature (in K) in 2 K increments in the range 18 to 50 K. The error bars are ±28 cm^{-1}. They represent the experimental uncertainty associated with the monochromator resolution.
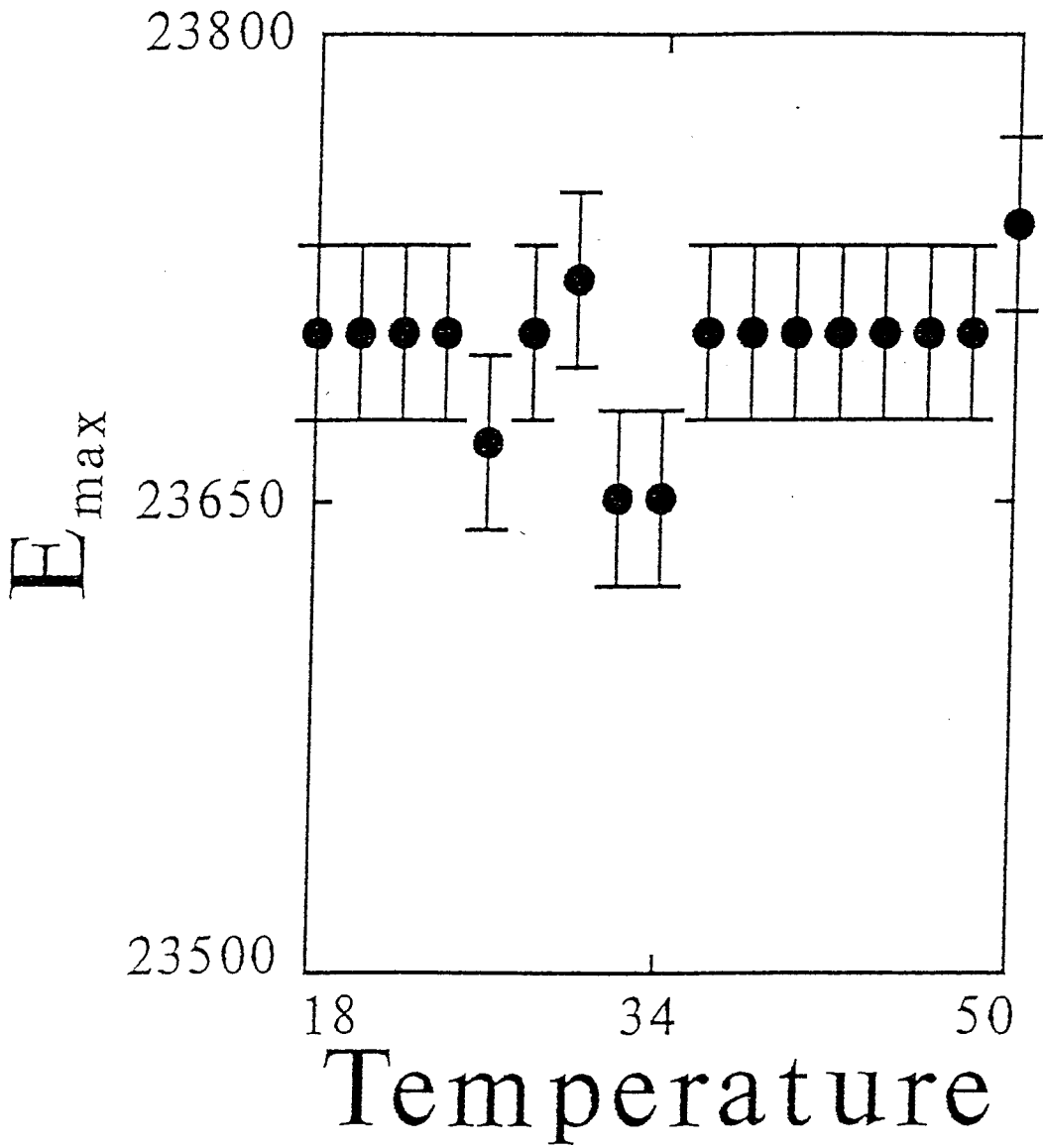
Figure 19. FWHM (in cm^{-1}) of the 0-0 carbonyl vibrational band of BZP plotted versus annealing temperature (in K). Cyclic-annealing took place in 10 K increments in the range 20 to 180 K with a 2 K increment anneal in the range 18 to 20 K. The error bars are ±28 cm^{-1}. They represent the experimental uncertainty associated with the resolution of the monochromator.
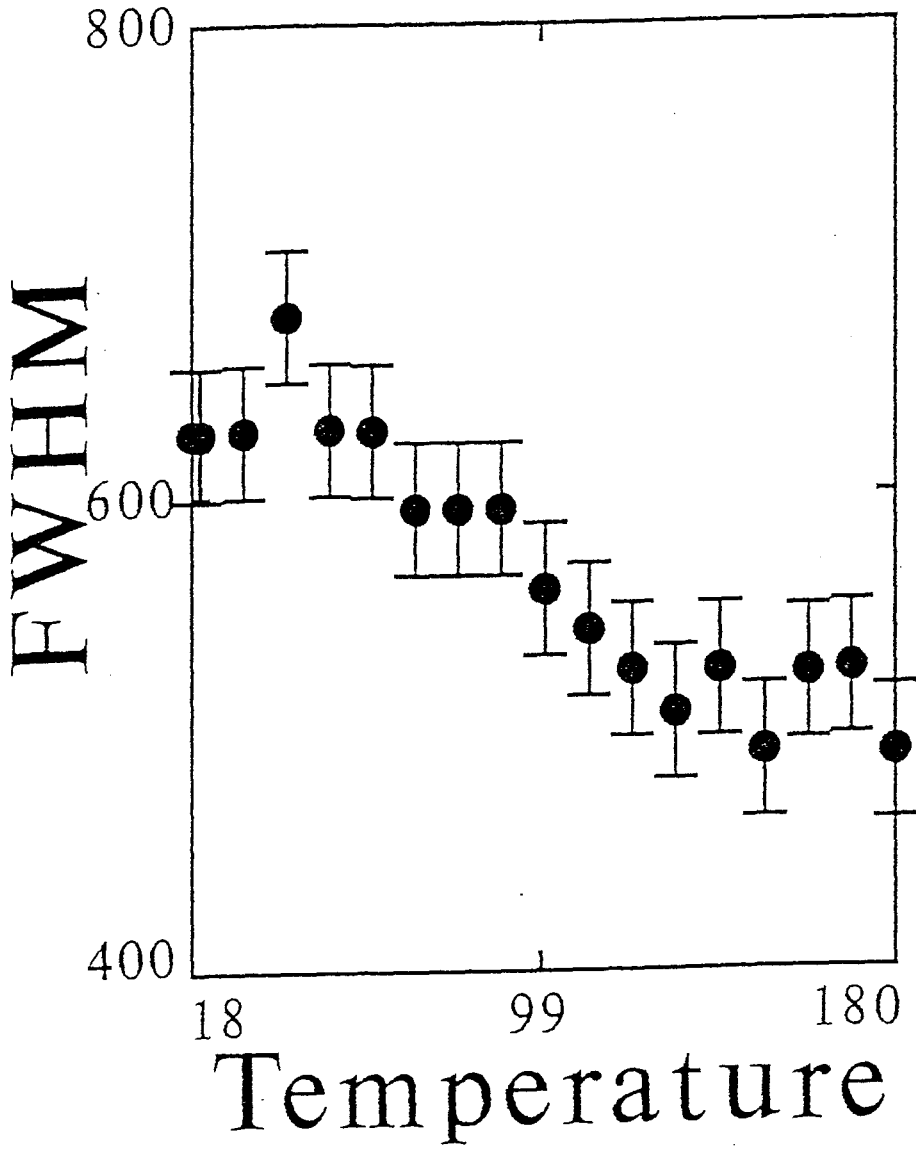
Figure 20. FWHM (in cm^{-1}) of the 0-0 carbonyl vibrational band of BZP-d_{10} plotted versus annealing temperature (in K). Cyclic-annealing took place in 10 K increments in the range 20 to 180 K and a 2 K increment anneal in the range 18 to 20 K. The error bars are ±28 cm^{-1}. They represent the experimental uncertainty associated with the resolution of the monochromator.
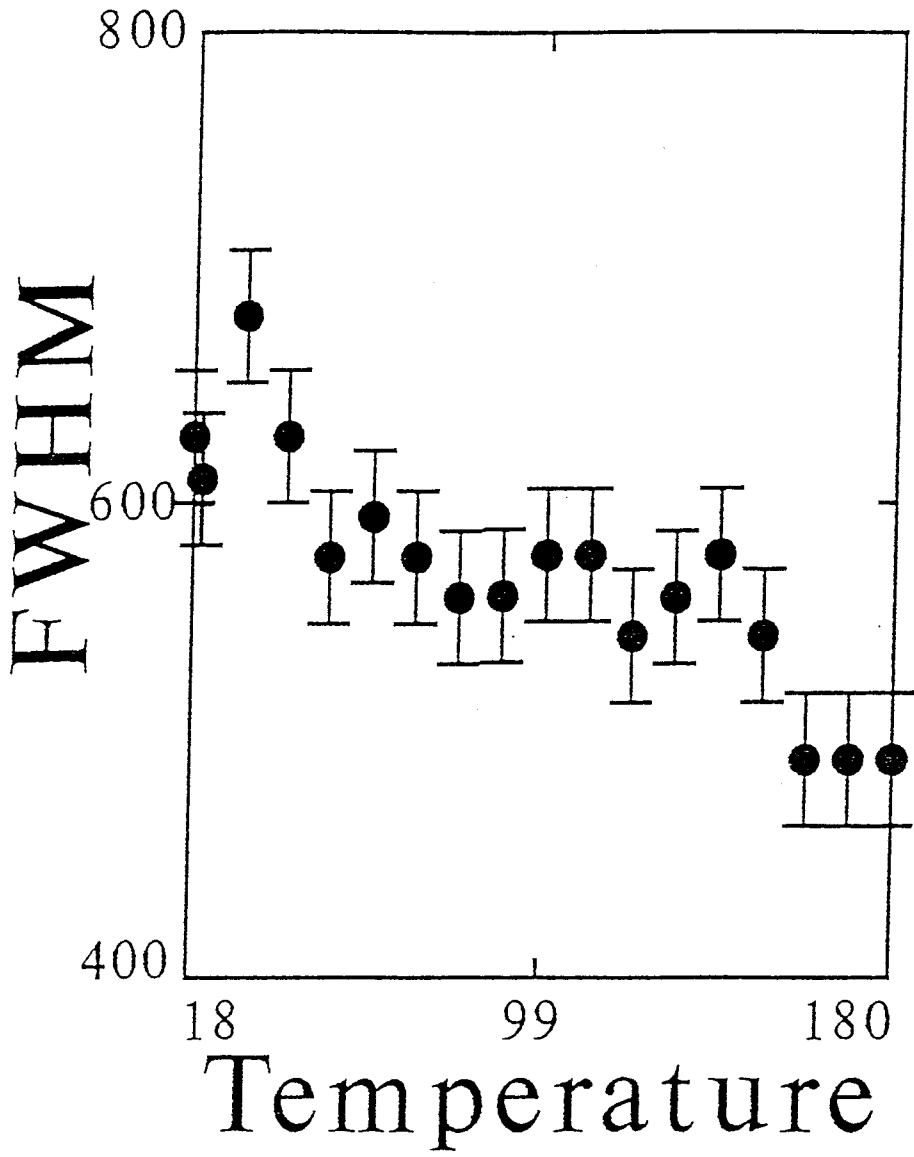
similarities in the annealing behavior of the FWHM of BZP and BZP-d_{10}. For example, the difference between the maximum and minimum values of the FWHM are the same within experimental error for both species over the annealing temperature range. The most distinct difference in the annealing behavior is that the FWHM of BZP-d_{10} appears to decrease over a larger temperature range (30-160 K) than the FWHM of BZP (40-120 K).

The FWHM was determined from sample spectra which were annealed in the range 18 to 50 K. Plots of the FWHM for annealed BZP and BZP-d_{10} between 18 and 50 K are shown in figures 21 and 22. Under these conditions, there is very little change in the FWHM of either species.

Changes in the intensity distribution of the BZP and BZP-d_{10} spectra with annealing temperature could be summarized in a number of different ways. For the purpose of this project, the changes in intensity distribution were characterized by measuring the change in intensity of the 0-2 band relative to that of the 0-0 band (I_{0-2}/I_{0-0}). This particular quantity was significant because in a high quality single crystal of BZP the ratio I_{0-2}/I_{0-0} is less than one. However, for vapor-quenched BZP the ratio is always greater than one. This relationship is somewhat unique for these two bands since the other bands appear more similar in intensity relative to the 0-0 vibrational band for both a high quality crystal and vapor quenched BZP. Figure 23 illustrates the changes in I_{0-2}/I_{0-0} for BZP with cyclic-annealing in the range
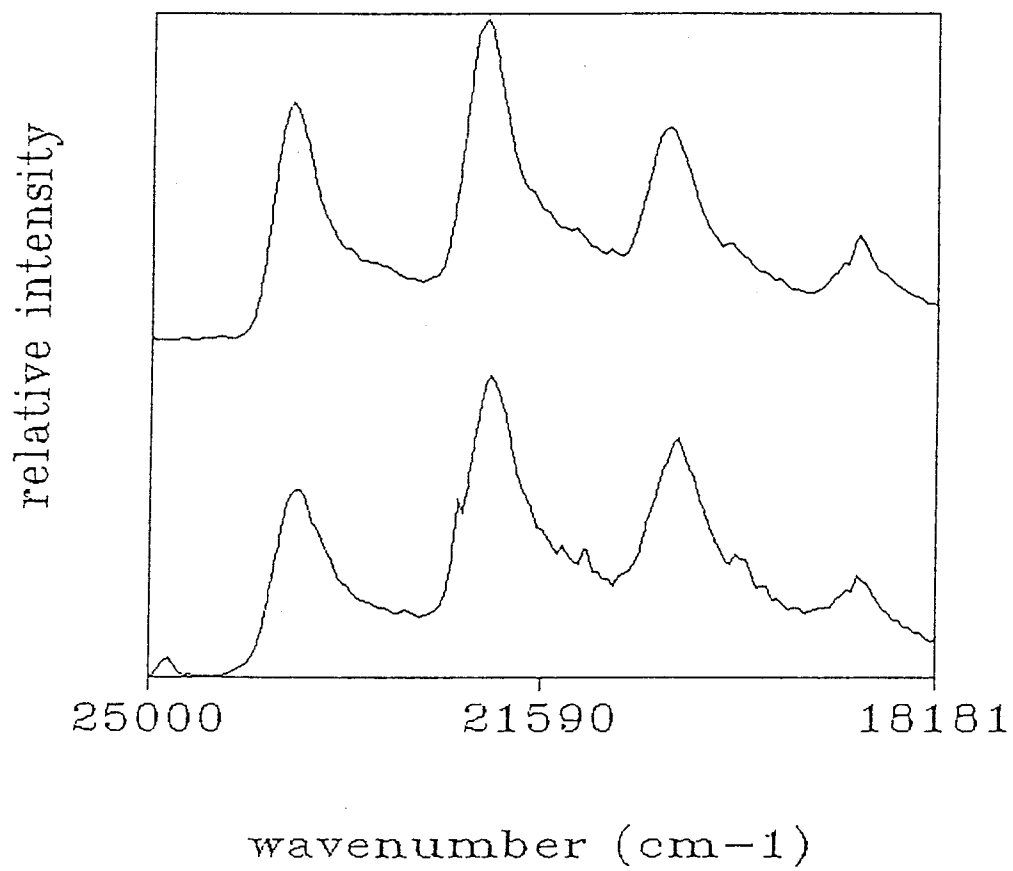
Figure 21. FWHM (in cm^{-1}) of the 0-0 carbonyl vibrational band of BZP plotted versus annealing temperature (in K) in 2 K increments in the range 18 to 50 K. The error bars are ±28 cm^{-1}. They represent the experimental uncertainty associated with the resolution of the monochromator.

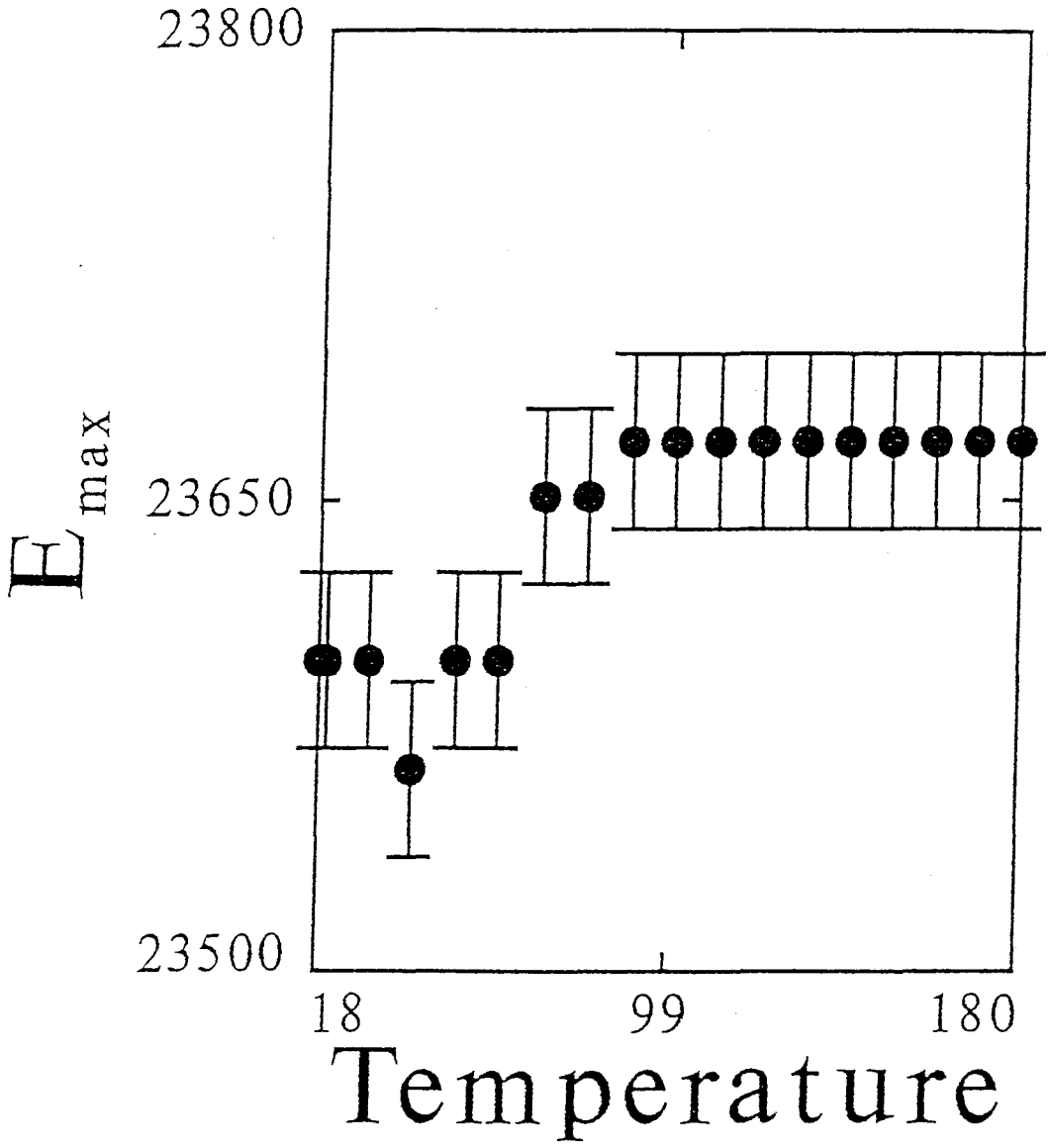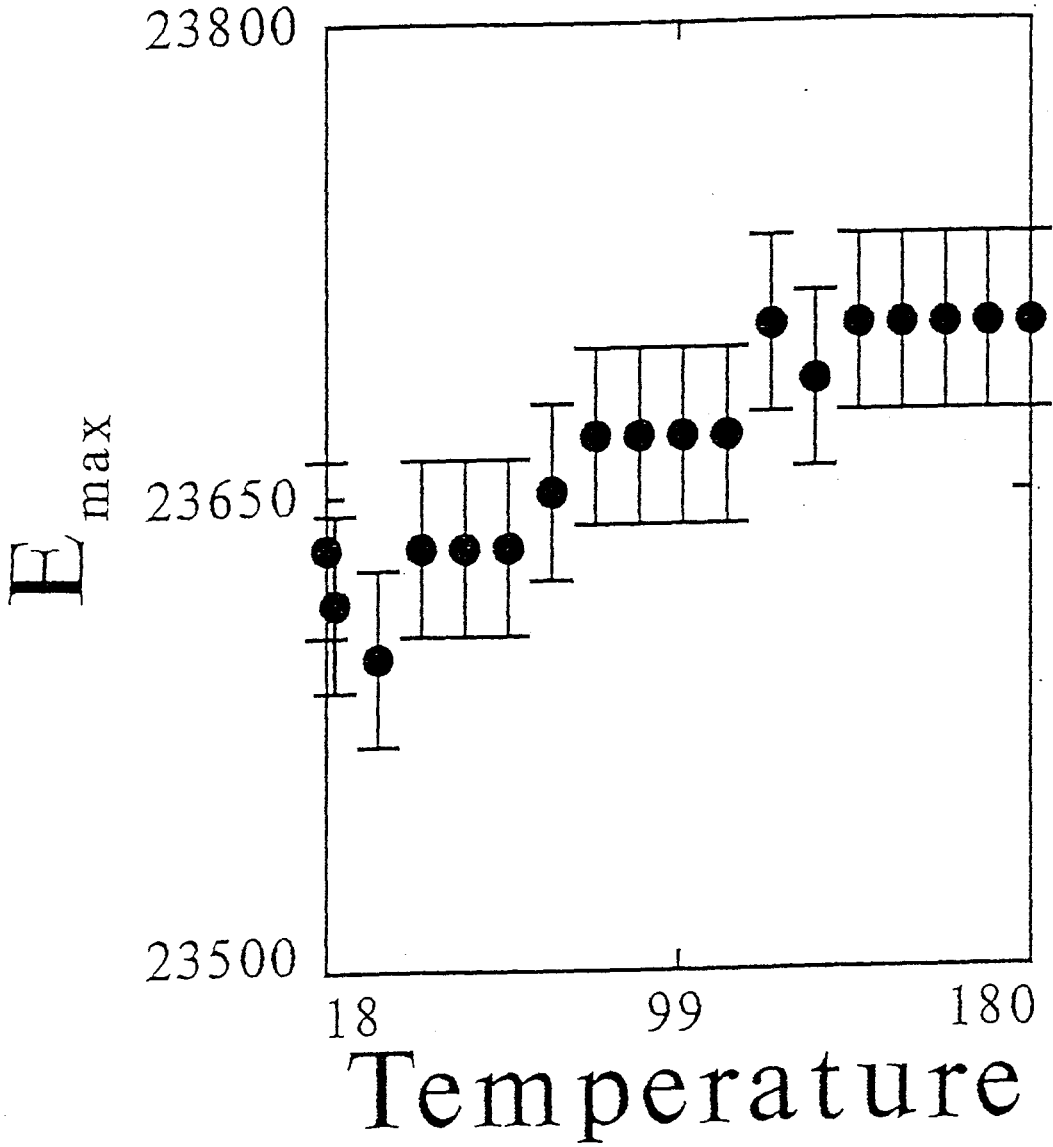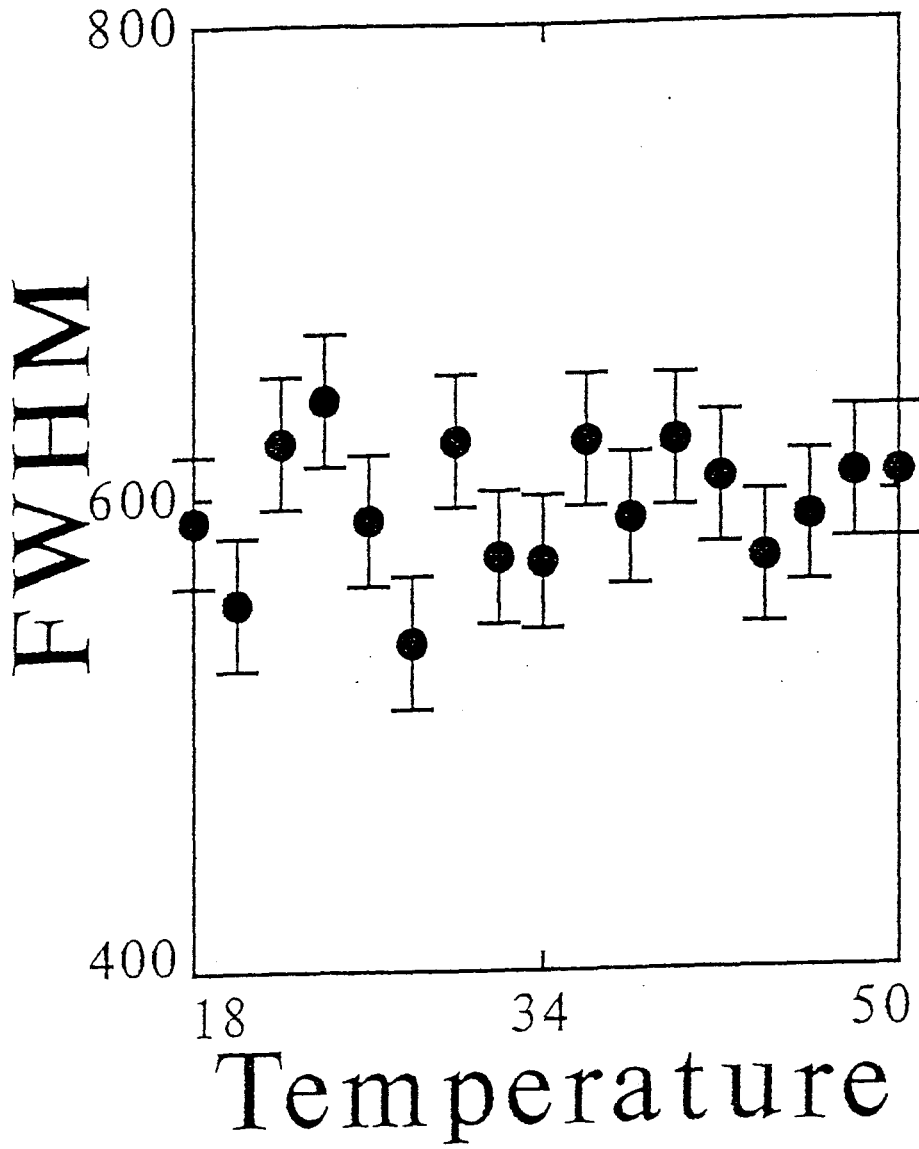Figure 22. FWHM (in cm^{-1}) of the 0-0 carbonyl vibrational band of BZP-d_{10} plotted versus annealing temperature (in K) in 2 K increments in the range 18 to 50 K. The error bars are ±28 cm^{-1}. They represent the experimental uncertainty associated with the resolution of the monochromator.

Figure 23. I_{0-2}/I_{0-0} for BZP plotted versus annealing temperature (in K). Cyclic-annealing took place in 10 K increments in the range 20 to 180 K with a 2 K increment anneal in the range 18 to 20 K. The uncertainty in the measurement is on the order of the dot size. The uncertainty corresponds to the fluctuations in the noise level in the PMT resulting from intensity variations.
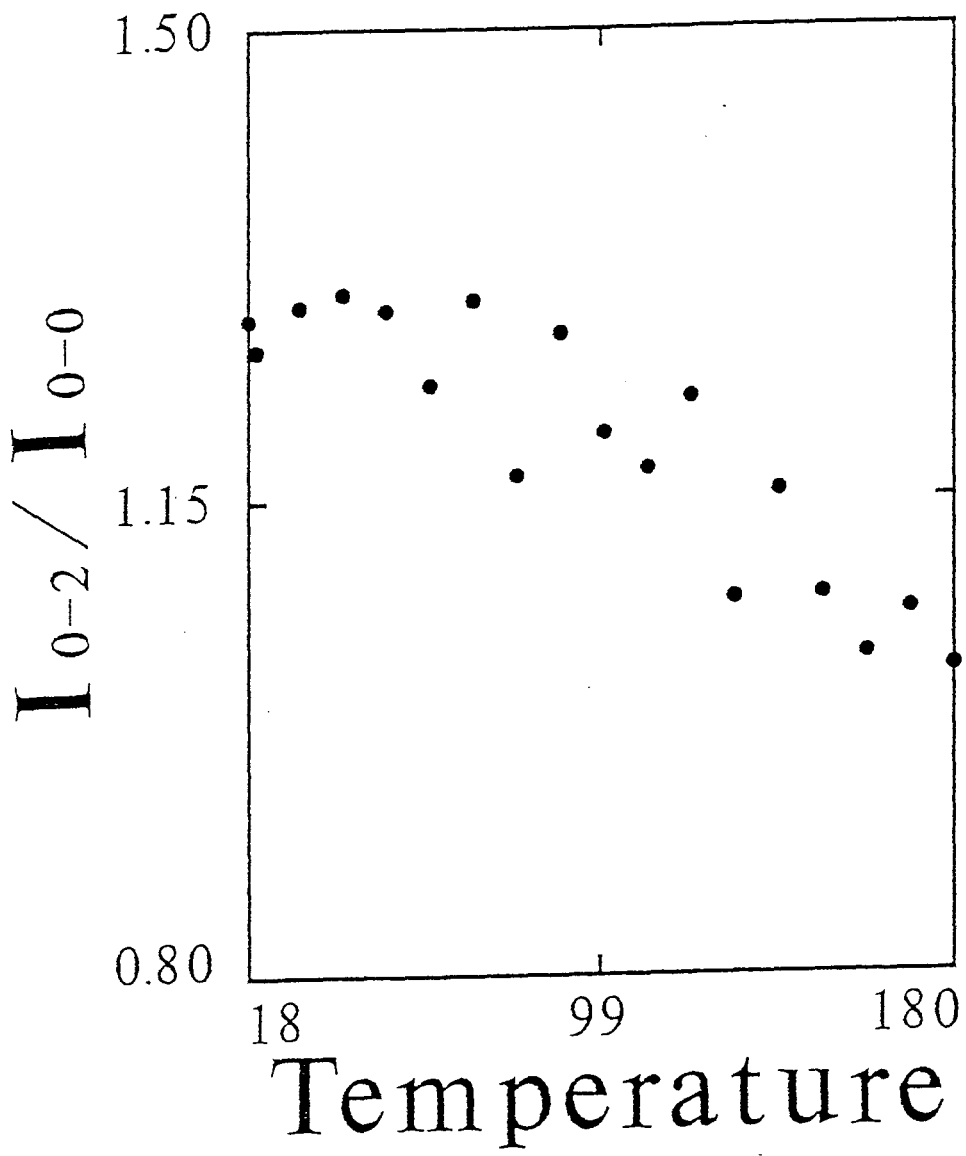
18 to 180 K. I_{0-2}/I_{0-0} remains essentially constant with annealing in the range 18 to 50 K and fluctuates in the annealing range 50 to 180 K with an overall decreasing trend.

The annealing dependent behavior of I_{0-2}/I_{0-0} for vapor-quenched BZP-d_{10} is illustrated in figure 24. I_{0-2}/I_{0-0} is essentially constant with annealing in the range 18 to 30 K and decreases steadily in the annealing range 30 to 180 K.

Figures 23 and 24 illustrate the similarities and differences in I_{0-2}/I_{0-0} for the two species. I_{0-2}/I_{0-0} for BZP and BZP-d_{10} are similar in that they both decrease with annealing. The primary difference between the two plots is that I_{0-2}/I_{0-0} for BZP-d_{10} changes by a larger amount with annealing in the range 18 to 180 K. The minimum value of the ratio is .89 for BZP-d_{10} and 1 for BZP.

Plots of I_{0-2}/I_{0-0} for BZP and BZP-d_{10} annealed in the range 18 to 50 K are shown in figures 25 and 26. In contrast to the 18 to 180 K annealing experiments, no apparent trend in I_{0-2}/I_{0-0} for BZP emerges as the sample is annealed in the range 18 to 50 k. For the BZP-d_{10} sample I_{0-2}/I_{0-0} experiences large fluctuations with a decreasing trend in the annealing range 18 to 50 K. The most outstanding difference between the plots is that I_{0-2}/I_{0-0} decreases over the annealing range for BZP-d_{10} but not for BZP.

Figure 27 illustrates the behavior of the total integrated intensity of the BZP sample spectrum between 25,000 and 18,181 cm^{-1} (I_{tot}) with annealing in the 18 to 180 K range.

Figure 24. I_{0-2}/I_{0-0} for BZP-d_{10} plotted versus annealing temperature (in K). Cyclic-annealing took place in 10 K increments in the range 20 to 180 K with a 2 K increment anneal in the range 18 to 20 K. The uncertainty in the measurement is on the order of the dot size. The uncertainty corresponds to the fluctuations in the noise level in the PMT resulting from intensity variations.
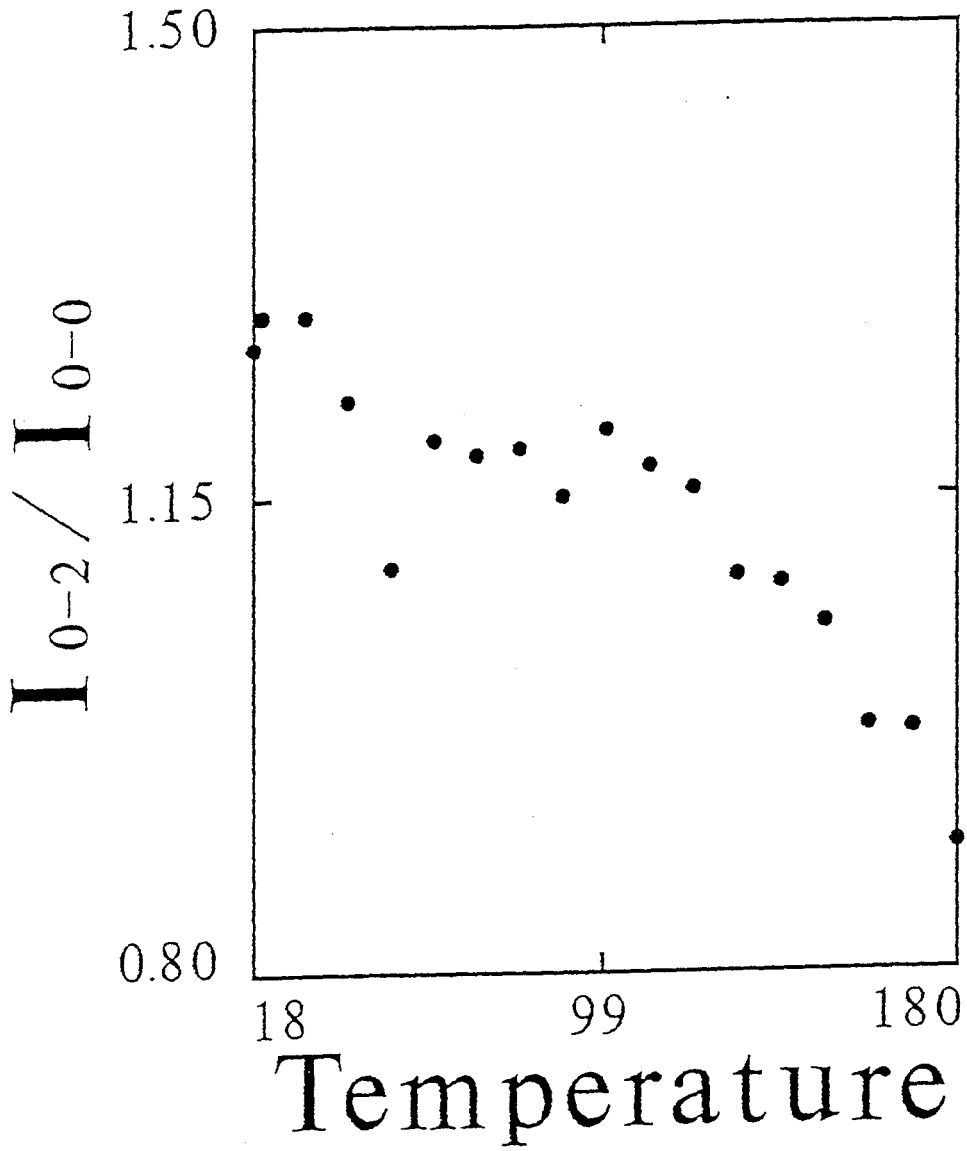
Figure 25. I_{0-2}/I_{0-0} for BZP plotted versus annealing temperature (in K) in 2 K increments in the range 18 to 50 K. The uncertainty in the measurement is on the order of the dot size. The uncertainty corresponds to the fluctuations in the noise level in the PMT resulting from intensity variations.
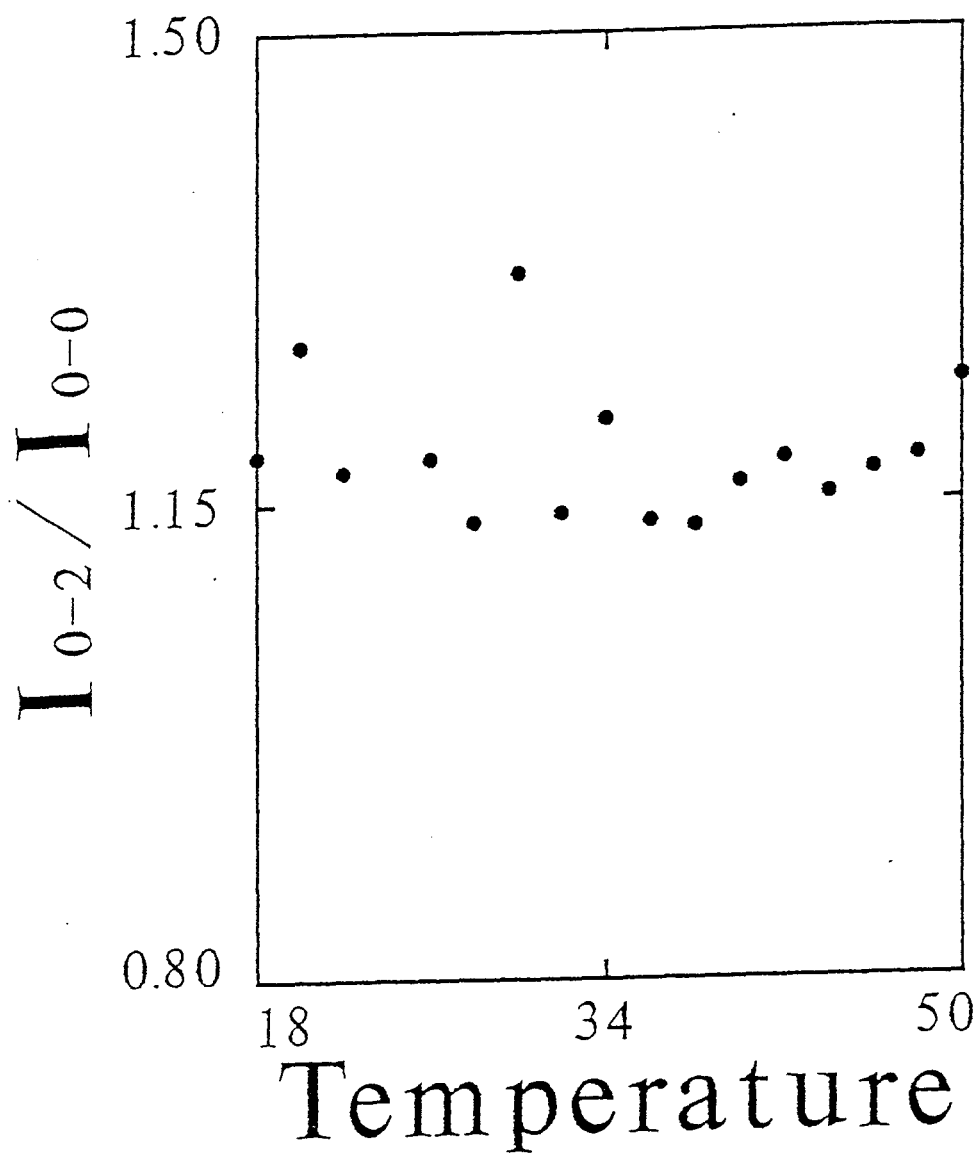
Figure 26. I_{0-2}/I_{0-0} for BZP-d_{10} plotted versus annealing temperature (in K) in 2 K increments in the range 18 to 50 K. The uncertainty in the measurement is on the order of the dot size. The uncertainty corresponds to the fluctuations in the noise level in the PMT resulting from intensity variations.
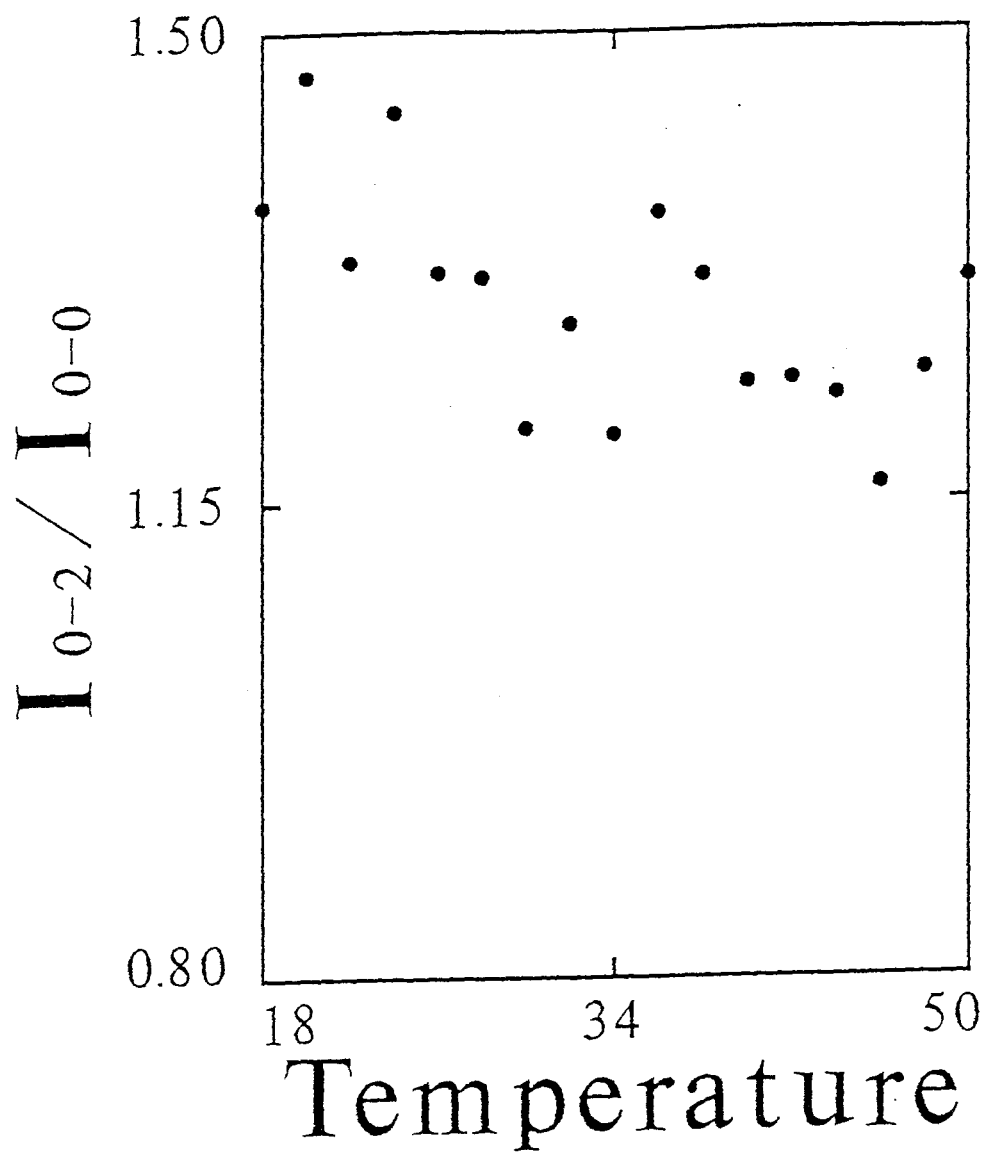
Figure 27. I_{tot} of BZP between 25,000 cm^{-1} and 18,181 cm^{-1} plotted versus annealing temperature (in K). Cyclic-annealing took place in 10 K increments in the range 20 to 180 K with a 2 K increment anneal in the range 18 to 20 K. The uncertainty of each point is on the order of the dot size. The uncertainty corresponds to the fluctuations in the noise level in the PMT resulting from intensity variations.
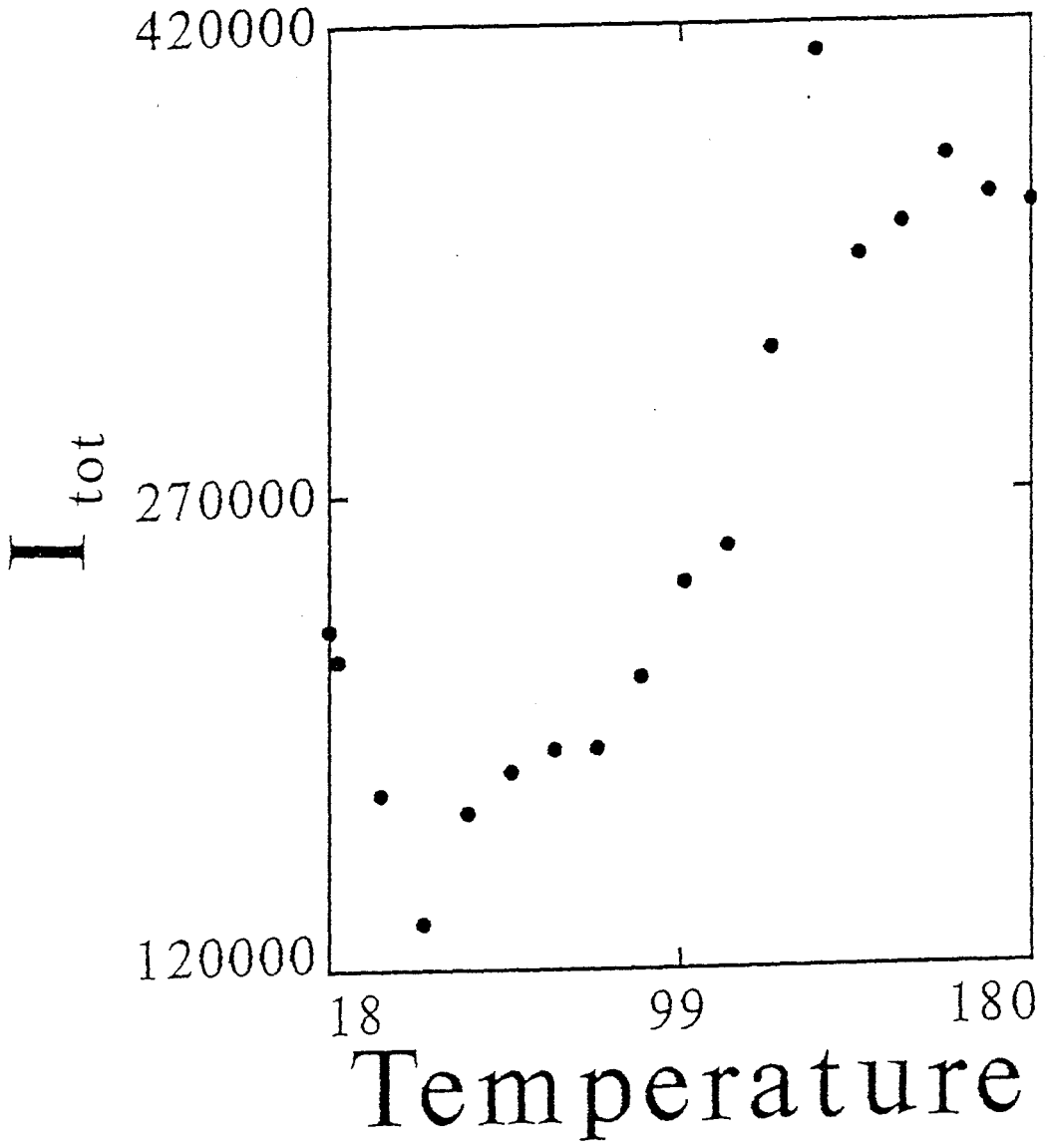
I_{tot} decreases in the annealing range of 18 to 40 K and increases in the annealing range 40 to 180 K.

Figure 28 demonstrates the annealing behavior of I_{tot} for BZP-d_{10}. I_{tot} decreases with annealing in the 18 to 40 K range and then increases in the range 40 to 180 K.

The behavior of I_{tot} is similar for both species as illustrated upon comparison of figures 27 and 28. The primary difference between the two species is that the change of I_{tot} with annealing temperature is much larger for BZP than BZP-d_{10} in the range 40 to 180 K.

Figure 29 shows the behavior of I_{tot} for BZP with cyclic annealing in the range 18 to 50 K. I_{tot} for BZP decreases in the annealing range 10 to 38 K and increases in the annealing range 38 to 50 K. The value of I_{tot} for the 50 K anneal is less than I_{tot} for the as-deposited sample spectrum of BZP.

Figure 30 illustrates a similar plot for BZP-d_{10}. I_{tot} decreases in the range 18 to 36 K, and increases in the annealing range 36 to 50 K. I_{tot} for the 50 K anneal is less than I_{tot} for the as-deposited BZP-d_{10} sample spectrum.

The behavior of I_{tot}, upon comparison of figures 29 and 30, is seen to be very similar for both BZP and BZP-d_{10}. There are no large differences between I_{tot} for BZP and BZP-d_{10} at these low temperature anneals. I_{tot} for both samples annealed in the range 18 to 50 K appears to demonstrate similar behavior compared to the samples annealed in the range 18 to 180 K.

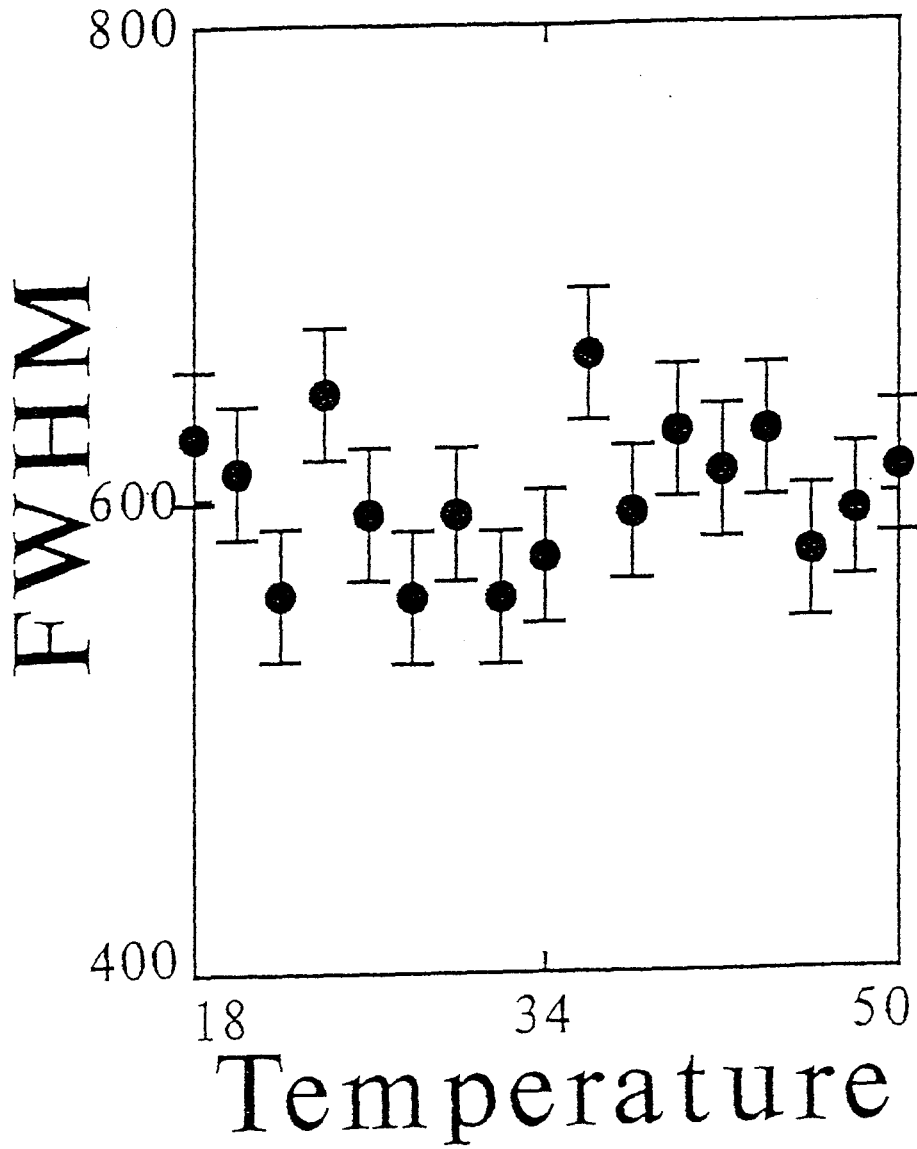Figure 28. I_{tot} of BZP-d_{10} between 25,000 cm^{-1} and 18,181 cm^{-1} plotted versus annealing temperature (in K). Cyclic-annealing took place in 10 K increments in the range 20 to 180 K with a 2 K increment anneal in the range 18 to 20 K. The uncertainty of each point is on the order of the dot size. The uncertainty corresponds to the fluctuations in the noise level in the PMT resulting from intensity variations.
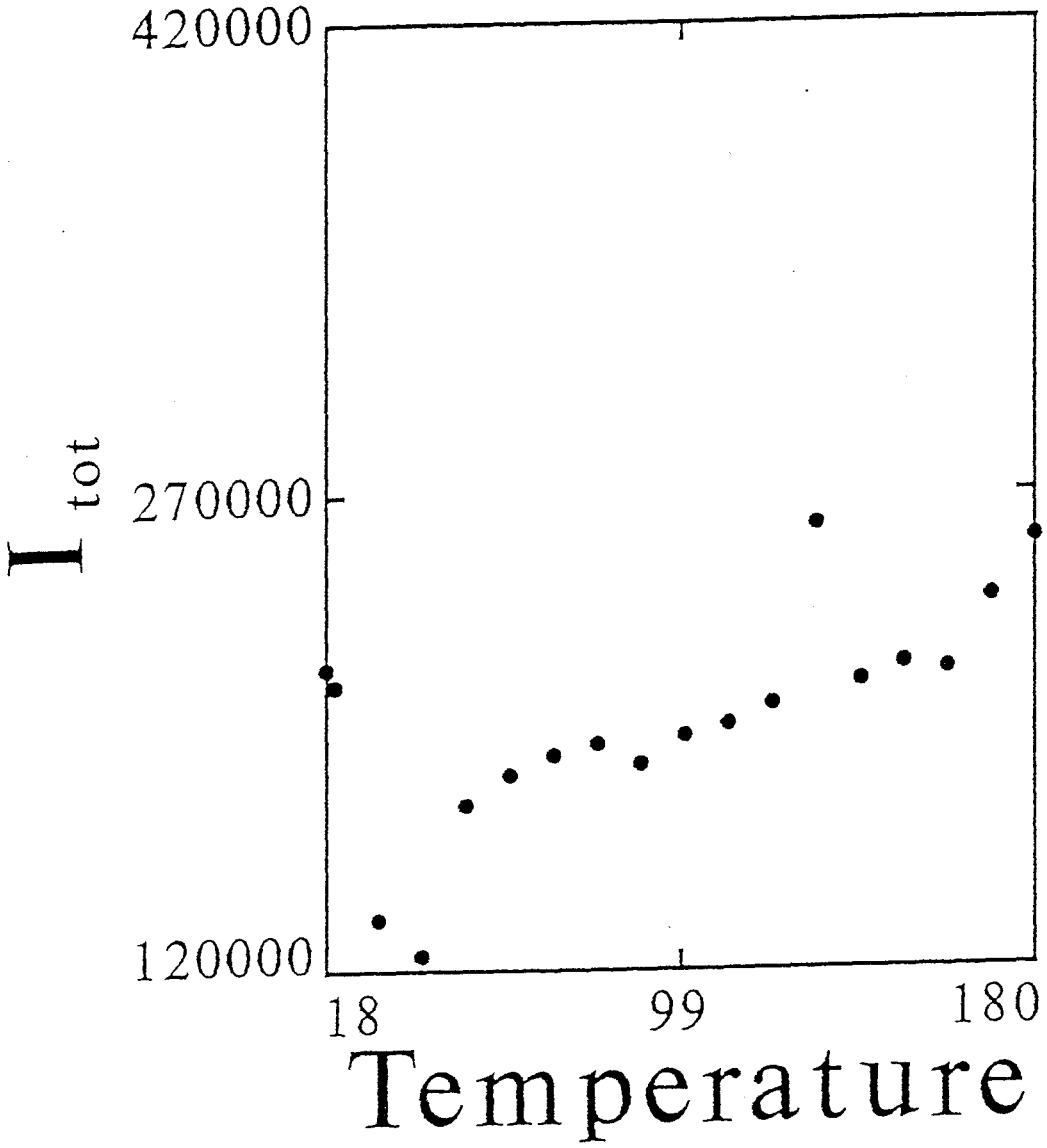
Figure 29. I_{tot} of BZP between 25,000 cm^{-1} and 18,181 cm^{-1} versus annealing temperature (in K) in 2 K increments in the range 18 to 50 K. The uncertainty of each point is on the order of the dot size. The uncertainty corresponds to the fluctuations in the noise level in the PMT resulting from intensity variations.
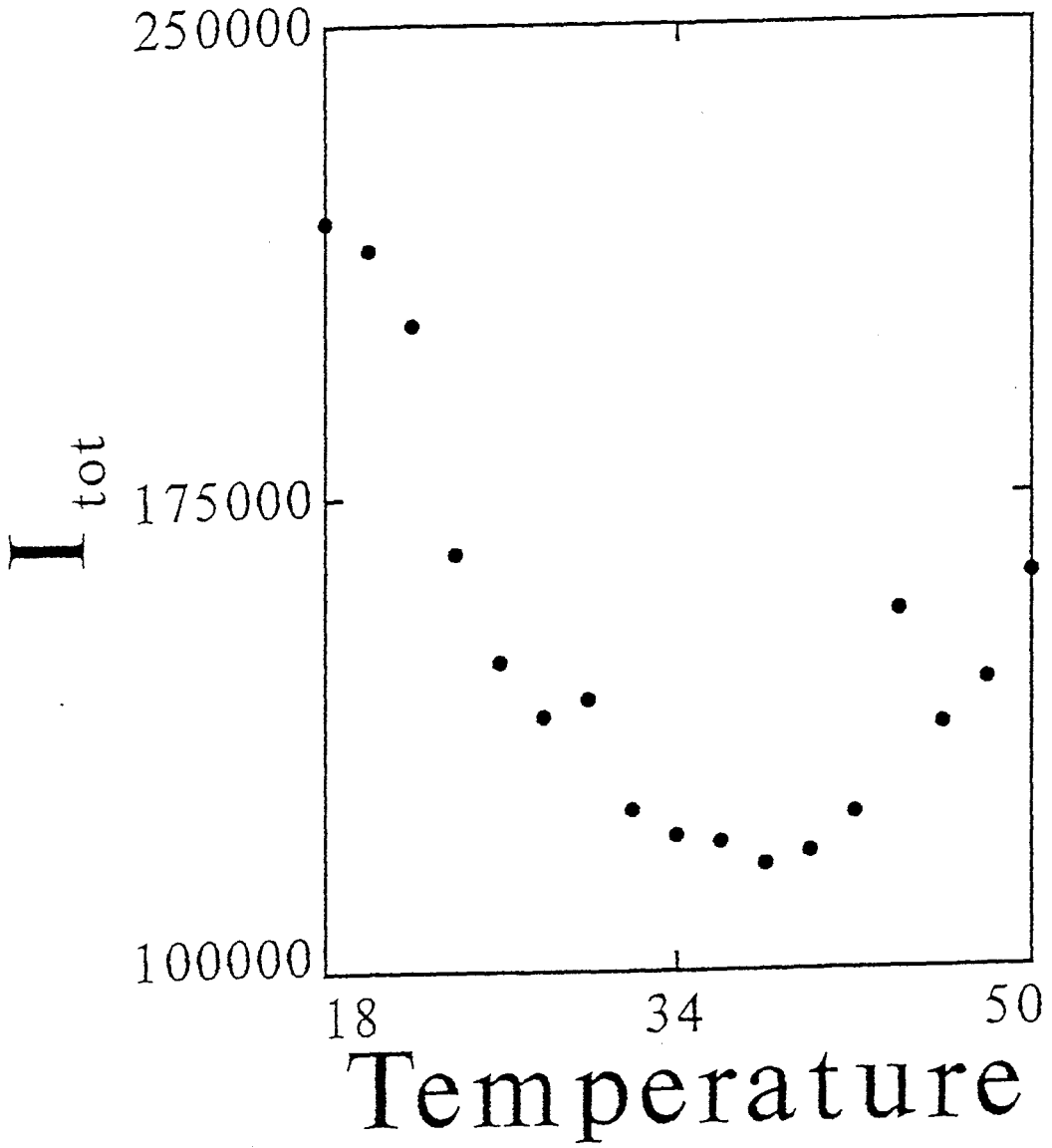
Figure 30. I_{tot} of BZP-d_{10} between 25,000 cm^{-1} and 18,181 cm^{-1} versus annealing temperature (in K) in 2 K increments in the range 18 to 50 K. The uncertainty of each point is on the order of the dot size. The uncertainty corresponds to the fluctuations in the noise level in the PMT resulting from intensity variations.
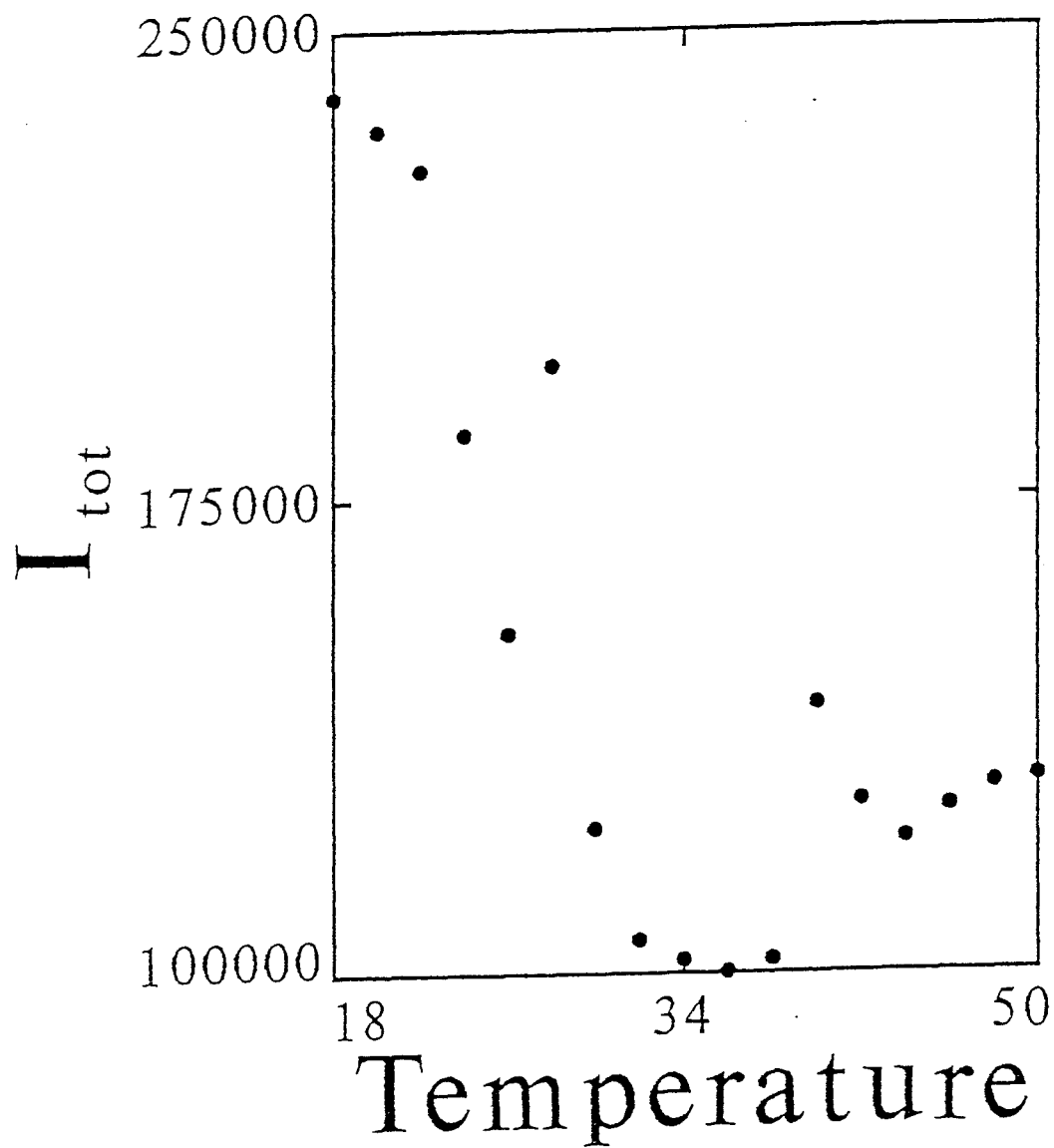
The data presented in this section concern selected experiments of which many were carried out. Given the experimental set-up and techniques, certain variations did occur, particularly with respect to nozzle angle and heating rates. Variations of the nozzle position were of order $\pm 5°$ and variations in the time required to reach the peak annealing temperature were ± 30 sec. These differences are not large. But they are observed to lead to slightly different experimental results for repeated annealing experiments. For example, the magnitude of any given data point, including experimental uncertainty of the data of different experiments, were different by as much as 5%. However, the functional dependencies of the data presented in this thesis on annealing temperature appears to be the same between any two experiments. Apparent differences are important in that they indicate a certain sensitivity of crystallization to initial conditions and the time frame of each annealing cycle. On the other hand, the similarities in the functional dependencies of the data demonstrate that actual trends are evidenced by the parameters concerning the crystallization of BZP.

3. *Time-resolved and High Temperature Spectra / Annealing Behavior*

a. *Time-Resolved Spectra*

Time resolved spectra were recorded for as-deposited and cyclic-annealed, vapor-quenched films of BZP at 18 K. The time resolved spectrum of BZP was observed to depend on the delay time and annealing temperature.

Figure 31 shows the spectrum of as-deposited BZP recorded at 18 K with a time delay of 400 ns with respect to the nitrogen laser pulse. Figure 32 (bottom spectrum) illustrates the as-deposited spectrum of BZP recorded with a 50 ms delay. In the delayed, as-deposited spectrum the carbonyl bands appear to be superimposed on a low intensity broad band. Figure 32 (top spectrum) illustrates the 50 ms delayed spectrum recorded after cyclic-annealing in the range 18 to 40 K. The spectra of figure 32 are similar to the spectrum in figure 31. For example, the spectra of both figures demonstrate the same carbonyl vibrational progression. The primary difference between the two 50 ms delayed spectra of figure 32 is that the intensity of the broad band relative to that of the carbonyl vibrational bands increases with annealing.

Figure 33 (bottom spectrum) illustrates the 50 ms delayed spectrum of BZP recorded after annealing in the range 40 to

Figure 31.   Pulsed nitrogen laser induced phosphorescence
spectrum of as-deposited BZP recorded with a 400 ns time delay
with respect to the laser firing.   The spectrum is recorded
with ±28 cm^{-1} resolution at a temperature of 18 K.
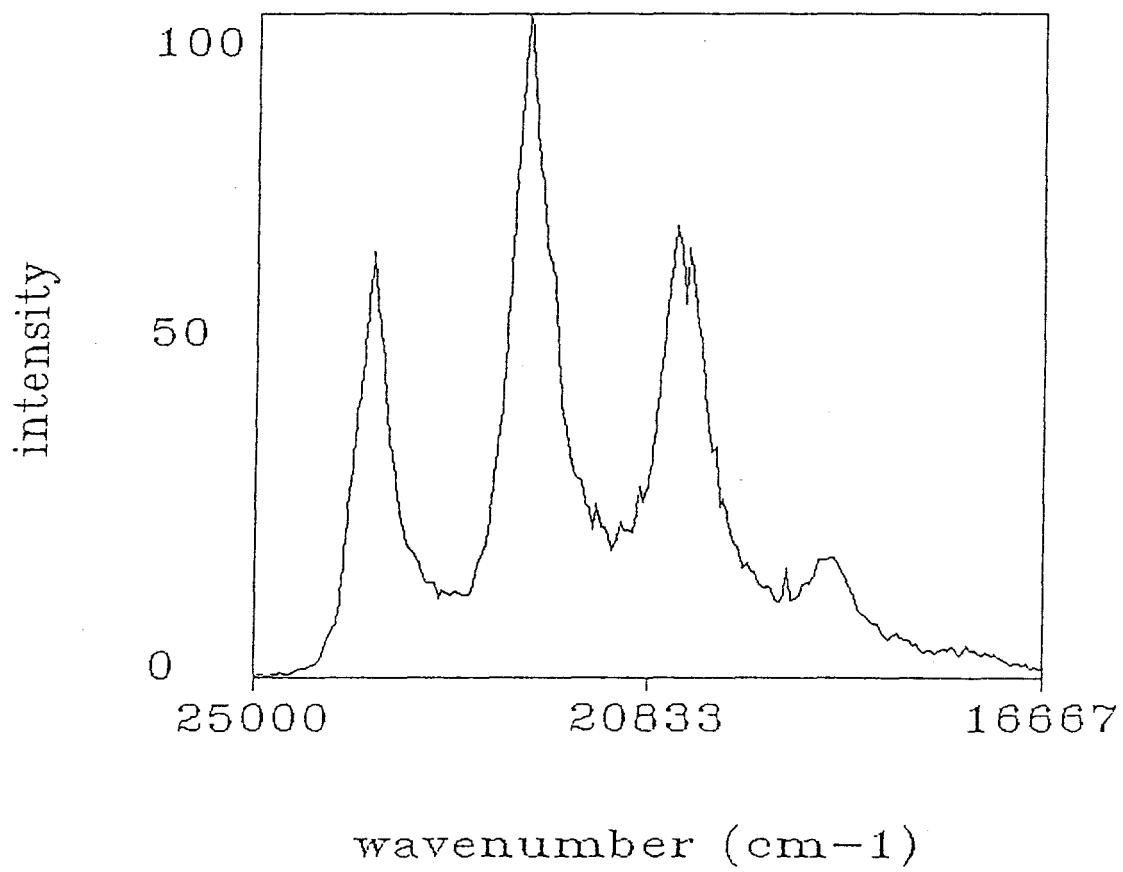
Figure 32.   Pulsed nitrogen laser induced phosphorescence spectrum recorded with a 50 ms time delay with respect to the laser pulse. The spectra are of the as-deposited (bottom) BZP sample and the result of annealing BZP in the range 18 to 40 K (top).   The spectra were recorded with ± 28 cm^{-1} resolution at a temperature of 18 K.   The noise is due to shot noise in the PMT.
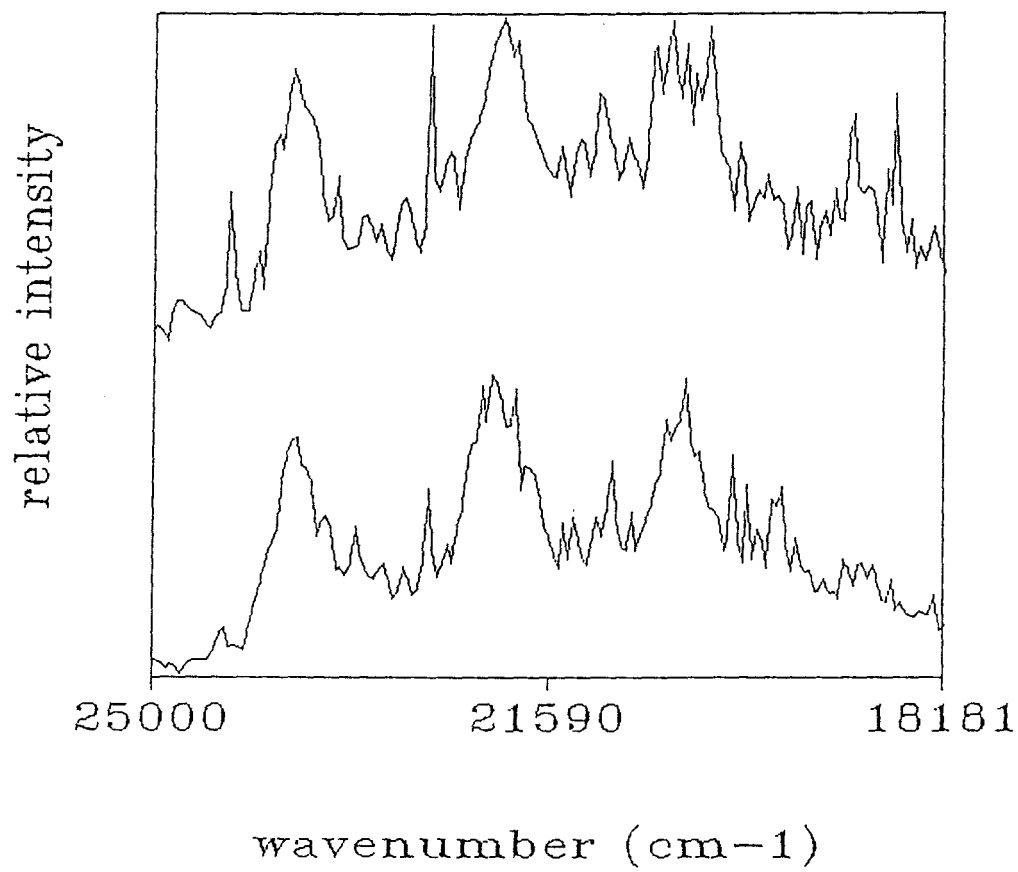
Figure 33. Pulsed nitrogen laser induced phosphorescence spectrum recorded with a 50 ms time delay with respect to the laser pulse. The spectra are of the 140 K (bottom) annealed and the 180 K annealed (top) BZP sample. The spectra were recorded with ±28 cm^{-1} resolution at a temperature of 18 K. The noise is due to shot noise in the PMT.
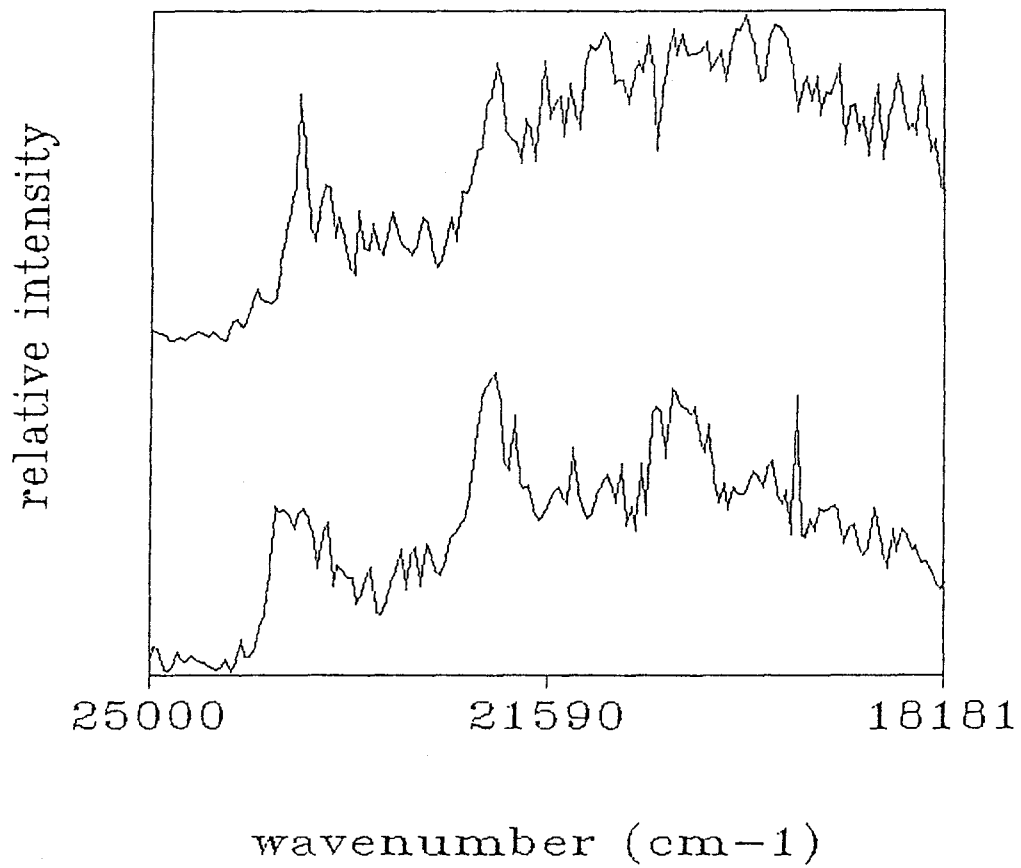
140 K. The top spectrum illustrates the 50 ms delayed spectrum of BZP subsequent to annealing in the 18 to 180 K range. The carbonyl vibrational bands are not evident in the top spectrum. The origin of the broad band is placed approximately 1800 cm^{-1} lower in energy than the 0-0 band. This is in the region where the broad band begins to rise.

Figures 32 and 33 illustrate that the broad band feature of the delayed spectra of BZP becomes more prominent with annealing in the range 18 to 180 K. This feature dominates the spectrum subsequent to the 180 K anneal.

b. High Temperature Spectra

In addition to the spectra recorded at 18 K as a function of cyclic-annealing temperature, spectra were recorded at elevated temperatures. For example, figure 34 illustrates the effects of elevated temperature on the spectrum of neat, vapor-quenched BZP. The spectrum was recorded at 140 K. The spectrum of figure 34 is broad band with no evidence of the carbonyl vibrational bands. It is very similar in appearance to the 50 ms delayed spectrum of figure 33 (top). The high temperature spectra of BZP-d_{10} behaved in the same manner as BZP.

The results of this section are from representative experiments. Variations of the relative intensity of the vibrational bands to that of the broad band in the time

Figure 34. Xenon arc lamp induced phosphorescence spectrum of vapor-quenched BZP held at a temperature of 140 K. The spectrum was recorded with a resolution of ± 28 cm^{-1}.
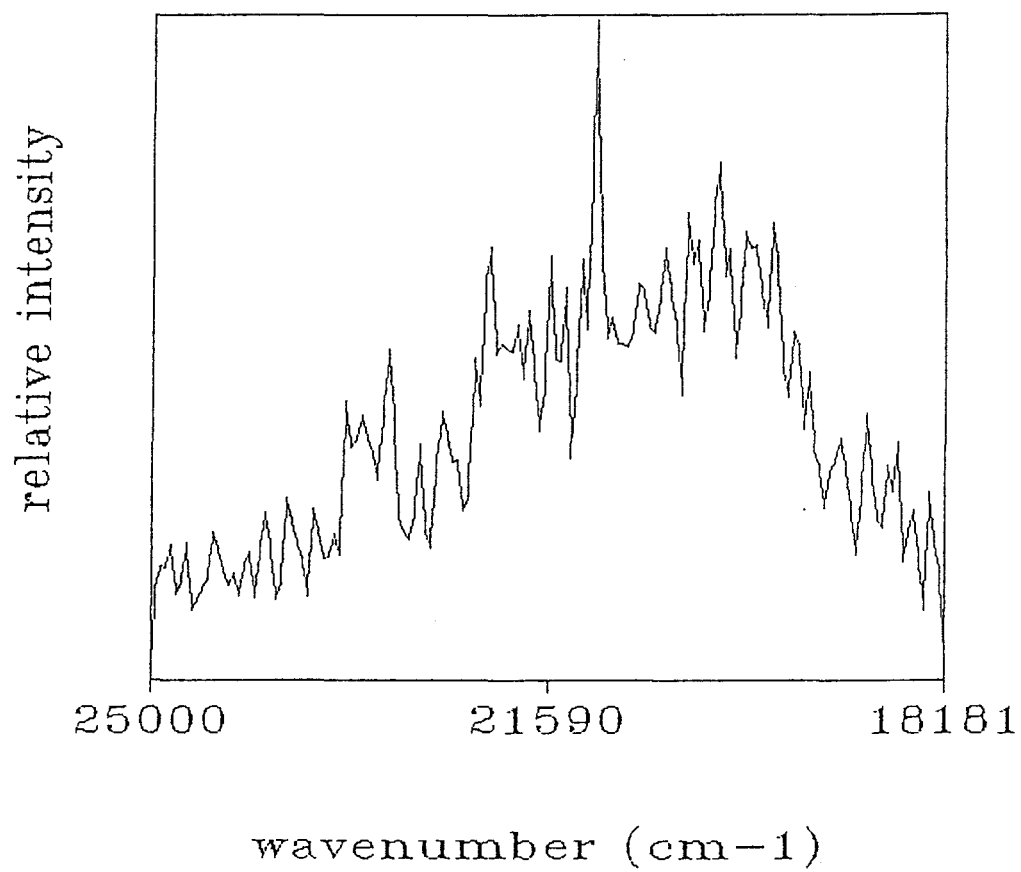
resolved spectra beyond experimental uncertainty were observed. However, the functionality of change with respect to annealing temperature appeared to be unchanged. These variations in the functional dependencies were due to variations in deposition nozzle position and heating rates. However, the differences in the experimental set-up and results were only of slight consequence with regard to the annealing dependent trends in the time resolved spectra outlined in this section.

B. *RADIATIVE DECAY MEASUREMENTS OF NEAT BENZOPHENONE AND BENZOPHENONE-d_{10}.*

Radiative decay measurements of BZP and BZP-d_{10} were recorded at 18 K for as-deposited and cyclic-annealed, vapor-quenched films. Marked changes in the radiative decay curves were observed with cyclic-annealing temperature.

Figure 35 illustrates the radiative decay curves of BZP for the as-deposited sample (bottom) and samples which were annealed in the range 18 to 40 K (middle) and 18 to 180 K (top).

Figure 35 enables comparison of the BZP decay curves as a function of annealing temperature. The decay curve which results from annealing in the range 18 to 180 K (top) decays more slowly in the time range 0 to 5 ms than either the as-deposited (bottom) or the 40 K (middle) annealed sample decay

Figure 35. Phosphorescence decay curves plotted versus time (in sec) for vapor-quenched BZP excited by the pulsed nitrogen laser. The decay measurements are from as-deposited BZP (bottom) and BZP subsequent to annealing in the range 18 to 40 K (middle) and 18 to 180 K (top). The decays were recorded at 23,697 cm^{-1} with 180 cm^{-1} slits and a .05 sec time window. The decays were recorded at 18 K.

relative intensity

time

0

.023

.047
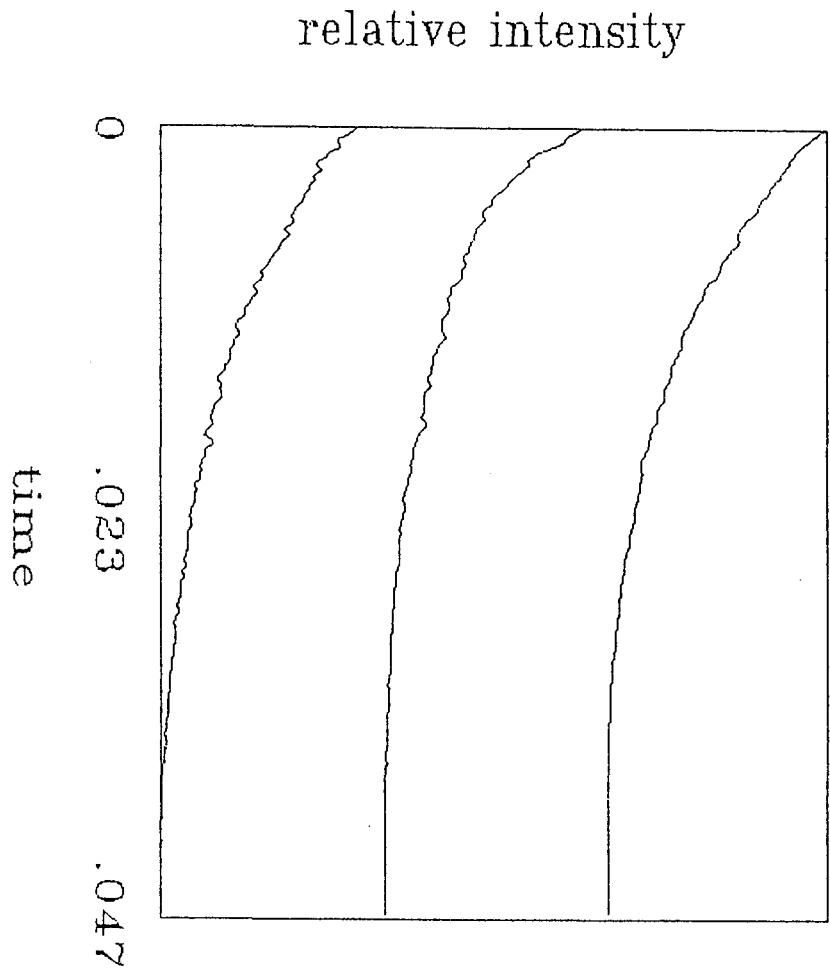
curves.   The radiative decay curve which resulted from
annealing in the range 18 to 40 K (middle) has the most rapid
initial decay rate in the range 0 to 5 ms.   The as-deposited
(bottom) sample decay curve has a longer tail in the time
range 20 to 25 ms than either of the other two decay curves
of figure 35.

Figure 36 illustrates plots of the natural logarithm of
the intensity versus time of the BZP decay curves in figure
35.   All three of these plots display curvature in the time
range up to 23 ms.   In other words, none of the decay curves
of figure 35 is well represented by exponential radiative
relaxation kinetics which are governed by a single lifetime.

Modeling of the radiative decay curves with regard to
excited state processes will help extract useful information
concerning microscopic molecular environments and how they
change along the crystallization path.   Modeling of the
radiative decay curves is described in Chapter IV.

C. *LOW TEMPERATURE EMISSION SPECTRA OF DISORDERED NAPHTHALENE / BENZOPHENONE MIXTURES*

The cw emission spectra of mixtures of NAP/BZP were
investigated   with   a   view   toward   understanding   the
crystallization path of neat BZP.   The effects of a structural
impurity namely NAP on molecular packing was also examined.

The spectra of three different mole fractions (1:2, 1:6

Figure 36. Natural logarithm of the intensity versus time (in sec.) of BZP radiative decays of figure 26. The curves correspond to the as-deposited (bottom) BZP sample and samples annealed in the range 18 to 40 K (middle) and 18 to 180 K (top).

log(intensity)

0   .023   .047

time
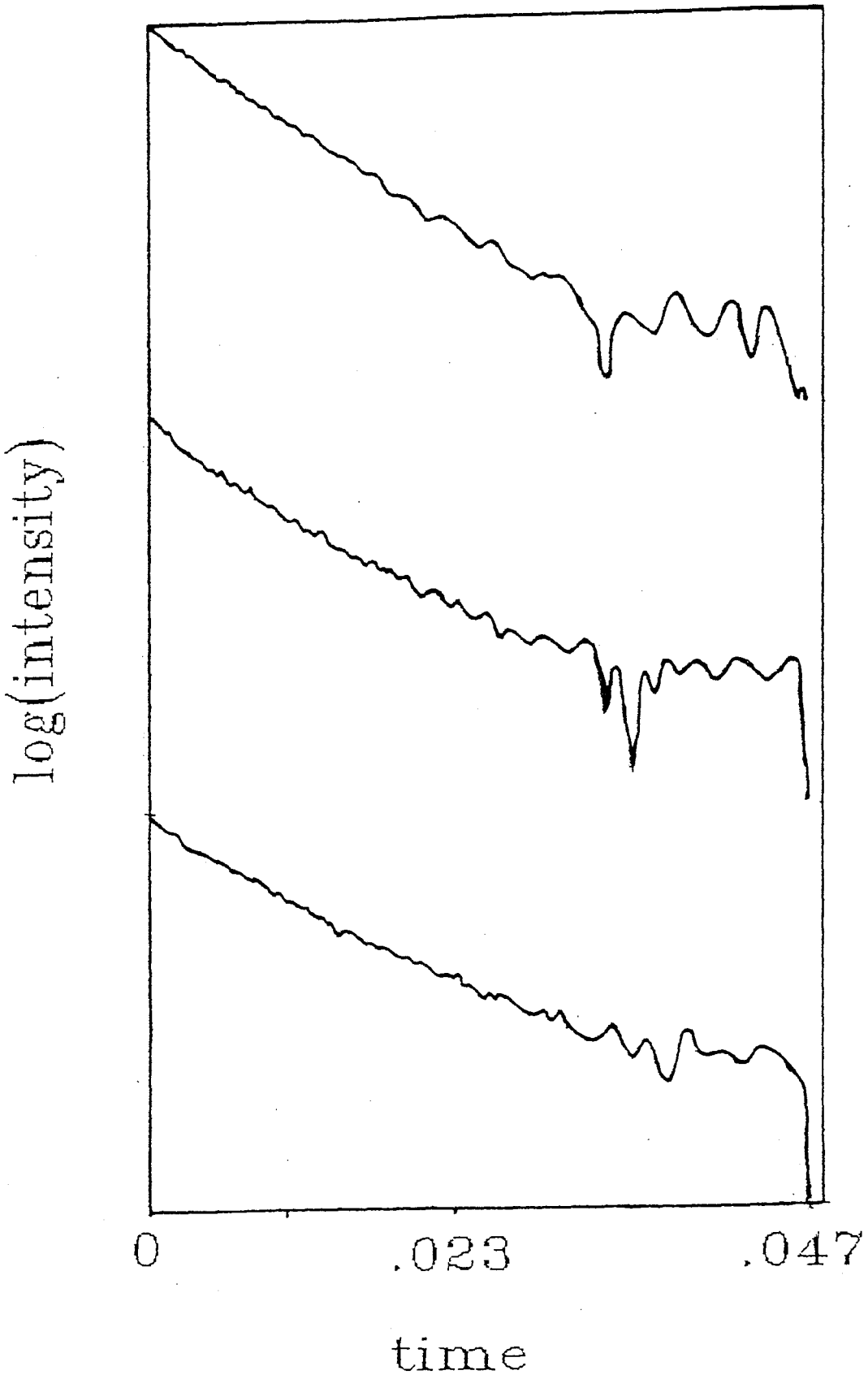
and 1:16) of NAP in BZP recorded at 18 K were observed to depend on the mole ratio of NAP and cyclic-annealing temperature. All three mixtures exhibited very different as-deposited and annealed sample spectra. These results demonstrate the effects of a structural impurity on the packing and exciton transfer properties of vapor-quenched BZP as it crystallizes.

Figure 37 illustrates the as-deposited sample spectrum of the 1:2 mole ratio NAP/BZP mixture. It contains predominately NAP phosphorescence originating at 20,797 cm^{-1}. The NAP phosphorescence spectrum is characterized by a vibrational progression with bands located 450 and 1460 cm^{-1} lower in energy than the origin. These vibrational transitions have been assigned to a C-H bending mode. In addition to NAP phosphorescence, the 0-2 band of BZP is visible just above the background at 22,060 cm^{-1}.

Figure 38 illustrates the as-deposited 1:2 mole ratio NAP/BZP sample spectrum (lower) and the spectrum recorded after annealing in the range 18 to 140 K (upper spectrum). The spectrum resulting from the 140 K anneal is similar to the as-deposited sample spectrum. The difference is that no electronic-vibrational structure is observed at energies greater than the NAP 0-0 phosphorescence origin. Figure 39 illustrates the spectrum which resulted from annealing in the range 18 to 180 K. It is somewhat different from the previous two in that the observed NAP origin is shifted 109 cm^{-1} lower

Figure 37.   Xenon arc lamp induced phosphorescence spectrum of the as-deposited, 1:2 mole ratio mixture of NAP/BZP.   The spectrum was recorded with a resolution of ±28 cm^{-1} at a sample temperature of 18 K.
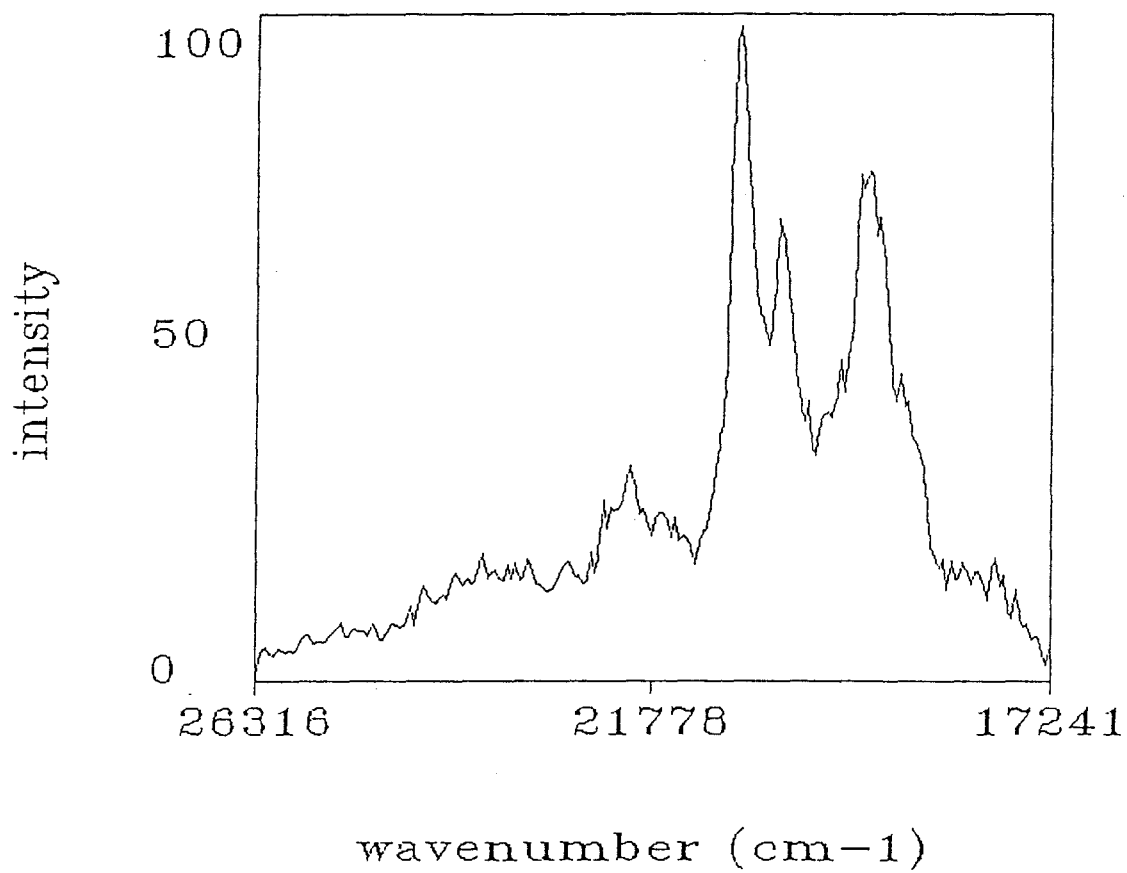
Figure 38. Xenon arc lamp induced phosphorescence spectra of the as-deposited (bottom) and 140 K annealed (top) 1:2 mole ratio mixture of NAP/BZP. The spectra were recorded with a resolution of ± 28 cm^{-1} at a sample temperature of 18 K.

relative intensity

26315   21778   17241

wavenumber (cm−1)
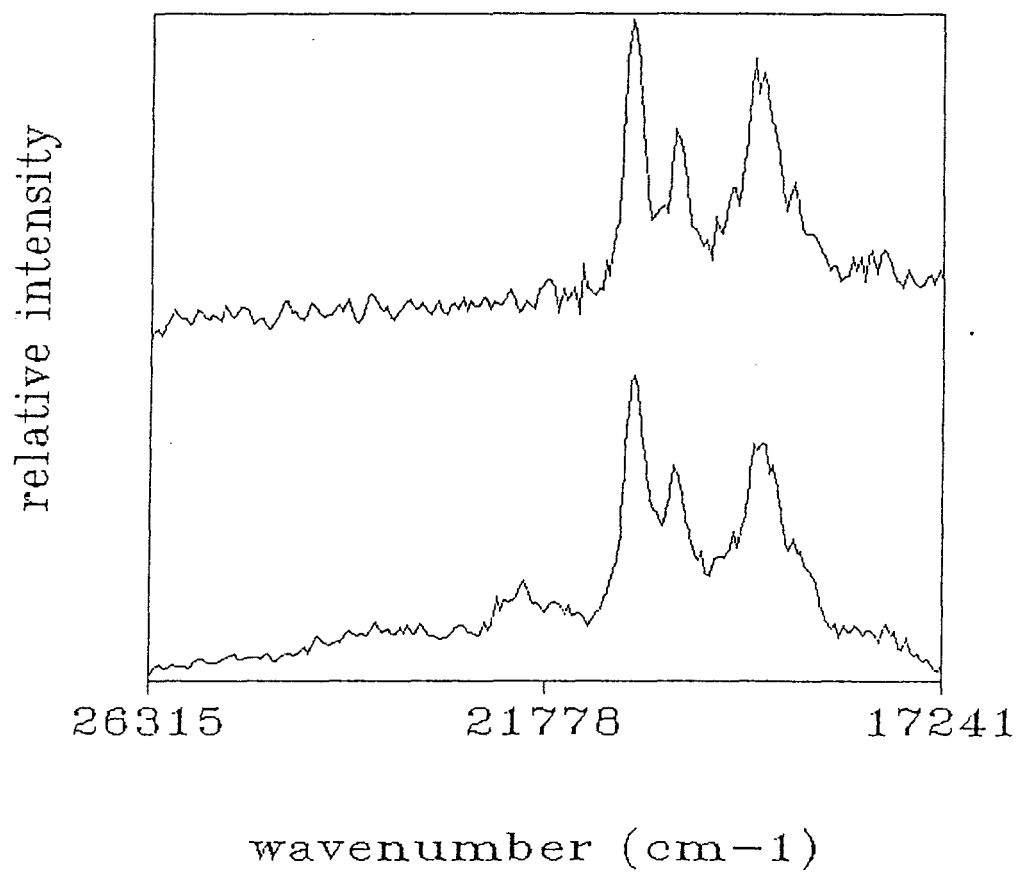
Figure 39.   Xenon arc lamp induced phosphorescence spectrum of the 1:2 mole ratio mixture of NAP/BZP annealed in the range 18 to 180 K.   The spectra was recorded with a resolution of ± 28 cm^{-1} at a sample temperature of 18 K.
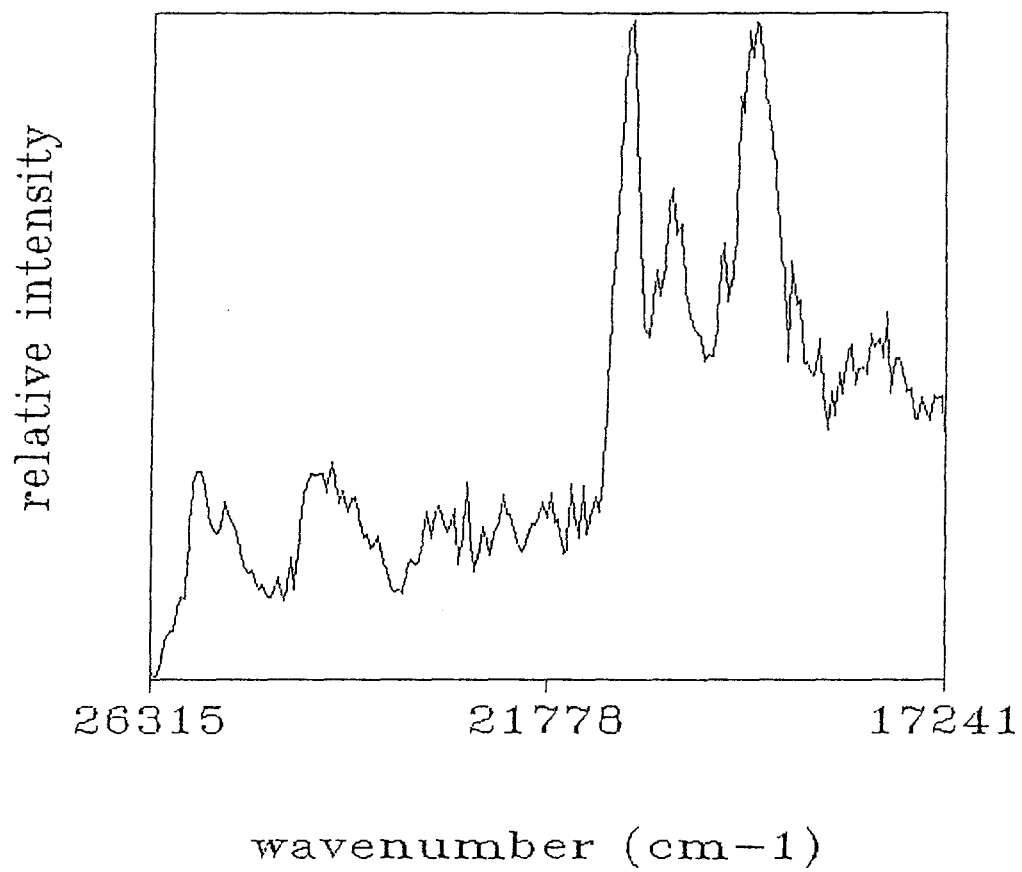
in energy to 20,870 cm^{-1}. The 180 K annealed sample spectrum also has bands in the 24,000 to 26,000 cm^{-1} region. The bands are observed at 25,727, 25,426 and 24,195 cm^{-1}. The 25,727 and 25,426 cm^{-1} bands result from NAP fluorescence, while the 24,195 cm^{-1} band appears to be a combination of NAP fluorescence and BZP 0-0 vibrational band phosphorescence.

Figure 40 illustrates the result of excitation of the as-deposited 1:6 mole ratio NAP/BZP mixture. No NAP phosphorescence features are observed for this 18 K spectrum. The spectrum consists of NAP fluorescence originating at 26,846 cm^{-1} overlapping BZP phosphorescence originating at 23,969 cm^{-1}. The 0-0, 0-1 and 0-2 bands of BZP are very broad and poorly resolved with the vibrational splitting between the 0-0 and 0-1 bands being 1693 cm^{-1}.

Figure 41 illustrates the time resolved spectrum of the as-deposited 1:6 mole ratio NAP/BZP sample recorded after a 40 ms delay with respect to the nitrogen laser pulse. This figure demonstrates that even at long delay times no NAP phosphorescence or fluorescence is observed.

Figure 42 illustrates the spectra recorded for the 1:6 mole ratio NAP/BZP mixture upon annealing in the ranges 18 to 80 (bottom) and 18 to 120 K (top). The BZP portion of spectrum effected upon annealing in the 18 to 80 K (bottom) range is shifted 256 cm^{-1} higher in energy to 24,225 cm^{-1} and the carbonyl bands are broader than the as-deposited sample spectrum. The energy difference between the 0-0 and 0-1 bands

Figure 40. Xenon arc lamp induced phosphorescence spectrum of the as-deposited, 1:6 mole ratio mixture of NAP/BZP. The spectrum was recorded with a resolution of ±28 cm^{-1} at a sample temperature of 18 K.
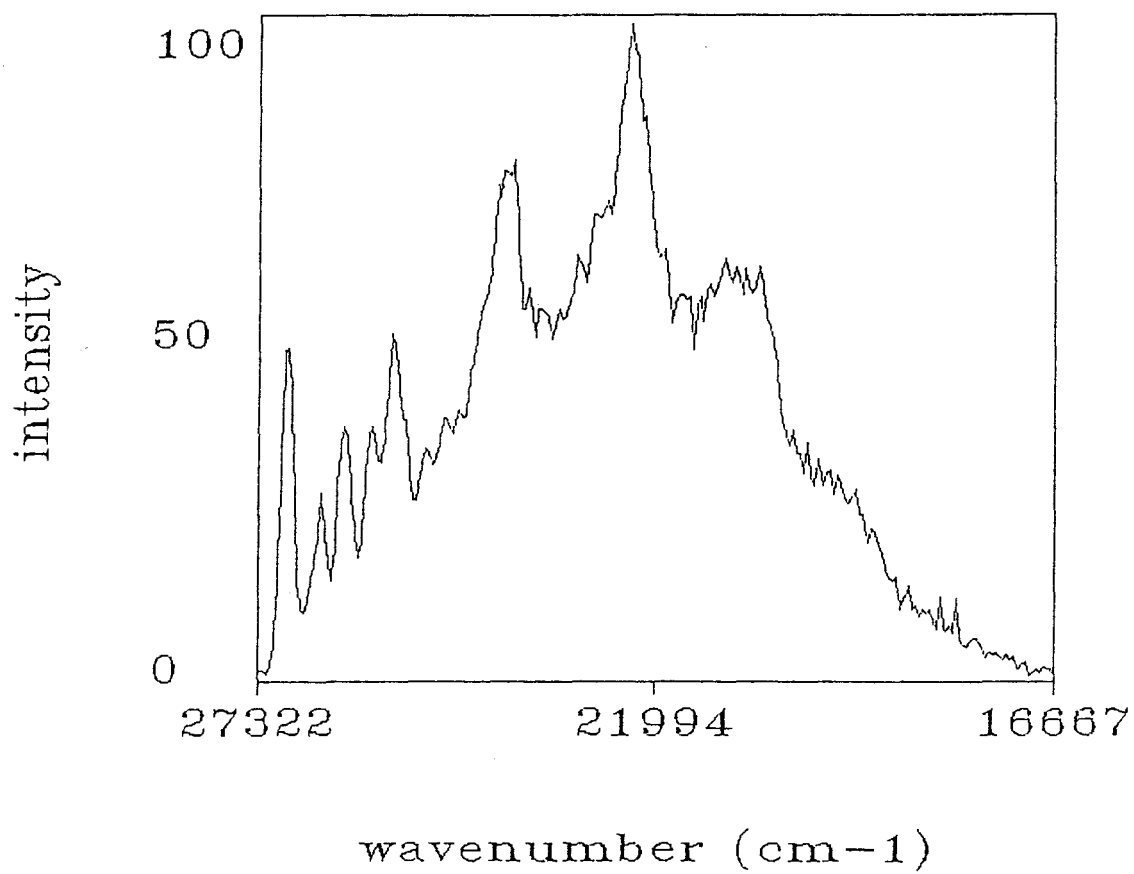
Figure 41.   Pulsed nitrogen laser induced phosphorescence spectrum of the as-deposited, 1:6 mole ratio mixture of NAP/BZP recorded with a 40 ms delay time.   The spectrum was recorded with a resolution of ±28 cm^{-1} at a sample temperature of 18 K.
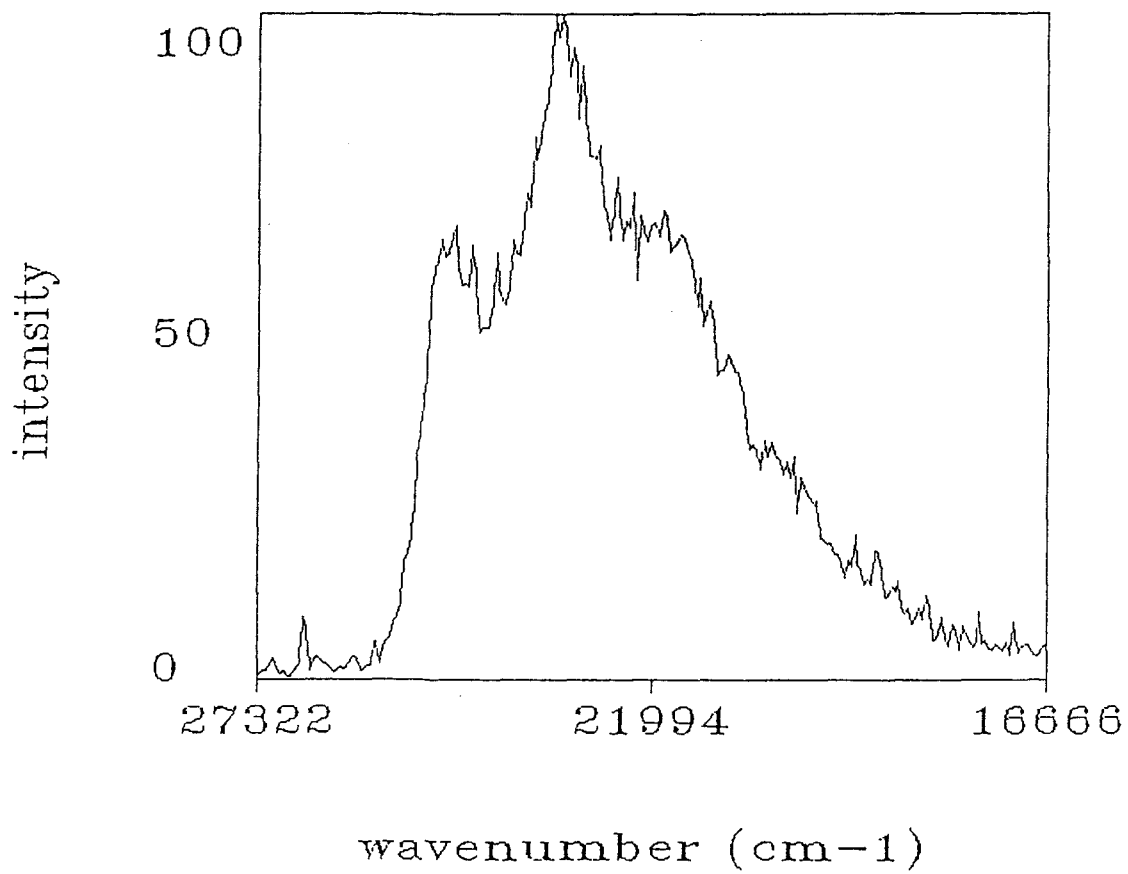
Figure 42.   Xenon arc lamp induced phosphorescence spectrum of the 1:6 mole ratio mixture of NAP/BZP annealed in the range 20 to 80 K (top) and 20 to 120 K (bottom).   The spectra were recorded with a resolution of ±28 cm^{-1} at a sample temperature of 18 K.
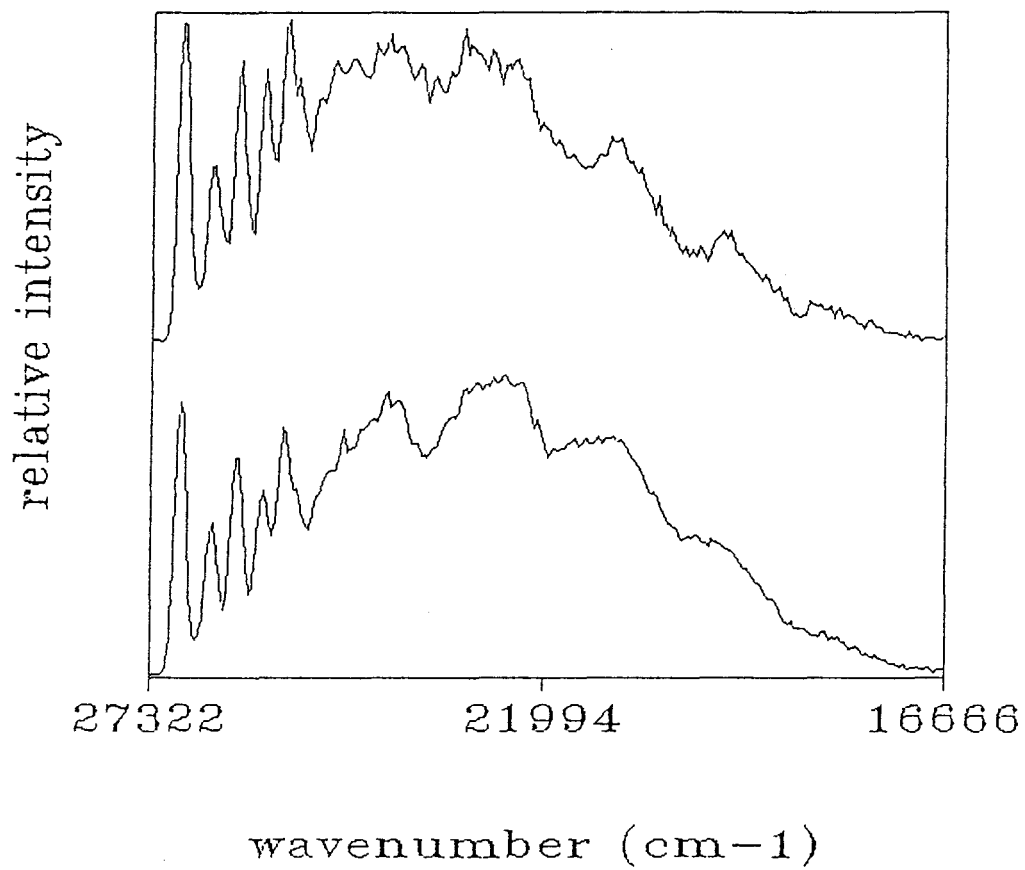
Figure 43. Xenon arc lamp induced phosphorescence spectrum of the 1:6 mole ratio mixture of NAP/BZP annealed in the range 18 to 170 K. The spectrum was recorded with a resolution of ± 28 cm^{-1} at a sample temperature of 18 K.
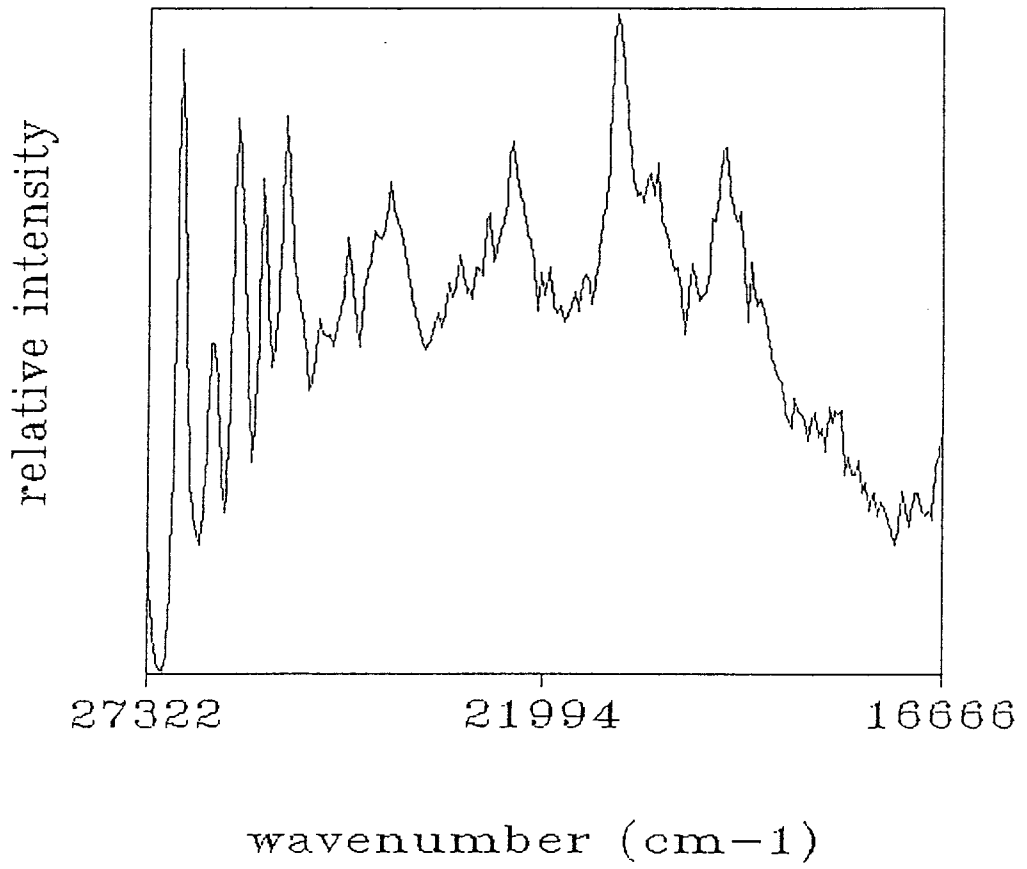
is 1505 cm^{-1}. The spectrum resulting from annealing in the range 18 to 120 K (top) exhibits very broad BZP vibrational bands which are poorly resolved. NAP phosphorescence is also observed in this spectrum origination at 21001 cm^{-1}.

Figure 43 illustrates the spectrum recorded for the 1:6 mole ratio NAP/BZP mixture after annealing in the range 18 to 170 K. This spectrum is different from the as-deposited and previously annealed sample spectra in two respects. First, the NAP phosphorescence is the most intense feature in the spectrum and second, the BZP carbonyl vibrational bands are much narrower than any of the previously annealed sample spectra. The 170 K annealed sample spectrum BZP vibrational bands are not as narrow as in the as-deposited sample spectrum.

Comparing figures 41 through 43, the NAP phosphorescence intensity is seen to increase with annealing in the range 80 to 170 K. Prior to 80 K, no NAP phosphorescence is observed. No shifts in E_{max} occur for the NAP phosphorescence origin. The BZP phosphorescence origin shifts from 23,969 to 23,111 cm^{-1} upon annealing in the 18 to 170 K range. Also the BZP carbonyl vibrational bands become broader with annealing in the range 18 to 150 K and narrower with annealing in the 160 to 170 K range. In all of the spectra recorded for the 1:6 mole ratio mixture NAP fluorescence was observed with considerable intensity.

Figure 44 illustrates the spectrum of the as-deposited

Figure 44. Xenon arc lamp induced phosphorescence spectrum of the as-deposited, 1:16 mole fraction mixture of NAP/BZP. The spectrum was recorded with a resolution of ± 28 cm^{-1} at a sample temperature of 18 K.
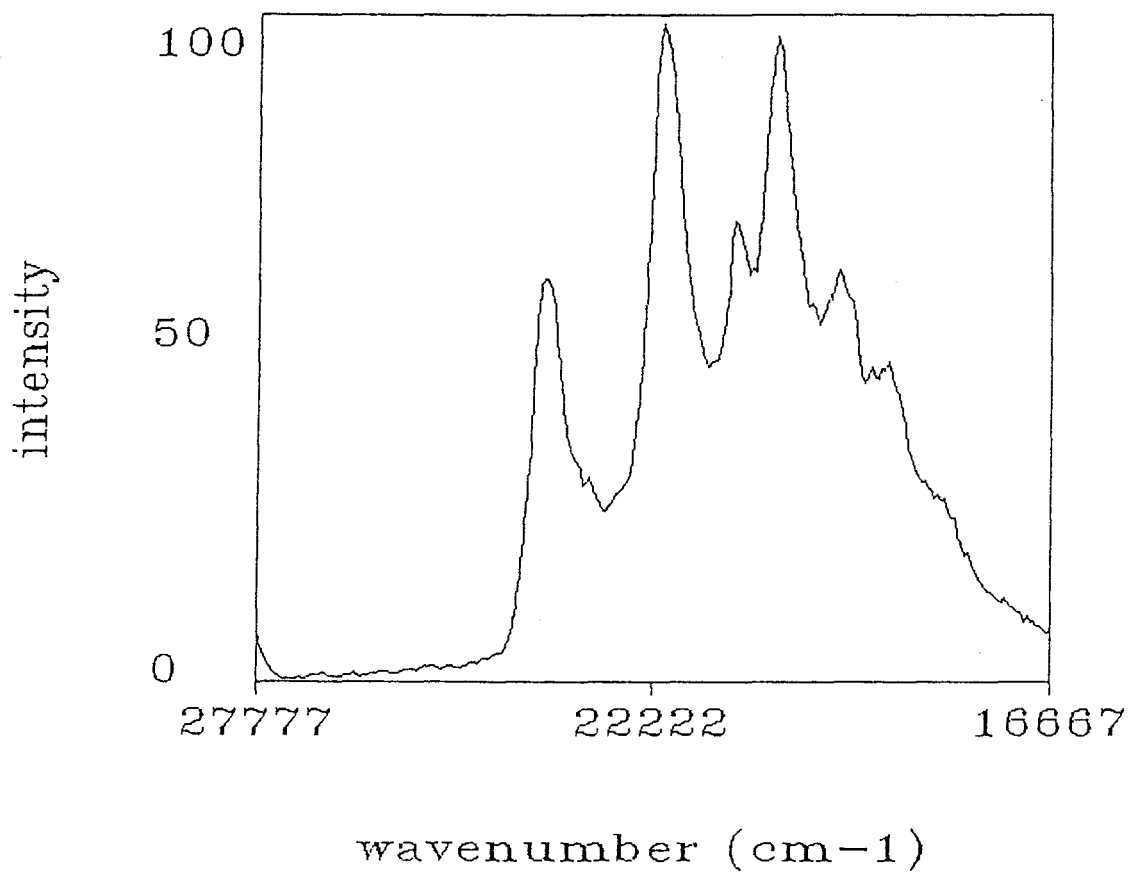
1:16 mole ratio NAP/BZP mixture. The spectral features are reminiscent of the neat, vapor-deposited spectrum of BZP with only a small fraction of NAP phosphorescence present. The BZP 0-0 vibrational band emission origin is at 23,585 cm^{-1} and separated by 1678 cm^{-1} from the 0-2 vibrational band. The NAP phosphorescence origin is at 21,053 cm^{-1}.

Figure 45 illustrates for comparison the as-deposited spectrum of the 1:16 mole ratio NAP/BZP mixture (bottom) and the spectrum which results from annealing in the range 18 to 180 K (top). The annealed sample spectrum of figure 45 (top) contains primarily NAP phosphorescence, but NAP fluorescence is also observed originating at 26,822 cm^{-1}. No BZP phosphorescence is observed. The 180 K annealed sample spectrum is not similar to the as-deposited sample spectrum except for the presence of NAP phosphorescence.

Three spectral changes occur during the course of annealing the 1:16 mole ratio NAP/BZP mixture in the range 18 to 180 K. First, the BZP origin shifts 224 cm^{-1} higher in energy to 23,809 cm^{-1}. Second, the observed NAP origin shifts 74 cm^{-1} lower in energy to 20,979 cm^{-1}. Figure 46 illustrates the decrease of E_{max} for the NAP 0-0 vibrational band in the annealing range 70 to 180 K. Finally, the intensity of NAP phosphorescence relative to BZP phosphorescence was observed to change with cyclic-annealing. This change was indicated by the ratio of the NAP 0-0 band intensity to the sum of the BZP 0-1 band and the NAP 0-0 band intensities

Figure 45. Xenon arc lamp induced phosphorescence spectrum of the 1:16 mole fraction mixture of NAP/BZP. The bottom spectrum is from the as-deposited sample and the top is from the sample subsequent to annealing in the range 18 to 180 K. The spectra were recorded with a resolution of ± 28 cm^{-1} at a sample temperature of 18 K.
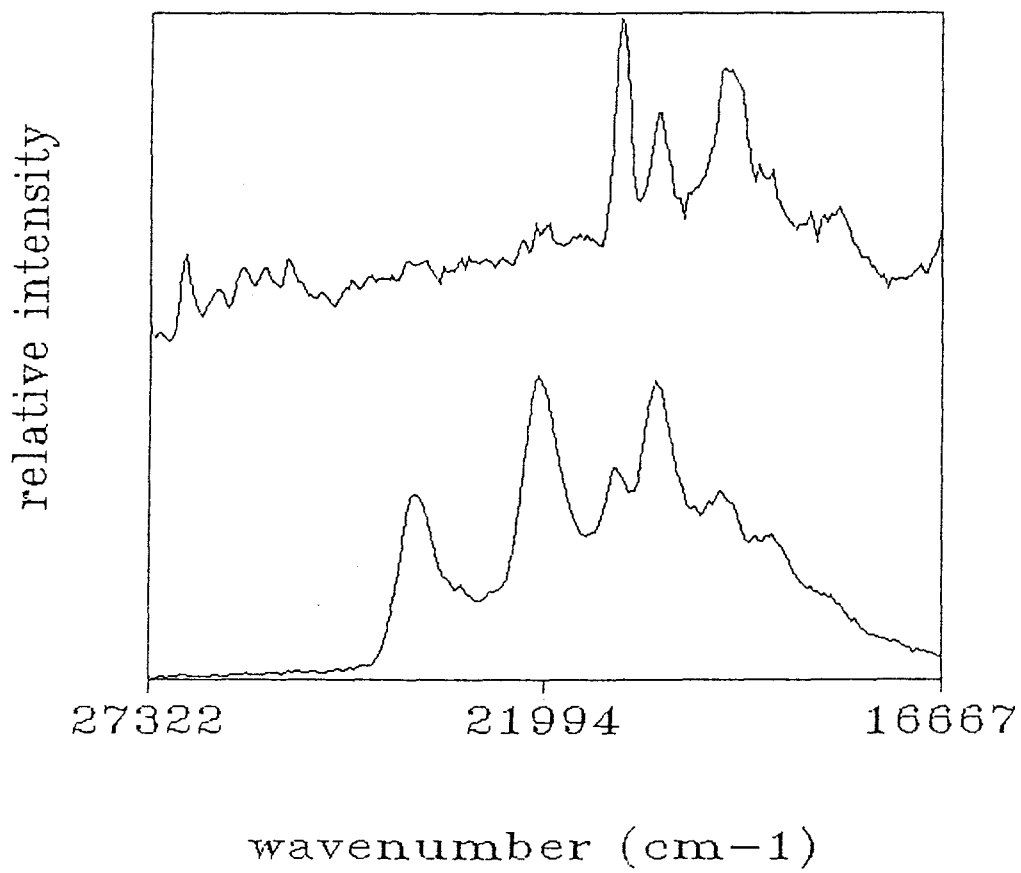
Figure 46. E_{max} (in cm^{-1}) of the NAP 0-0 phosphorescence band plotted versus annealing temperature (in K) from the spectra of the 1:16 mole ratio mixture of NAP/BZP. Cyclic-annealing took place in 10 K increments in the range 20 to 180 K with a 2 K increment anneal in the range 18 to 20 K. The error bars are ±28 cm^{-1}. This is the uncertainty associated with the resolution of the monochromator.
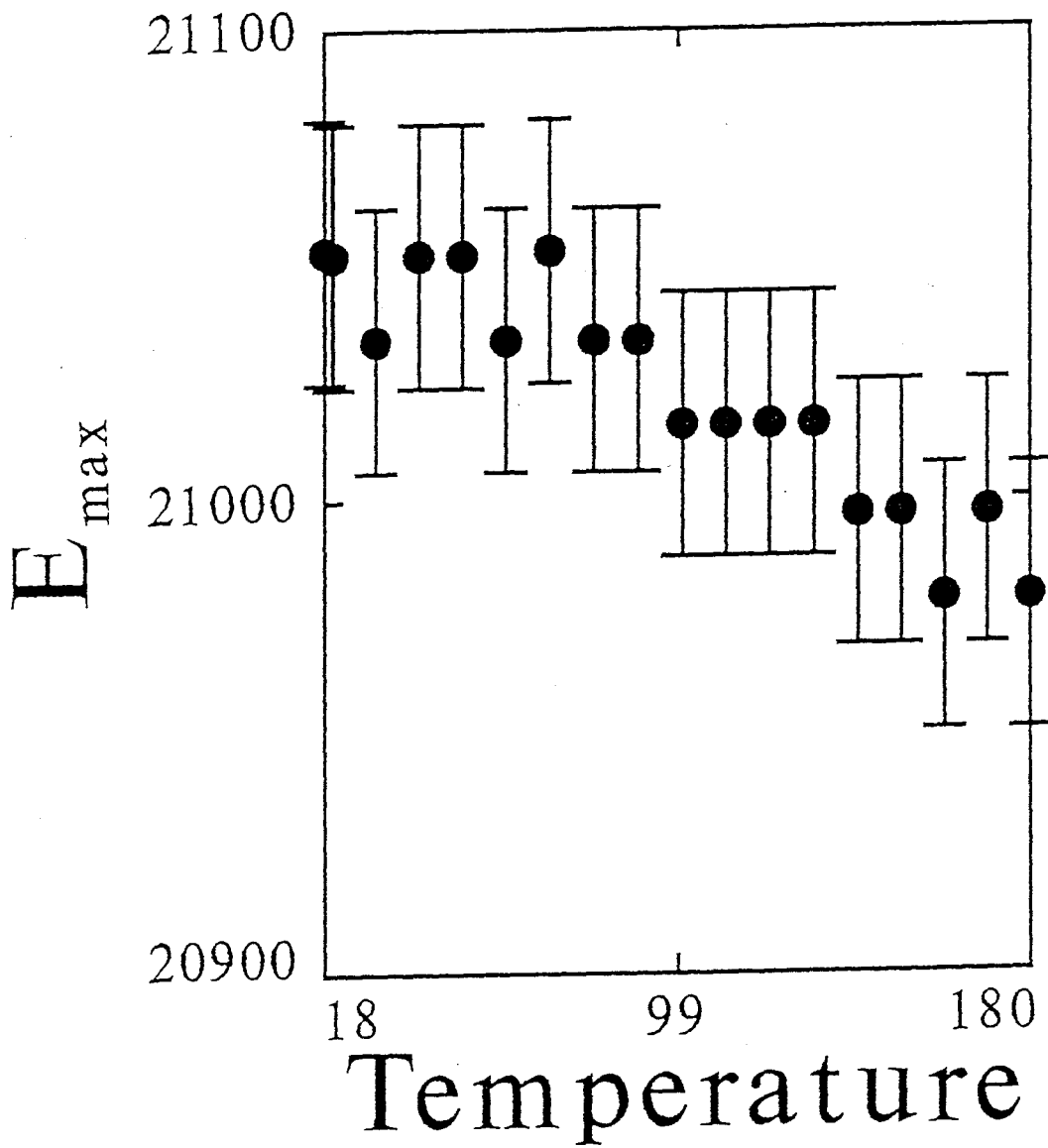
Figure 47. $I_{NAP}/(I_{NAP}+I_{BZP})$ from the spectrum of the 1:16 mole ratio mixture of NAP/BZP plotted as a function of annealing temperature (in K). The error bars are on the order of the dot sizes. The are due to fluctuations in the noise level in the PMT resulting from changes in intensity variations.
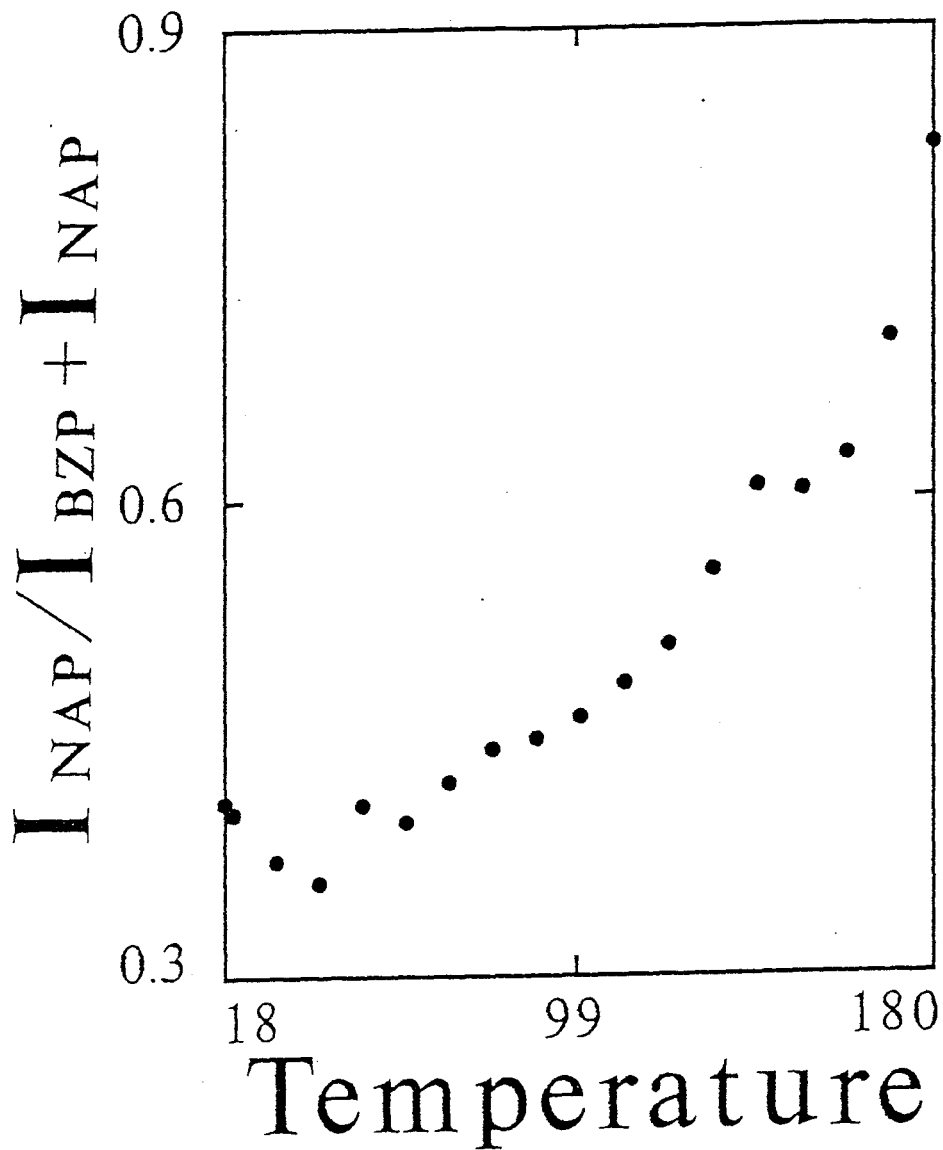
$(I_{NAP}/(I_{NAP}+I_{BZP}))$ plotted as a function of annealing temperature (figure 47). $I_{NAP}/(I_{NAP}+I_{BZP})$ decreases with annealing in the range 18 to 40 K and increases in a continuous manner with annealing in the range 40 to 180 K. This plot exemplifies the results of cyclic-annealing on the change in the BZP phosphorescence intensity relative to the NAP phosphorescence intensity of the 1:16 mole ratio NAP/BZP mixture.

The NAP fluorescence emission observed in all the mixed system sample spectra was characterized from neat vapor-quenched NAP. Figure 48 illustrates the spectrum which resulted from excitation of neat, vapor-quenched NAP. The observed fluorescence origin is 26,846 cm^{-1}. The spectrum is characterized by a C-H bending mode vibrational progression with bands located 419, 736, 1092 and 1452 cm^{-1} lower in energy than the NAP fluorescence emission origin.

The results of the mixed sample annealing experiments are from selected experiments. As with all the samples of the project certain variations occurred for repeated experiments, particularly with respect to nozzle position and heating rates. However, these variations had little effect on the cyclic-annealing dependent trends observed for the data of this project. For example, the magnitudes of change of the BZP intensity relative to that of NAP were beyond experimental uncertainty for different experiments. However, the functional dependence of the relative intensity changes with annealing temperature appeared to be unaffected. The

differences do signify the effects of slightly different experimental conditions especially with regard to deposition conditions and the time frame of annealing. The similarities, on the other hand, demonstrate that actual trends exist as evidenced by the parameters used to understand the crystallization path.

Figure 48. The nitrogen laser induced fluorescence spectrum of as-deposited, neat NAP. Acquisition was delayed by 400 ns with respect to the laser pulse. The spectrum was recorded with a resolution of ± 28 cm^{-1} at a sample temperature of 18 K.
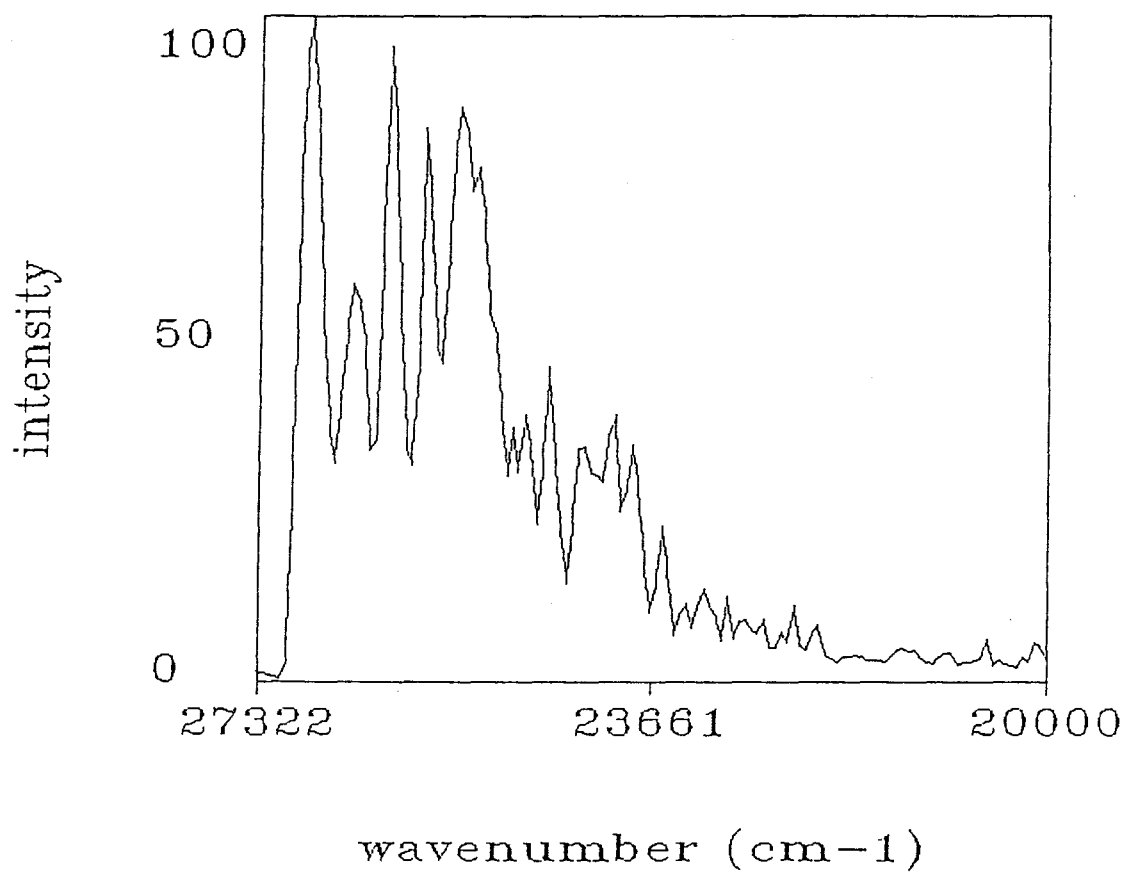
CHAPTER IV

MODELS OF THE RADIATIVE DECAY KINETICS OF

BENZOPHENONE AND BENZOPHENONE-d_{10}

A number of theoretical investigations concerned with excitation energy transport and radiative relaxation in disordered molecular systems including BZP have been carried out.[6-9,10,11,17,19,20-24,30,34,35,40,42,53-55,57,58] Two different but complementary models concerning the radiative decay kinetics of triplet state BZP were applied in this project using some of these ideas. The first model (model I) assumes nothing about electronic excitation energy transfer processes. Model I only assumes a Gaussian distribution of radiative relaxation rates to be operative in the sample. The second model (model II) makes certain assumptions concerning electronic excitation energy transfer. The purpose of these models is to get at the molecular information contained in the radiative decay curves and how it changes with annealing. This information and its functional dependence on annealing temperature provides insight into the microscopic transformations involved in the crystallization of vapor-quenched BZP.

A. MODEL I.

1. Presentation of Model I.

Vapor-quenched BZP is one example of a disordered solid. In modeling its radiative decay kinetics it is reasonable to assume that a distribution of natural decay rates dependent on the emitting site energies is operative. Following Richert, the distribution of emitting site energies is assumed to be Gaussian.[43] This distribution results from a Gaussian distribution of molecular shapes and intermolecular orientations in vapor-quenched BZP.[4]

The radiative relaxation of BZP emitting sites which possess the same energy are assumed to follow a single exponential rate law characterized by a single average rate, k_0. Radiative relaxation from a Gaussian distribution of emitting site energies results in a Gaussian distribution of first order decay rates. The weighting coefficient of the continuous distribution of first order rate equations is simply the Gaussian random variable integrated over the possible values of the decay rate. The time dependence of the excited molecular states E(t) subject to a Gaussian distribution of natural decay rates is given by:

$$E(t) = 1/(\sqrt{(2\pi)})\sigma \int_{-\infty}^{\infty} \exp[(-(k-k_0)^2/2\sigma^2)-kt] \; dk \qquad (1)$$

where, k_0 is the average radiative relaxation rate and σ is the variance of the radiative relaxation rates. The integration is carried out over all space since unphysical negative values of the rate constants make a negliable contribution to the Gaussian distribution. Equation (1) can be simplified by completing the square of the argument and adding and subtracting the terms $2k_0\sigma^2t + \sigma^4t^2$, i.e.

$$\left[\frac{(k-k_0)^2}{2\sigma^2} + kt \right]$$

$$= \left[\frac{(k + (\sigma^2t - k_0))^2}{2\sigma^2} + k_0t - \frac{\sigma^2t^2}{2} \right] \qquad (2).$$

combining equation (2) with Equation (1), E(t) becomes

$$E(t) = 1/(\sqrt{(2\pi)})\sigma \; \exp[(\sigma^2t^2/2)-k_0t] \; * \; \phi(t|k_0,\sigma) \qquad (3)$$

where $\qquad \phi(t|k_0,\sigma) = \int_{-\infty}^{\infty} \exp[-(k+\sigma^2t-k_0)^2/2\sigma^2] \; dk \qquad (4).$

$\phi(t|k_0,\sigma)$ must be determined numerical methods. The restriction that $k_0/\sigma^2 \gg t$ is used to ensure the assumption of the Gaussian distribution is justified. Equations (3) and

(4) are the final result of model I. They are vital for extracting annealing dependent information contained in radiative decay curves which is correlated with microscopic processes.

Equations (3) and (4) were used to simulate radiative decay curves of vapor-quenched BZP and BZP-d_{10}. The two adjustable parameters σ and k_0 indicate the variance and average of the distribution over the natural decay rates for vapor-quenched BZP. Thus k_0 and σ and changes thereof with annealing temperature are used to interpret how the distribution changes as BZP and BZP-d_{10} crystallize.

2. *Application of Model I to Experimental Data.*

Radiative decay curves of BZP and BZP-d_{10} recorded in this study were simulated using equations (3) and (4) of model I in order to extract annealing dependent information on microscopic interactions. k_0 and σ were observed to change with cyclic-annealing. Nonlinear regression of the BZP and BZP-d_{10} radiative decay curves using equations (3) and (4) yielded values of k_0 and σ as a function of cyclic annealing.

Figure 49 illustrates changes in k_0 for BZP cyclic-annealed in the range 18 to 180 K. k_0 increases sharply in the 18 and 40 K annealing range and then decreases in the annealing range 40 to 180 K. k_0 ranges between 204 and 300

Figure 49. k_0 (in sec^{-1}) of model I for BZP versus annealing temperature (in K) in 10 K increments in the range 20 to 180 K. A 2 K anneal took place in the range 18 to 20 K. The uncertainty in k_0 is roughly ± 10 sec^{-1}.
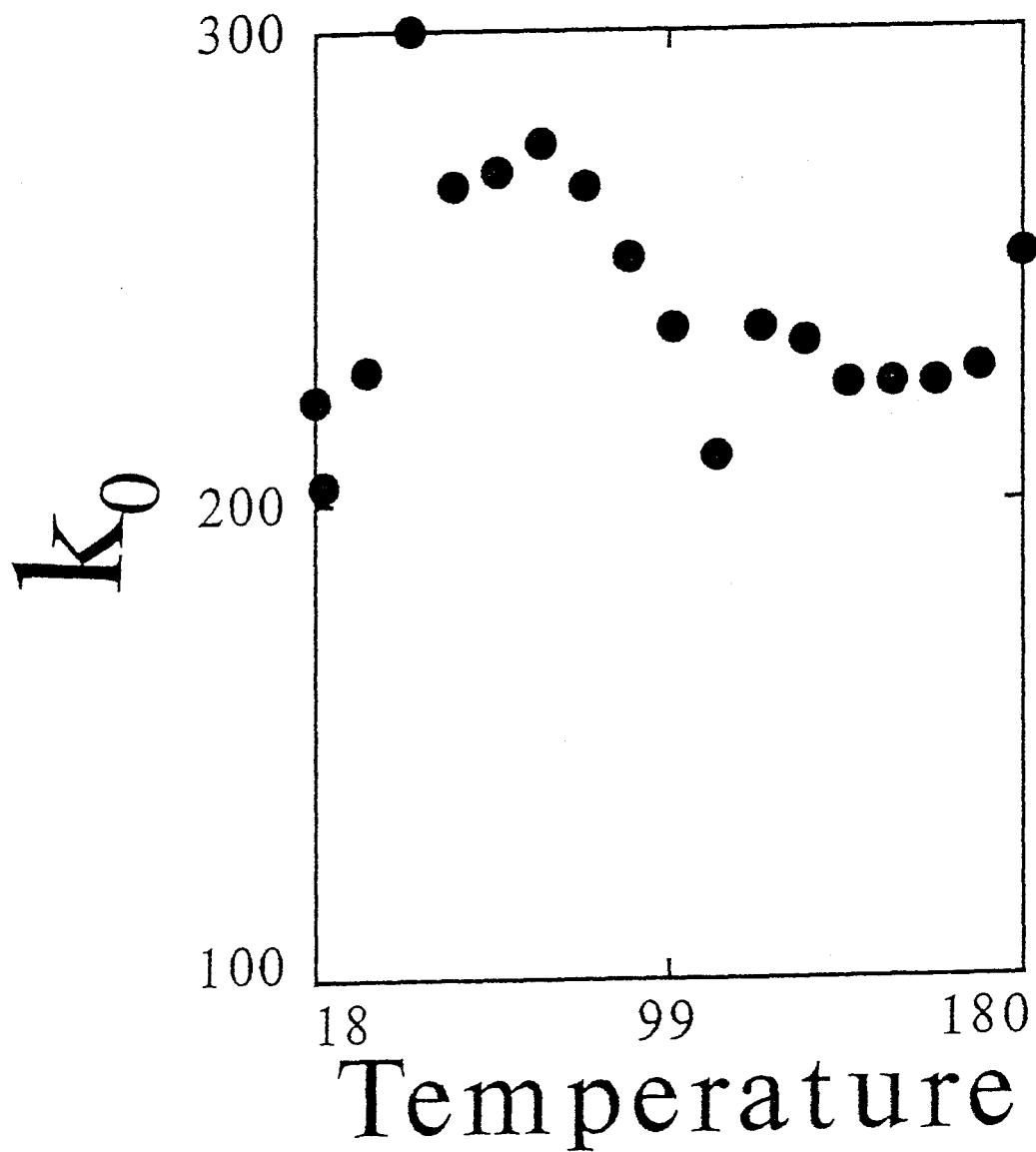
Figure 50. k_0 (in sec^{-1}) of model I for BZP-d_{10} versus annealing temperature (in K) in 10 K increments. A 2 K anneal took place in the range 18 to 20 K. The uncertainty in k_0 is roughly ±10 sec^{-1}.
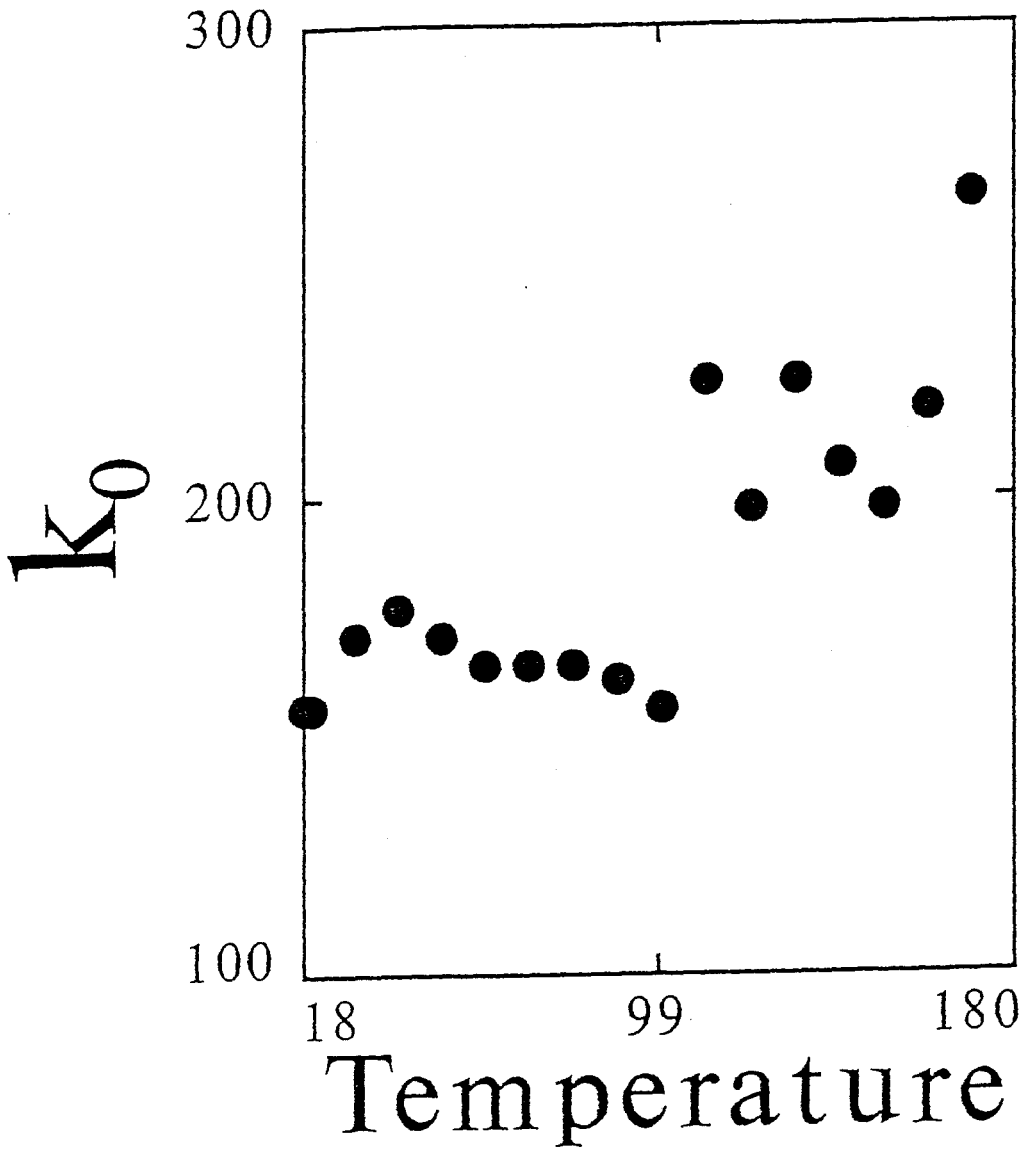
sec^{-1} for the 20 and 40 K annealing temperatures. Figure 50 exemplifies the behavior of k_0 for BZP-d_{10} annealed in the range 18 to 170 K. k_0 increases with annealing temperature in the range 18 to 40 K and then gradually decreases with annealing between 40 to 100 K. k_0 increases again in the annealing temperature range 100 to 180 K. k_0 for BZP-d_{10} ranges between 156 and 264 sec^{-1} for the as-deposited and 170 K annealed samples.

Figures 49 and 50 together illustrate that both species exhibit similar behavior with annealing temperature. However, k_0 for BZP-d_{10} does not experience percentage changes as large as k_0 for BZP in the annealing range below 110 K. k_0 experiences larger fluctuations and larger percentage changes for BZP-d_{10} with annealing above 110 K as compared to BZP in the same range.

Figure 51 illustrates the changes in σ for BZP upon annealing in the range 18 to 180 K. σ of model I increases sharply with annealing in the 30 to 40 K range and decreases with the annealing temperature in the range 40 to 180 K. σ's maximum value is 71 sec^{-1} and minimum is 14 sec^{-1} at the annealing temperatures of 40 and 30 K.

Figure 52 illustrates a similar plot of σ for BZP-d_{10} upon annealing in the 18 to 170 K range. The value of σ for BZP-d_{10} decreases with annealing in the 18 to 30 K range and is constant at 11 sec^{-1} with annealing between 30 and 60 K. σ fluctuates with an increasing trend in the annealing

Figure 51. σ (in sec^{-1}) of model I for BZP versus annealing temperature (in K) in 10 K increments in the range 20 to 180 K. A 2 K anneal took place in the range 18 to 20 K. The uncertainty in k_0 is roughly ±1 sec^{-1}.
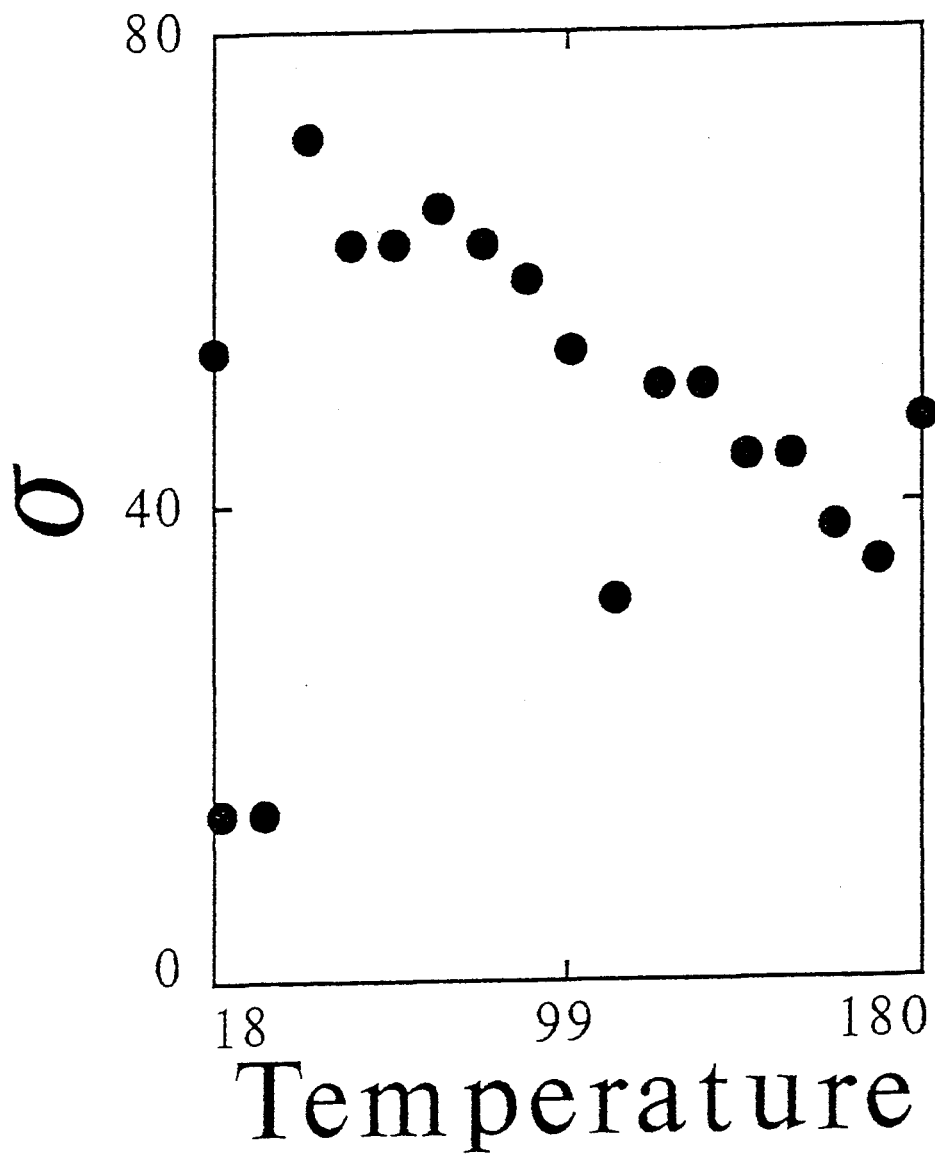
Figure 52. σ (in sec^{-1}) of model I for BZP-d$_{10}$ versus annealing temperature (in K) in 10 K increments in the range 20 to 18 K. A 2 K anneal took place in the range 18 to 20 K. The uncertainty in k_0 is roughly ±1 sec^{-1}.
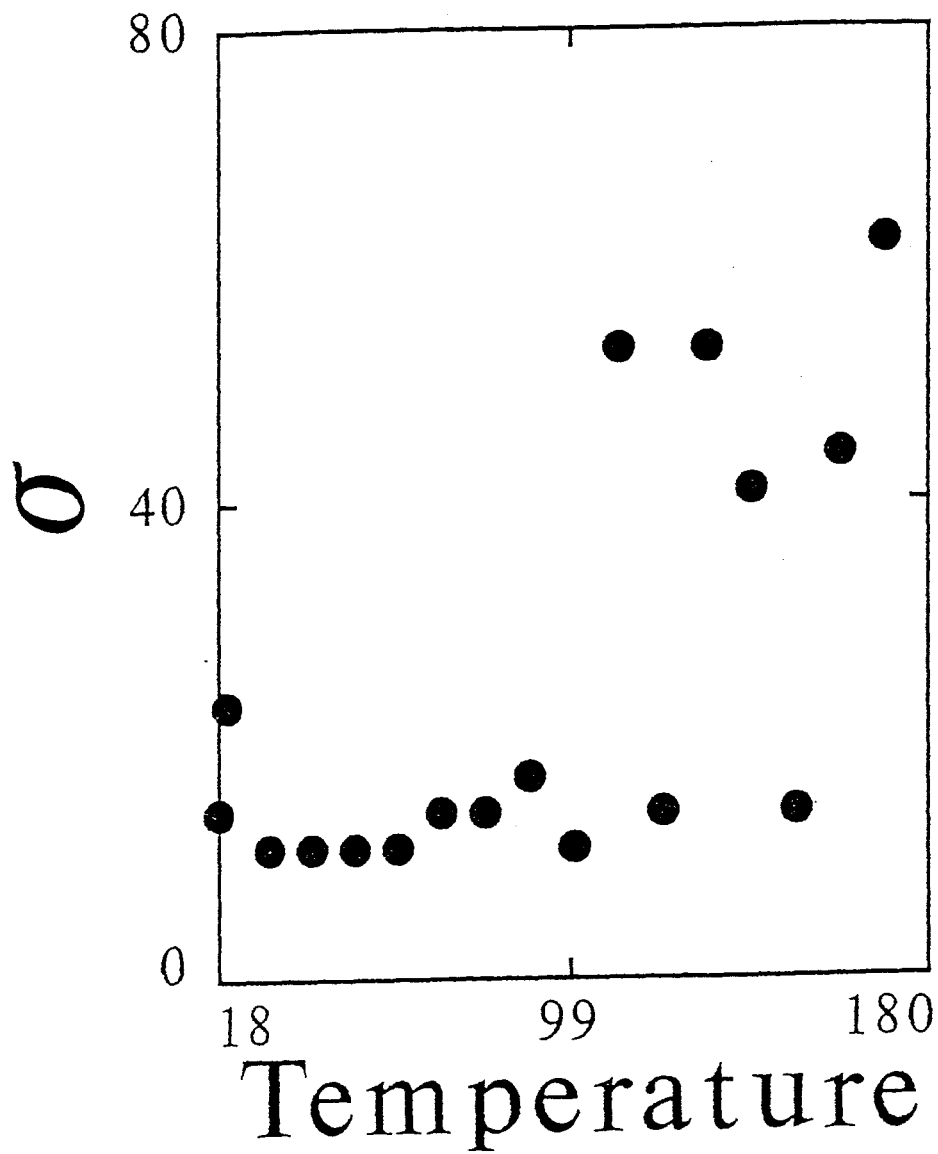
temperature range 60 to 180 K. The minimum value of σ for BZP-d_{10} is 11 sec^{-1} in the annealing range 30 to 60 K and itsmaximum is 65 sec^{-1} subsequent to annealing to 170 K.

Comparing figures 51 and 52, no striking similarities in σ between the two species are observed. The relative error between the two sets of sample parameters associate with fitting equation (3) to the decay curves was greater for the case of σ for BZP-d_{10}. This may be the reason for the large differences in the values of k_0 and especially σ between the two species.

B. MODEL II.

1. Presentation of Model II.

Model II is based on certain assumptions regarding electronic excitation energy transfer in disordered BZP. The disorder inherent to vapor-quenched BZP is assumed to be uniformly distributed. That is, any defect site that occurs in one portion of the sample also occurs in all others with a uniform probability. As a consequence, the number of acceptor or trap sites in the system are assumed to be uniformly distributed.[33]

Only two modes of depopulation of the exciton states are assumed to occur. They are: (1) natural decay resulting from both radiative relaxation and nonradiative coupling to

interand intramolecular relaxation pathways and (2) exciton annihilation resulting from encounter of an exciton with an acceptor molecule. An acceptor is a structurally dissimilar molecule which lies lower in energy than the exciton donor states. Exciton annihilation due to trapping is also assumed to be irreversible provided the energy difference between the donor state and acceptor state is greater than $k_B T$. $k_B T$ is about 13 cm^{-1} (18 K) in the experiments of this project. This criterion is normally satisfied at this low temperature and for the samples of this project.

Exciton transfer in vapor-quenched BZP occurs by the same mechanism as in the crystalline system, i.e the exchange interaction. The exchange interaction relies on the overlap of the charge clouds of neighboring molecules. Also, the magnitude of the exchange interaction energy between an exciton donor and an exciton acceptor is assumed to be the same as between two donors.

The transport of an excitation is assumed to be well described by a hopping mechanism. This being the case, the exciton is assumed to execute a random walk among the donor states until it encounters an acceptor. The number of new sites visited by the excitation therefore, scales with time. Also, the number of donor sites encountered by an exciton prior to trapping defines a certain domain size associated with that particular exciton.

In order to derive an equation concerning the probability

of an exciton encountering a certain number of donor sites (i.e. defining a domain size) the number of acceptor sites exclusive of the exciton domain must be determined. Following Kopelman,[33] this is accomplished using combinatorial analysis as follows.

Vapor-quenched BZP will be assumed to be composed of M molecules, Z of which are traps or excitation acceptors. The mole fraction of acceptors is defined as:

$$C = \frac{\gamma Z}{M} \qquad (5)$$

The interaction of an excitation with an acceptor is described by the efficiency factor γ. γ will be assumed equal to one for vapor-quenched BZP. In other words, thermal repopulation of donor sites subsequent to exciton trapping is assumed to be negligible since the acceptor states are normally in excess of 100 cm^{-1} lower in energy than the donor states.

The number of ways of selecting Z acceptors from M molecules or sites (the term site and molecule will be used synonymously in the following) is obtained from counting the number of possible combinations of Z acceptors among M molecules.

$$P(M,Z) = \frac{M(M-1)(M-2)(M-3)\ldots(M-Z+1)}{Z(Z-1)(Z-2)\ldots(Z-Z+1)}$$

$$= \frac{M!}{(M-Z)!\, Z!}$$

$$= \begin{pmatrix} M \\ Z \end{pmatrix} \qquad (6)$$

The notation used in equation (6) is simply the binomial coefficient for the number of ways of dividing Z objects among M objects.

In the discussion above, it was mentioned that the exciton undergoes a finite number of hops before encountering an acceptor. Thus there must be a certain number of sites n which do not contain any of the Z acceptors. n is defined as the number of sites which form a region which does not contain any acceptors. Therefore, the total number of sites from which the Z acceptors can be chosen is reduced by some amount M-n. The number of ways of selecting Z acceptors from M-n sites is given by

$$P(M-n,Z) = \frac{(M-n)(M-n-1)(M-n-2)\ldots(M-n-Z+1)}{Z(Z-1)(Z-2)(Z-3)\ldots(Z-Z+1)}$$

$$= \frac{(M-n)!}{(M-n-Z)!\ Z!} = \begin{pmatrix} M-n \\ Z \end{pmatrix} \qquad (7)$$

Using combinations (6) and (7), the probability (P_n) of observing n sites with zero acceptors is:

$$P_n = \frac{P(M-n,Z)}{P(M,Z)} = \frac{[(M-n)(M-n-1)\ldots(M-n-Z+1)/Z!]}{[M(M-1)(M-2)\ldots(M-Z+1)/Z!]}$$

$$P_n = \left(1-\frac{n}{M}\right)\left(1-\frac{n}{M-1}\right)\left(1-\frac{n}{M-2}\right) \ldots \left(1-\frac{n}{M-Z+1}\right) \qquad (8).$$

Equation (8) can be simplified if $M \gg Z$. Making this simplification, equation (8) can be written

$$P_n = \left(1-\frac{n}{M}\right)^Z \qquad (9).$$

Equation (9) is the probability of observing a domain of size n with zero acceptors among the n sites. Since the probability of observing no acceptors among n sites is P_n the probability (P_Z) of observing at least one acceptor among n sites is simply $1-P_n$

$$P_Z = 1-P_n$$

$$= 1-\left(1-\frac{n}{M}\right)^Z \qquad (10).$$

Again we recall the simplifying approximation $M \gg Z$. With this in mind, P_Z can be rewritten in the following form

$$P_Z = 1 -\exp[-Z(n/M)]$$

$$= 1 - \exp[-n\,C] \qquad\qquad (11)$$

where $C = Z/M$. Equation (11) is an important result as it enables the exciton transfer probability to be determined. It is dependent only on the number of sites visited by an exciton prior to trapping and the acceptor mole fraction. The exciton transfer probability will appear in the final equation of model II. This equation will be used to extract information from radiative decay curves used to interpret the crystallization path of vapor-quenched BZP.

Equation (11) is interpreted as the probability of observing n sites where at least one of the sites is an acceptor. Therefore, the probability of an excitation being trapped after visiting n sites is P_z. P_z is formally considered to be the probability of exciton trapping with the probability of exciton trap interaction being dependent on the number of sites visited prior to trapping and the acceptor mole fraction of the whole system.

For the purpose of modeling the time dependent exciton population, two important points must be restated. First, only two modes of depopulation of the exciton states are assumed, namely natural decay and trapping. The second point is that exciton transport is well described by a hopping mechanism. With these things in mind, the time dependent exciton population is described as the product of the probability of exciton transfer times the probability of

natural decay. P_z does not describe the probability of exciton transfer; $1-P_z$, however, does.

$$P_h = 1 - P_z \qquad (12).$$

P_h is the probability of exciton transfer after n sites visited in a domain with at least one trap present.

Using equation (12), the population of excitons at any given time can be written as

$$E(t) = E_0 (1 - P_z) e^{-kt} \qquad (13)$$

where k is the natural decay constant and E_0 is the instantaneous exciton population subsequent to pulsed excitation. Equation (13) can be rewritten by directly substituting P_z into equation (13) with the result

$$E = E_0 \exp(-nC) \exp(-kt) \qquad (14).$$

Equation (14) represents the exciton population of a particular domain at a particular time where the excitation visits n distinct sites or molecules prior to being trapped. It should be noted that the acceptor mole fraction C is that of the system as a whole.

For the purpose of extracting information from radiative decay curves the sample is assumed to be composed of many

domains resulting from the quench process. These domain sizes are defined by the number of molecules an excitation encounters before being trapped. Subsequent to pulsed excitation, there are many excitations present in the sample. At a particular time, the number of sites visited by many of these will define different domain sizes. The number of different domain sizes will depend primarily on the extent of disorder. The distribution of domains will therefore depend strongly on the extent of local anisotropy which, in turn, determines the degree of crystallinity in the sample. For example, the distribution of domain sizes in the crystalline case is expected to be very narrow and peaked about a large value, relative to the case of an amorphous sample. This is due to the long-range order in crystals.

Provided a low intensity excitation source is used, it is acceptable to assume that each of the excitation domains in vapor-quenched BZP is independent. That is, an exciton in one domain is completely unaffected or uncorrelated with an exciton in a neighboring domain. An exciton is also assumed not to cross over into a neighboring domain. The domains are assumed to be composed of a finite number of sites and are believed to be completely random with respect to the number in a given domain. Invoking these assumptions, the distribution of domain sizes is assumed to follow Poisson's distribution.[16] That is, the number of molecules an exciton encounters in a particular domain before encountering an

acceptor is given by

$$P(n) = \frac{e^{-<n>} <n>^n}{n!} \qquad (15).$$

where $<n>$ is the average number of sites visited over the lifetime of the exciton population for the system as a whole. Equation (15) is the Poisson random variable for a given value of n and $<n>$. $P(n)$ is completely described by the average number of sites visited for the system, $<n>$. To determine the probability mass function the random variable is summed over all possible values of n.

$$P(n) = \sum_{n=0}^{\infty} \frac{e^{-<n>} <n>^n}{n!} \qquad (16).$$

Applying this to the model implies that there is a Poisson distribution of first order differential equations each describing the time dependent exciton population of a collection of domains of size n. The relative number of domains where an excitation makes n hops is given by the value of the Poisson random variable for that value of n. The solutions to the distribution of first order differential equations are:

$$E_0(t) = A_0 \exp(-n_0 C - k)t \qquad (17)$$
$$E_1(t) = A_1 \exp(-n_1 C - k)t \qquad (18)$$

$$E_2(t) = A_2 \exp(-n_2 C - k)t \tag{19}$$

$$E_3(t) = A_3 \exp(-n_3 C - k)t\ldots\ldots \tag{20}.$$

summing equations 17 through 20 over all possible domain sizes

yields

$$E_n(t) = \sum_{n=0}^{\infty} A_n \exp(-nC - k)t \tag{21}$$

where A_n is a weighting coefficient corresponding to the instantaneous exciton population, E_0 of each domain and the Poisson random variable of observing a particular domain size. The decay function is summed over all possible domain sizes. Substituting E_0 and the Poisson random variable for A_n

$$E_n(t) = E_0\, e^{-kt} \sum_{n=0}^{\infty} \frac{e^{-<n>} <n>^n}{n!}\, e^{-nC} \tag{22}.$$

Recognizing Taylor's expansion for e^x i.e.

$$\sum_{n=0}^{\infty} \frac{x^n}{n!} = e^x \tag{23},$$

equation (22) reduces to

$$E_n(t) = E_0 \; e^{-kt} \; e^{-<n>} \sum_{n=0}^{\infty} \frac{(<n> \; e^{-C})^n}{n!}$$

$$= E_0 \; e^{-kt} \; e^{-<n>} \; \exp[<n> \; e^{-C}]$$

$$= E_0 \; e^{-kt} \; \exp[<n> \; (e^{-C}-1)] \qquad\qquad (24).$$

Equation (24) describes the exciton population with time and is a function of k the natural decay constant, C the acceptor mole fraction and $<n>$ the average number of donor sites visited by excitations in the system prior to encounter with traps. Equation (24) contains all of the basic physics inherent to the assumptions of model II.

In order to apply this model to the annealing dependent radiative decay curves of vapor-quenched BZP the explicit time dependence of $<n>$ must be assumed. Following Montroll and Scher, the number of sites visited by a random walker in a disordered system is postulated to scale as t^α.[45] The average number of sites visited will be defined as $<n> = (\kappa t)^\alpha$, where κ is the average transfer rate of an exciton in a particular structural phase and α is the average dispersion parameter.[44] The average number of sites visited, $<n>$ of equation (24) is defined in this manner since the actual number of sites visited varies between excitons/domains. Therefore, $<n>$

correlates with the average behavior of all excitons in the sample.

The basic form of the definition of <n> was first postulated by Montroll and Weiss for the case of a random walker on a three dimensional cubic lattice.[38] The motion of the random walker in their development was assumed to be diffusive, i.e $\alpha=1$. Later, Montroll and Scher postulated that the number of sites visited in a disordered system scaled as t^{α}. Since then the definition of <n> invoked in this development has been derived and implemented in the study of many types of relaxation processes in disordered solids.[44,48,53,55]

Substituting the postulated form of <n> into equation (24), namely $<n> = (\kappa t)^{\alpha}$ yields

$$E(t) = E_0 e^{-kt} \exp[(\kappa t)^{\alpha}(e^{-C} -1)]$$

$$= E_0 \exp[\beta t^{\alpha} -kt] \qquad (25)$$

where $\beta = \kappa^{\alpha}(e^{-C} -1)$.

Equation (25) is the equation which will enable information to be extracted from the radiative decay curves of vapor-quenched BZP and BZP-d_{10}.

Equation (25) describes how the exciton population changes with time as a function of the probability of natural decay and the probability of exciton transfer. The transfer

probability is dependent on α which is defined on the interval $0\langle\alpha\leq1$. α can be correlated with the average exciton transfer time.[48] When α is close to 1, the average time between hops is small. When α approaches zero, the average time between hops is large. α describes the dispersion in the transfer times resulting from variations in the average local structural anisotropy.[22] Regarding the samples of this project, the structural anisotropy as indicated by α is dependent on the nature of intermolecular charge cloud overlap, in particular the carbonyl moiety charge clouds. An α value near 0 means less optimum charge cloud overlap. An α value near 1, extracted from a radiative decay profile means less structural anisotropy (i.e. more optimum charge cloud overlap). Changes in α values as a function of annealing temperature indicate changes in structural anisotropy (i.e. variations in charge cloud overlap) and thus changes in crystallinity.

The argument of the exciton transfer probability term of equation (25) also contains the adjustable parameter β. β is the product of $<n>$ and $(e^{-c}-1)$. Thus β scales linearly with the average exciton transfer domain and exponentially with the acceptor mole fraction. Therefore, the functional dependence of β as a function of annealing temperature scales with the size of crystalline domain sizes. As the crystalline domain sizes increase $<n>$ increases and C decreases. The opposite is true for decreasing crystalline domain sizes.

In order to calculate $<n>$, κ must be either assumed or measured by experiment. The experimental measurement of κ for both crystalline and disordered phases has already been accomplished by Hochstrasser and Hunter et.al.[23,24] They conducted experiments measuring the transfer efficiency of triplet excitons in the slowly cooled melt of BZP to be of order 10^5 sec^{-1}, using NAP as a guest impurity. They argued this to be the case because the lifetime of disordered, neat BZP as a cooled melt is essentially the same as that of the crystal. This implies the contribution due to trapping of the excitation is negligibly small. The important feature of this is that as the three dimensional, long-range order is reduced, the excitation encounters new sites at a slower rate. This indicates that the probability of transfer is reduced due to off resonance interactions. $\kappa=10^5$ sec^{-1} represents an upper limit to the characteristic transfer rate for disordered neat BZP. There are no dispersions in the transfer rate reported by Hunter et. al. since the radiative decay is apparently of single exponential character.

The other factor in β namely, $(e^{-c}-1)$ is recognized as the Taylor series expansion of the acceptor mole fraction. Taking the first term yields an equation for E(t) describing a system composed of domains of the same size.[44] In other words, the system is well characterized by only the most probable value of the Poisson distribution.

The basic form of equation (25) has been used by many

researchers.[1,9,15,21,22,30,31,41,44,53-55]   However,   the   conceptual
development with regard to defining vapor-quenched BZP in
terms of average domain sizes which are Poisson distributed
and average hop rates is different than these. This leads to
a different development and form of β than arrived at by other
investigators.   It is important to note that the form of β
given here reduces to that used by others if the first term
of the expansion over the acceptor mole fraction is the only
term considered.

2. *Application of Model II to Experimental Results.*

The radiative decay curves which resulted from the
cyclic-annealing experiments of this project were analyzed
using equation (25). The natural decay constant k was chosen
to be 100 sec^{-1} as it is within the range of values reported
in the literature for BZP phosphorescence.[37] β and α are the
adjustable parameters used to determine best fits of equation
(25) to BZP and BZP-d$_{10}$ radiative decay curves as a function
of annealing.

Figure 53 illustrates α plotted as a function of
annealing temperature in the range 18 to 180 K for BZP. α
for BZP is observed to decrease in the annealing temperature
range 18 to 40 K and increases rather continuously in the 40
to 180 K range. Figure 54 exemplifies the behavior of α for
BZP-d$_{10}$ upon annealing in the range 18 to 180 K. α decreases

Figure 53. α of model II for BZP versus annealing temperature (in K) in 10 K increments in the range 20 to 180 K. A 2 K anneal took place in the range 18 to 20 K. The uncertainty in α is roughly ±.03.

Figure 54. α of model II for BZP-d_{10} versus annealing temperature (in K) in 10 K increments in the range 20 to 180 K. A 2 K anneal took place in the range 18 to 20 K. The uncertainty in α is roughly ±.03.
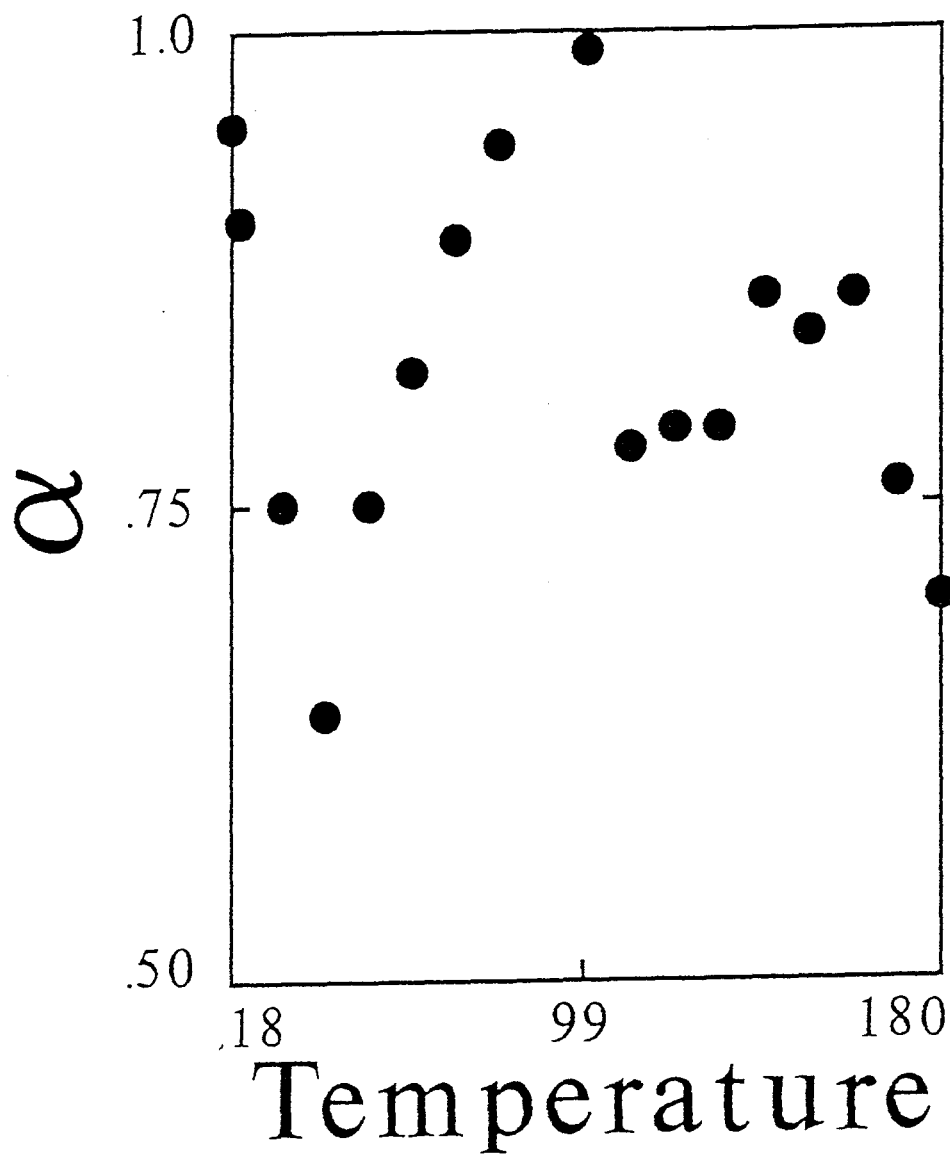
in the 18 to 40 K annealing range and increases to its maximumwith annealing in the range 40 to 90 K. It is noted that α for BZP-d_{10} upon the 90 K anneal is equal to one. α generally decreases with annealing in the 90 to 180 K range.

Viewing figures 53 and 54 comparatively, the primary difference between α for BZP and BZP-d_{10} is that the changes in α with annealing for the BZP-d_{10} sample are greater. The range of α values spanned by BZP-d_{10} over the annealing range 18 to 180 K are about a factor of two greater than α for BZP.

Figures 55 and 56 illustrate the behavior of α for BZP and BZP-d_{10} with annealing in the range 18 to 50 K. α for BZP decreases in the annealing range 18 to 30 K; this increases in the 30 to 50 K range. Figure 56 illustrates the behavior of α for BZP-d_{10} in the annealing range 18 to 50 K. The fluctuations in α for the BZP-d_{10} sample are such that no identifiable trend is observed.

Figures 57 and 58 exemplify changes in <n> for BZP and BZP-d_{10} with annealing in the range 18 to 180 K. <n> was calculated for BZP and BZP-d_{10} as a function of annealing temperature using the α values of figure 53 and 54, $\kappa=10^{5}$ sec^{-1} and t=.05 sec. t is the time interval over which the radiative decay curves were recorded. The general trends for both plots of <n> are simply those of the respective plots of α. The average number of sites visited for the BZP and BZP-d_{10} samples range over the same order of magnitude. <n>

Figure 55. α of model II for BZP versus annealing temperature (in K) in 2 K increments in the range 18 to 50 K. The uncertainty in α is roughly $\pm.03$.
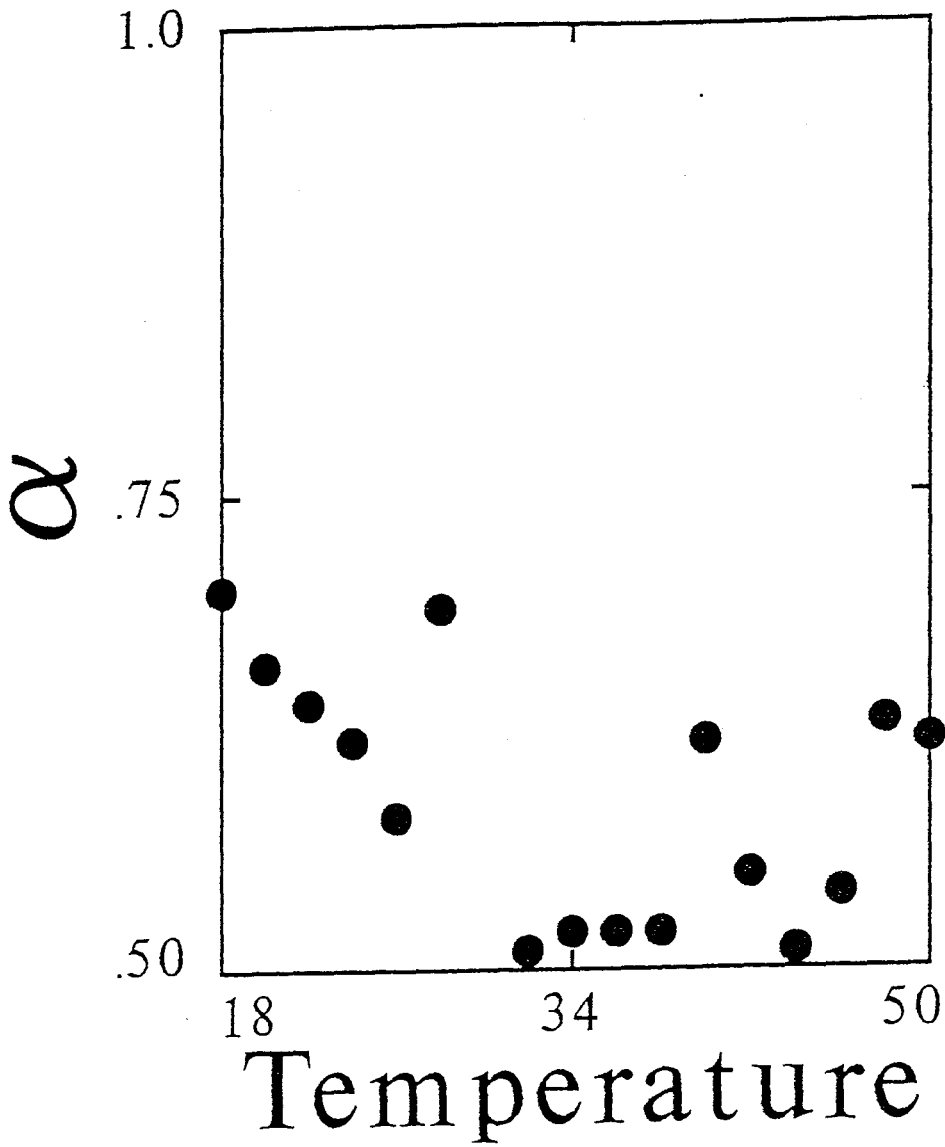
Figure 56. α of model II for BZP-d_{10} versus annealing temperature (in K) in 2 K increments in the range 18 to 50 K. The uncertainty in α is roughly $\pm.03$.
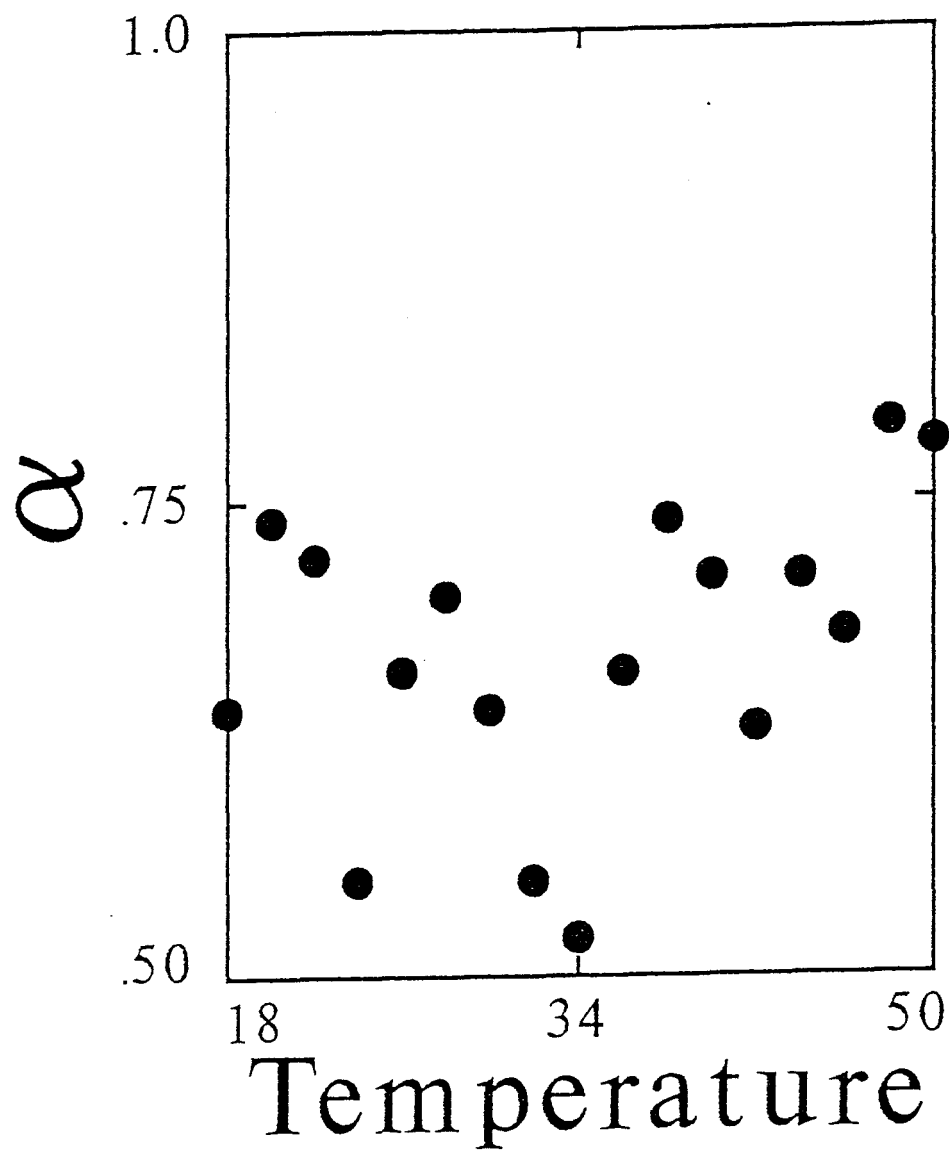
Figure 57. <n> of model II for BZP versus annealing temperature (in K) in 10 K increments in the range 20 to 180 K. A 2 K anneal took place in the range 18 to 20 K.

Figure 58. <n> of model II for BZP-d$_{10}$ versus annealing temperature (in K) in 10 K increments in the range 20 to 180 K. A 2 K anneal took place in the range 18 to 20 K.

for BZP has its range between 150 at 40 K and 1739 at 110 K, while $<n>$ for BZP-d_{10} has its range between 235 at 40 K and 5000 at 90 K. The values of $<n>$ upon the 180 K anneal for BZP (1379) and BZP-d_{10} (338) exemplify the differences between the two samples for the high temperature anneals.

The values of $<n>$ from figures 57 and 58 and the α values of figures 53 and 54 are used to determine the acceptor concentration, C as a function of annealing temperature for BZP and BZP-d_{10}. The acceptor concentration is proportional to the natural logarithm of the inverse of $<n>$.

C versus annealing temperature in 10 K increments in the range 18 to 180 K for BZP is illustrated in figure 59. C increases in the annealing range 18 to 40 K and decreases rather continuously in the annealing range 40 to 180 K. C ranges between .0024 for the 110 K anneal and .023 for the 40 K anneal. Figure 60 exemplifies the behavior of C for BZP-d_{10} in the annealing range 18 to 180 K. C increases with annealing in the range 18 to 40 K and decreases in an exponential manner in the annealing range 40 to 100 K. C increases in the 100 to 180 K annealing range.

As is evident upon comparison of figures 59 and 60, in both samples the acceptor mole fraction changes during annealing by about an order of magnitude. Both samples have a large value of C at 40 K relative to most other annealing temperatures. The higher temperature anneals of the BZP-d_{10} sample yield very different results than for the BZP sample

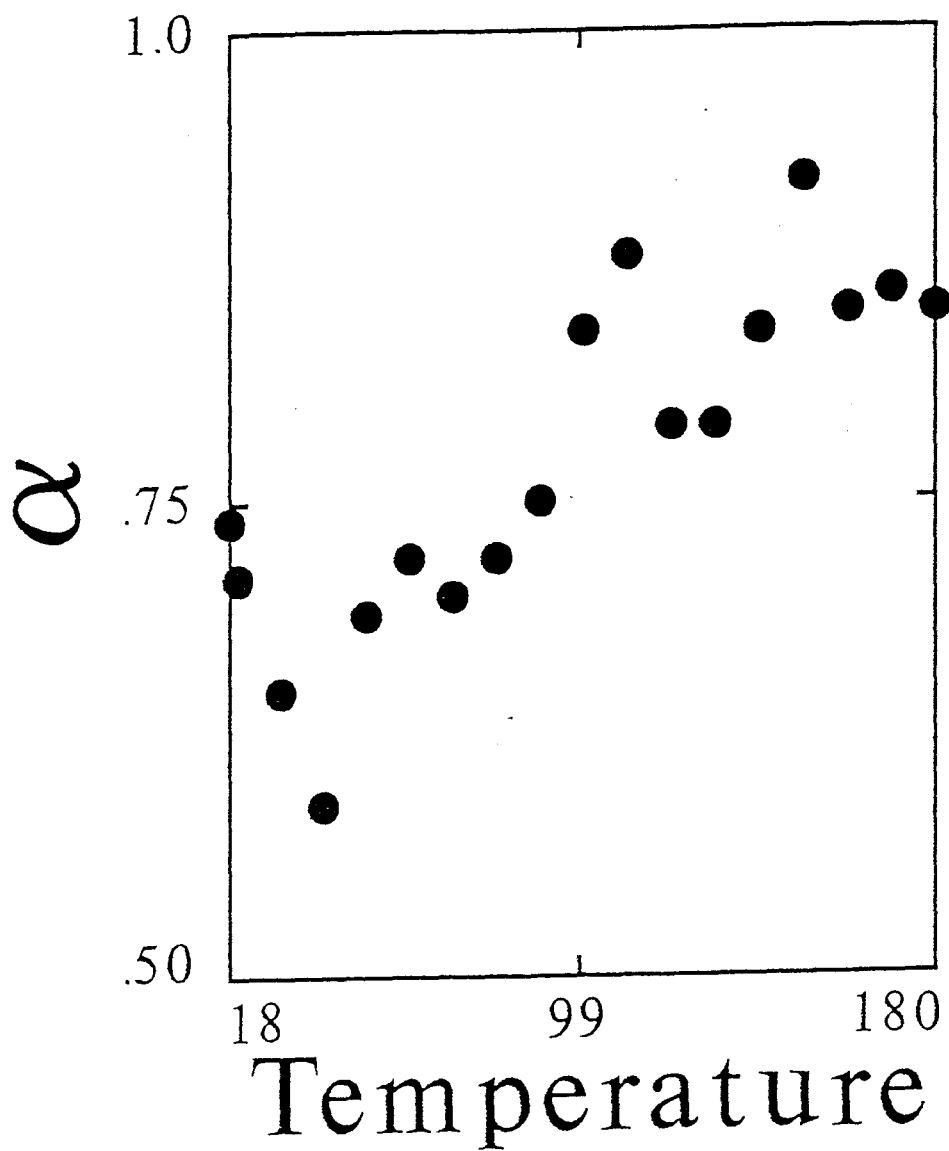Figure 59. C of model II for BZP versus annealing temperature (in K) in 10 K increments in the range 20 to 180 K.   A 2 K anneal took place in the range 18 to 20 K.
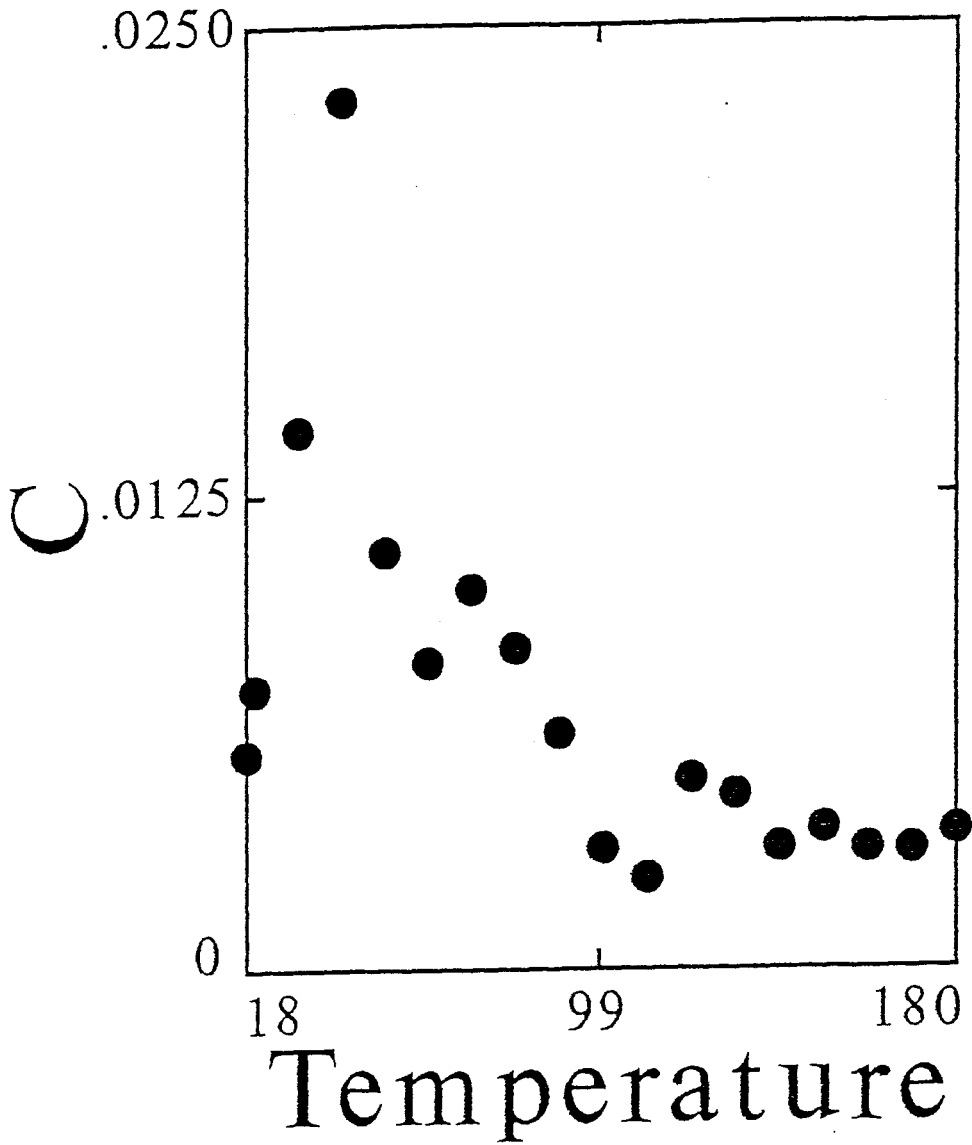
Figure 60. C of model II for BZP-d_{10} versus annealing temperature (in K) in 10 K increments in the range 20 to 180 K. A 2 K anneal took place in the range 18 to 20 K.
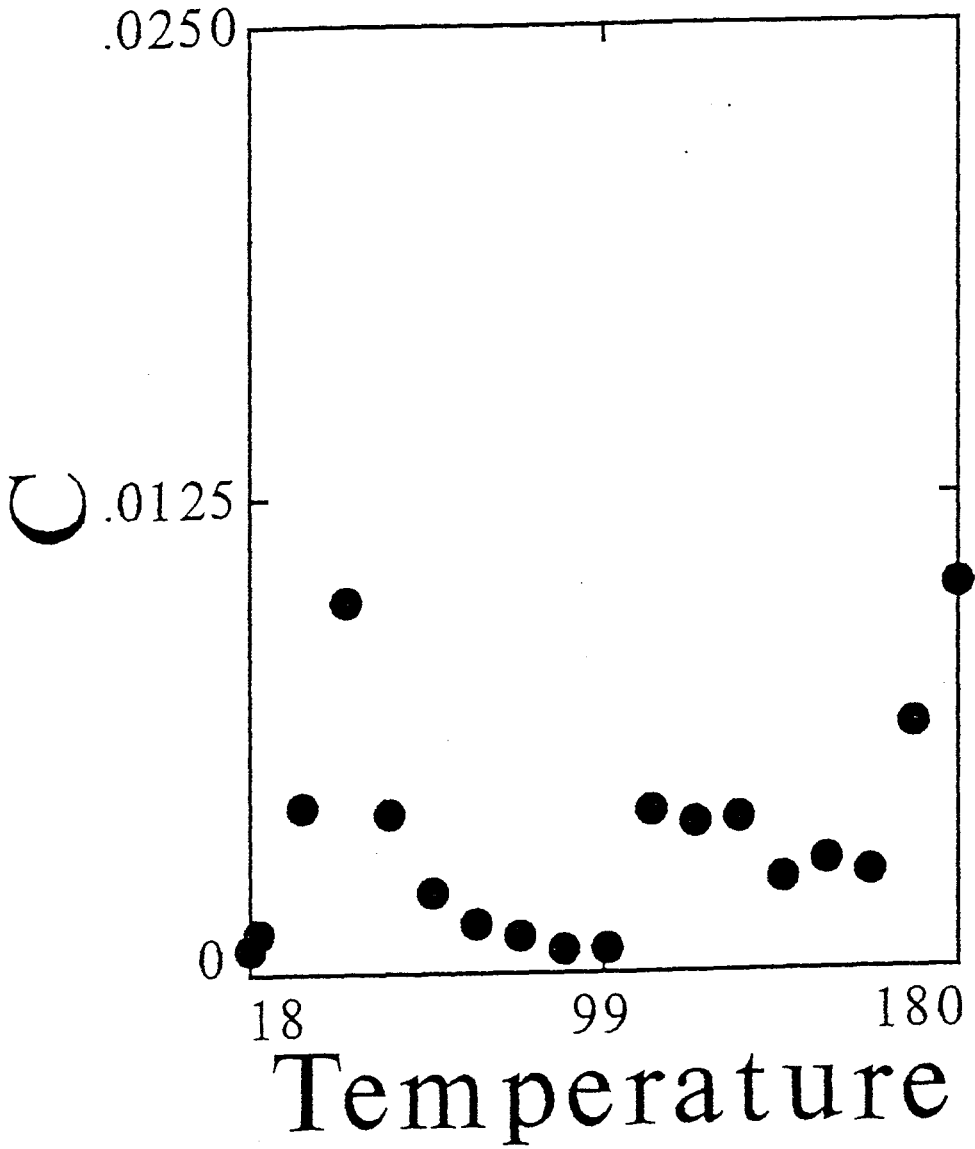
(i.e. between 160 and 180 K). The acceptor mole fraction of the BZP-d_{10} sample changes over a larger concentration range than the acceptor mole fraction of the BZP sample.

The functional dependence of the parameters extracted from radiative decay profiles on annealing temperature were subject to a certain extent of variability for repeated experiments. These variations were primarily due to differences in the sample deposition nozzle position and heating rates. Repeated experiments revealed trends very similar to the results presented in this chapter. For example the magnitudes of the parameters including experimental uncertainty were different for different experiments by as much as five percent. However, their functional dependencies on annealing temperature appears to be the same for repeated experiments. The differences indicate that there exists a certain sensitivity of the crystallization process to initial conditions and the time-frame of each annealing cycle. The similarities, on the other hand, demonstrate that actual trends are indicated by the parameters concerning the crystallization of BZP.

CHAPTER V

CYCLIC-ANNEALING INDUCED STRUCTURAL TRANSFORMATIONS OF DISORDERED BENZOPHENONE, BENZOPHENONE-d_{10} AND NAPHTHALENE/BENZOPHENONE MIXTURES

Vapor-quenched films of BZP, BZP-d_{10}, and NAP/BZP were prepared in a state far from the crystalline state. They were prepared by condensing each molecule at a rate greater than the crystallization rate. Annealing vapor-quenched samples enabled passage of the amorphous solid to the crystalline state. Cyclic-annealing techniques allowed the progress of the crystallization process to be controlled and monitored in a sequential manner. Each spectroscopic measurement was made under conditions where the system was in a state of minimal change, i.e. at 18 K. The optical spectroscopic and annealing experiments of this project indicated certain important aspects concerning the microscopic processes which occur as vapor-quenched films of BZP, BZP-d_{10} and mixtures of NAP/BZP crystallize. The crystallization of BZP-d_{10} was examined with regard to the sensitivity of crystallization to minute, molecular perturbations (i.e. isotopic substitution). Experiments were also performed using mixtures of NAP/BZP in order to examine the effects of substitutional impurities on

189

the crystallization of BZP.

As-deposited films were visually transparent and thus homogeneous on the length scale of visible light. The annealing induced changes in the optical homogeneity of vapor-quenched BZP were evident from variations of I_s with annealing temperature. Results were such that I_s remained relatively constant with annealing temperature in the range 18 to 160 K. I_s evidenced sample density fluctuations on the length scale of visible light with annealing temperature only beginning in the range 160 to 180 K. This indicated the formation of crystalline domain sizes some of which were of size on the length scale of visible light. The annealing behavior of I_s is the first significant result concerning the crystallization of vapor deposited BZP. The results evidence that as BZP passes from amorphous to microcrystalline phase space, the visible signs of this passage are not actually evident until barriers of a certain height are crossed. The barrier heights as evidenced by the behavior of I_s for BZP are apparently of order 100 cm^{-1}.

The vast majority of crystallization experiments are concerned with processes which occur on no less than the length scale of visible light. This is in great contrast to the optical spectroscopic data of this project. The inherent sensitivity of emission spectroscopy to structural transformations enabled investigation of processes on a length scale much less than that of visible light. This was

primarily due to the extreme sensitivity of BZP triplet electronic excitation energy transport to small variations in microscopic interactions in the condensed phase. Emission spectroscopic data demonstrate that many transformations take place on a microscopic scale in the path toward crystallization. The data also show that these transformations are neither trivial, nor random. Rather these transformations appear to occur in a particular sequence as the sample is annealed in the range 18 to 180 K.

Optical spectroscopic data evidence that structural transformations leading to the crystallization of BZP are of two interdependent types. That is, structural changes concern the configuration of individual BZP molecules and the collective structure of BZP domains. Spectroscopic data were used to identify how these local and non-local properties changed during crystallization and what these changes teach about the specific crystallization process. A first step toward accomplishing this was understanding the interactions responsible for variations in the $T_1 \leftarrow S_0$ transition energy and electronic excitation energy transport in BZP.

Variations in the $T_1 \leftarrow S_0$ transition energy of BZP depend primarily on two interactions.[56] The first is the interaction of the excited triplet state with its ground state surroundings. This nonresonant interaction energy is very small for BZP owing to its small oscillator strength, i.e. $f \sim 10^{-7}$. The term "nonresonant interaction energy" is used to

describe the interaction energy of excited BZP with its ground state surroundings. The magnitude of the nonresonant interaction energy is exemplified by differences in $T_1 \leftarrow S_0$ transition energies of BZP in different environments. For example, the observed phosphorescence origin of single crystalline BZP is 24,189 cm^{-1}.[52] This is comparable to the observed phosphorescence origin of BZP dissolved in the non-polar solvent methlycyclohexane (23,890 cm^{-1}) or that observed in the polar solvent mixture EPA (a mixture of ether, pentane and ethanol) (24,210 cm^{-1}). In the extreme case of BZP isolated in the gas phase, the observed phosphorescence origin is apparently 23,800 cm^{-1}.[56] Thus, the nonresonant interaction energy of the excited triplet state of BZP is responsible for only small variations in the $T_1 \leftarrow S_0$ transition energy.

The second and more important factor which determines the $T_1 \leftarrow S_0$ transition energy of BZP is the intramolecular structure which results from condensed phase ground state intermolecular interactions. In particular, the rotation angle ξ of the phenyl rings with respect to the carbonyl axis has been postulated to correlate most strongly with variations in the $T_1 \leftarrow S_0$ transition energy of BZP molecule. Variations of ξ in the range $10° \leq \xi \leq 90°$ have been calculated to be responsible for fluctuations of order 800 cm^{-1} in the $T_1 \leftarrow S_0$ transition energy of BZP.[56] In addition, structurally dissimilar molecules classified as exciton acceptors or traps have been observed to emit more than 1800 cm^{-1} lower in energy than the

phosphorescence origin of the band states of BZP. This observation has been made for disordered samples of both vapor-quenched and vitreous phase BZP.[42,44] The term "vitreous phase" is used to denote a sample of liquid BZP which has been rapidly quenched using liquid nitrogen or helium.[40] These calculated and observed differences for the $T_1 \leftarrow S_0$ transition energy are comparable to the nonresonant interaction energy of an excited molecule whose oscillator strength is f~0.1 (i.e. spin allowed transitions).

In the condensed phase ground state, intermolecular interactions (i.e. dispersion forces) are responsible for the shapes of individual BZP molecules. It is these shapes which correlate with the observed $T_1 \leftarrow S_0$ transition energies. In the vapor-quenched samples of this study, random variations of the intermolecular potential energy resulting from the quench process lead to a random distribution of phenyl ring twist angles, ξ. This results in a random distribution of $T_1 \leftarrow S_0$ transition energies. Phosphorescent BZP molecules serve as optical indicators of changes in individual molecular shapes and the collective structure of BZP domains. Variations of the nonresonant interaction energies of the T_1 state are of negligible importance.

Triplet state electronic excitation energy transport in condensed phase BZP is governed by the exchange interaction (of order 0.3 cm^{-1}).[24] The exchange interaction depends on the magnitude of the intermolecular overlap of an excited charge

cloud with a ground state charge cloud. Dexter postulated that the exciton transfer probability where the exchange interaction is operative scales exponentially with distance, i.e. $e^{-\psi r}$.[10,11] He proposed this based on the functionality of hydrogen atom wave functions.

In vapor-quenched films of BZP a range of intermolecular interaction energies is expected resulting from the quench process. The distribution of charge cloud overlap (i.e. intermolecular distances) determines the distribution of intermolecular interaction energies responsible for different molecular shapes. By logical extension, it is reasonable to assume that a range of exciton transfer efficiencies is operative in vapor-quenched BZP. Variations in the range of transfer efficiencies can be observed using time resolved spectroscopy and model parameters. Time resolved spectroscopy of excited state BZP thus serves as an indicator of changes in the individual molecular shapes and the collective structure of BZP domains.

Having discussed some particulars of BZP spectroscopy the significance of parameters extracted from spectra and modeling of radiative decay curves is discussed. The functional dependence of these data can then be discussed with regard to the crystallization of BZP.

A. EMISSION SPECTRA / ANNEALING BEHAVIOR

The parameters E_{max}, FWHM, I_{0-2}/I_{0-0}, and I_{tot} are indicative of the microscopic interactions affected during cyclic-annealing of vapor-quenched BZP. The magnitude and direction of change of these parameters characterizes the processes by which vapor-quenched BZP crystallizes.

E_{max} is associated with the average emitting site energy of the exciton band states of BZP. The average emitting site energy is determined primarily by different molecular shapes which are a function of the quench process and condensed phase intermolecular interactions. The average of the distribution of molecular shapes associated with single crystalline BZP results in an observed E_{max} approximately 600 cm^{-1} greater in energy than as-deposited, vapor-deposited BZP. This is important as it indicates that the average intramolecular coordinates of vapor-quenched BZP are not the same as those of the single crystal.

E_{max} increases continuously with annealing temperature for BZP having its most marked changes between 40 and 90 K. The BZP phosphorescence origin shifts to higher energy by approximately 100 cm^{-1} in this annealing temperature range. This is still 500 cm^{-1} lower in energy than the single crystal, but it indicates that the average molecular configuration redistributes to a value more closely associated with the single crystal. Based on this one variable, the films of this

project apparently approach microcrystalline states with cyclic-annealing. That E_{max} is a maximum and constant in the annealing range 90 to 180 K demonstrates that the average of molecular structures is apparently set well before any visible signs of crystallization become evident.

The FWHM of the 0-0 vibrational band of BZP correlates with the variance of the distribution of exciton emitting site energies and hence the variance of the distribution of molecular shapes. The FWHM of as-deposited, vapor-quenched BZP is about 300 cm^{-1} greater than that of the single crystal.[24,44] This indicates that there exists a greater number of different molecular shapes in the vapor-quenched sample as compared to the single crystal.

The decreasing trend in the FWHM of BZP is continuous with annealing temperature, having its most marked changes in the range 40 to 120 K. That the FWHM narrows as the film is annealed indicates that BZP molecular shapes evolve toward those of the single crystal. Based on changes in the FWHM, the formation of microcrystalline structures appears to be gradual and continuous over the annealing range. The narrowing of the FWHM, like changes in E_{max}, demonstrates that the variance of molecular shapes finds a minimum well before any visible signs of crystallization emerge. However, the FWHM continues to change with annealing up to 120 K, demonstrating that while the average intermolecular shape is set at 90 K the number of different shapes continues to

decrease until 120 K. That the FWHM never converges to the value associated with the single crystal indicates the system is somewhere in between the single crystalline state and the completely amorphous state. Thus, the annealed film must contain a mixture of both microcrystalline and amorphous domains.

I_{0-2}/I_{0-0} correlates with the different electronic-vibrational transition probabilities of the emitting sites of vapor-quenched BZP. These transition probabilities, in turn, correlate with the precise intramolecular coordinates of each emitting site. In addition, I_{0-2}/I_{0-0} correlates with the acceptor mole fraction which also depends on the precise intramolecular coordinates of each acceptor emitting site. Thus, I_{0-2}/I_{0-0} is a measurement which is directly associated with annealing dependent changes in the average molecular shape. A plot of I_{0-2}/I_{0-0} versus annealing temperature indicates how the BZP structure changes along the crystallization path.

I_{0-2}/I_{0-0} for single crystal BZP is very sensitive to the quality of the crystal. A poor quality crystal will exhibit I_{0-2}/I_{0-0} values close to vapor quenched BZP. I_{0-2}/I_{0-0} for vapor-deposited BZP is about 2.6 times greater than the ratio observed for a high quality single crystal.[12] This implies that a different distribution of molecular shapes is operative in the disordered film. I_{0-2}/I_{0-0} for BZP decreased between the annealing temperatures of 50 and 180 K, equaling one for the

180 K anneal. This indicates that the intramolecular coordinates approach those of the crystal during annealing. The value of I_{0-2}/I_{0-0} observed for the 180 K annealed sample of this study is about a factor of 2 greater than that observed for a high quality single crystal. This implies that the 180 K annealed, vapor-quenched film is not entirely crystalline.

The important feature of I_{0-2}/I_{0-0} is that it is very sensitive to changes in the molecular coordinates. As an indicator of the crystallization path of BZP, I_{0-2}/I_{0-0} demonstrates that the trend toward crystalline-like coordinates is continuous. However, the path demonstrates a certain non-trivial structure as the annealing temperature is increased. The structure suggests that the crystallization pathway of vapor-quenched BZP in this experiment is rather complicated. It also indicates changes in the intramolecular coordinates leading to the crystalline state occur well before any visible signs of crystallization.

I_{tot} correlates with the density of emitting sites and the nonradiative degrees of freedom. The radiative quantum yield can be defined by $Q = k_R/(k_R + k_{NR})$, where k_R is the pure radiative decay rate and k_{NR} is the nonradiative decay rate of an emitting population. Keeping this in mind, it has been observed that the effect of different environments on the radiative decay rate of BZP is small. The lifetimes of BZP recorded for the crystal, slowly cooled melt and frozen solvent solution are nearly the same.[24,37] This indicates that

nonradiative depopulation mechanisms in the absence of appreciable exciton trapping are slightly environment specific for BZP.

I_{tot} has also been postulated to depend on the intramolecular coordinates BZP molecule.[56] Computer simulations indicate that changes in ξ effect the degree of spin-orbit coupling in BZP molecule thereby altering the oscillator strength of the $T_1 \leftarrow S_0$ transition.

I_{tot} for BZP decreases in the annealing range 18 to 40 K and increases in the annealing range 40 to 160 K. The effect of annealing induced changes on BZP molecular shapes seem to be partly responsible for changes in I_{tot}. Also, nonradiative coupling to lattice modes are probably important in the strained environment of vapor-quenched BZP. It is not clear from the data which interactions are primarily responsible for the observed behavior of I_{tot}. It is clear that changes in I_{tot} are very sensitive to annealing temperature and thus the crystallization path. As an indicator of the crystallization of BZP, I_{tot} demonstrates that BZP's crystallization is continuous and nontrivial. The inflection point at 40 K evidences that two different processes dominate structural transformations in the two different annealing temperature regimes. The origin of these processes cannot be specified since the processes responsible for changes in I_{tot} are not completely understood. However, increased coupling to nonradiative modes seems to indicate increased disorder

relative to the single crystal while decreased coupling to the nonradiative modes indicates less disorder with regard to the single crystal.

Well before visible crystallization, the spectral parameters E_{max}, FWHM, I_{0-2}/I_{0-0} and I_{tot} all indicate important events occur during the cyclic-annealing process. They all demonstrate that the components of the film evolve toward the crystalline state. The parameters are different in that the annealing temperature region of greatest change is different for each of them. For example, E_{max} finds its maximum at a lower annealing temperature than the FWHM. This evidences that the average of the distribution of intramolecular coordinates stops changing while the spread in the distribution continues to change with annealing temperature in the range 18 to 180 K.

I_{tot} appears to be the most sensitive parameter to annealing temperature. It indicates that the crystallization path of vapor-quenched BZP is continuous and complicated in the range 18 to 180 K. The other spectral parameters do not evidence this but do show that certain aspects of the crystallization process occur in a particular sequence. All of the functional dependencies of the spectral parameters are in great contrast to the functional dependence of I_s with annealing temperature. The latter indicates that no important crystallization events occur on the length scale of visible light in the annealing temperature range below 160 K.

B.   TIME RESOLVED AND HIGH TEMPERATURE SPECTRA / ANNEALING
BEHAVIOR

Time resolved spectra of vapor-quenched BZP are diagnostic of the energetic distribution of sites sampled by mobile excitations. This energetic distribution is associated with annealing induced variations in the intramolecular coordinates of acceptor sites. The population of acceptor sites is a transport controlled process which can be monitored by time resolved techniques.

Using the time resolved spectra as an indicator of the crystallization path of BZP, two types of emitting site structures are evidenced. The time resolved spectra of figures 32 and 33 indicate two limits with respect to the types of sites sampled by excitons at long times. The two extremes are observed for the as-deposited sample and the sample annealed in the range 18 to 180 K (figures 32 (bottom) and 33 (top)). The as-deposited sample spectrum recorded at a delay time of 50 ms indicates that the types of sites sampled at long delay times are very similar to those sampled at short times, i.e. 400 ns (figure 31). Thus, the as-deposited sample is rather homogenous as indicated by the emitting sites of the 50 ms delayed spectrum possessing a very distinct emission profile which is very similar to the 400 ns delayed spectrum. The 50 ms delayed spectrum recorded

subsequent to the 180 K anneal demonstrates that there exists a large distinction of emitting sites sampled at long times relative to very short times. This is evidenced by the very broad band emission recorded in the 50 ms delayed spectrum relative to the 400 ns delayed spectrum. These experiments evidence that as the film crystallizes it becomes rather inhomogeneous demonstrated by the poorly resolved emitting site energies with regard to the emitting sites sampled at long times.

The transition in the types of sites sampled at long times occurs predominately during the higher temperature anneals, particularly in the range where visible crystallization is observed. The behavior of the time resolved spectra with annealing temperature is similar to I_s in that, both measurements evidence decreasing homogeneity with respect to the observable in the high annealing temperature limit.

The broad band feature of figures 32 and 33, which the BZP carbonyl vibrational bands are superimposed on, is due to molecules whose intramolecular coordinates are very different from the bulk. These molecules act as exciton acceptors. As annealing proceeds, the distribution of acceptor site energies converges to that observed in the 180 K annealed sample spectrum of figure 33 (top).

The efficiency with which acceptor sites are populated appears to increase with annealing upon the formation of

crystalline domains. This is evidenced by the drastic increase in the population of acceptor sites with annealing temperature as recorded by time resolved spectra. The exciton transfer rate in the microcrystalline regions is much faster than in the disordered surroundings. Thus a narrower distribution of lower energy acceptor states is populated more quickly in the microcrystalline limit. The 180 K annealed, delayed sample spectrum of figure 32 (top) indicates the distribution of acceptor site energies.

Spectra recorded at elevated temperatures, i.e. 140 K, are reminiscent of annealed sample spectra recorded at 18 K using long delay times with respect to a pulsed excitation source (i.e figure 33 (top)). Because as the applied thermal energy increases, the average thermal fluctuations of the intramolecular coordinates about their mean approach those of the acceptor sites with respect to the exciton donor sites. Thus, the high temperature time averaged spectrum is reminiscent of molecules which emit at similar energies to those of the delayed spectra. In other words, there exists a similarity between the acceptor sites sampled at long times and those emitting sites with thermal energy of order 100 cm^{-1}.

It is significant that 100 cm^{-1} of thermal energy results in a cw spectrum reminiscent of the 180 K annealed delayed spectrum. Phenyl ring torsional vibrations of BZP are known to be of order 100 cm^{-1}.[5,12] Thus, the 100 cm^{-1} of thermal

energy applied to the sample represents the thermal energy necessary to activate a significant population of BZP torsional vibrations. These vibrations reduce the average $T_1 \leftarrow S_0$ transition energy to that associated with structural impurity exciton acceptor sites. It can thus be inferred that exciton acceptors are BZP molecules which possess much different phenyl ring torsional angles as compared with the bulk. However, by themselves they do not add any new information regarding the crystalline path of BZP. The elevated temperature spectra were, on the other hand, useful in determining the intramolecular interaction most influential in formation of acceptor states.

C. RADIATIVE DECAY MEASUREMENTS / ANNEALING BEHAVIOR

In the development of model I, k_0 was assumed to correlate with the average emitting site energy. The average emitting site energy correlates with the average of the distribution of different molecular shapes. Therefore, k_0 is related to the distribution of molecular shapes. The average natural decay rate of model I for BZP increases with annealing in the range 18 to 40 K and decreases in the annealing range 40 to 180 K. Since nothing concerning electronic energy transport is assumed in model I it appears that fluctuations in the intramolecular coordinates of BZP must be attributed to fluctuations in intramolecular nonradiative coupling and

thus the observed behavior of k_0.

As an indicator of the crystallization path of BZP, k_0 evidences that crystallization is continuous but complicated. A large inflection point is observed at the 40 K anneal indicating that two different structural processes are operative defining two annealing regimes. The behavior k_0 is inversely proportional to I_{tot}. When k_0 is large (at 40 K) the contribution due to nonradiative depopulation is expected to be large. This is verified by the relatively small value of I_{tot} associated with the 40 K anneal. Changes in k_0 with annealing temperature can also be understood in light of the results of model II where exciton transport is assumed.

σ of model I is the variance in the average decay rate of the emitting sites. It is related to the variance of the distribution of molecular shapes. That it increases for BZP with annealing in the range 18 to 40 K indicates the number of different intramolecular emitting site coordinates is increasing. The decreasing trend of σ in the annealing temperature range 40 to 170 K indicates a decrease in the number of different emitting site molecular shapes. That σ increases in the 170 to 180 K annealing range indicates an increase in the number of different intramolecular emitting site geometries.

σ, as an indicator of the path toward the crystalline state of BZP, demonstrates continuous but complicated behavior with a large inflection point at the 40 K anneal. The

behavior of σ reveals that two distinct types of transformations occur before visible crystallization takes place. The interpretation of σ regarding the crystallization path of BZP is that the system proceeds away from the crystalline state before proceeding toward it. The interpretation and behavior of σ is similar to the FWHM only σ appears to be more sensitive to annealing temperature. This is due to the sensitivity associated with intensity measurements and the nonlinear regression method used to fit Equations (3) and (4) to experimental decay curves. These are apparently more sensitive than the measurements of FWHM which are limited by the resolution of the monochromator.

The dispersion parameter, α of model II correlates with the interrelated changes in the average site transfer rate, structural anisotropy, local molecular structure, and intermolecular charge cloud overlap. The behavior of α with annealing temperature indicates that the path to the crystalline state of BZP is continuous and nontrivial, possessing an inflection point associated with the 40 K annealing temperature. The inflection point enables identification of two distinct events which occur as BZP crystallizes. Decreasing α in the range 18 to 40 K evidences changes in the structural anisotropy associated with increasing disorder, while increasing α in the range 40 to 180 K indicates increasing crystallinity (i.e. decreasing anisotropy). These two processes always occur in the same

order in repeated experiments. α also indicates many events occur prior to visible signs of crystallization. The behavior of α in the annealing temperature range 40 to 180 K demonstrates a continuous progression of the film components toward the crystalline state.

That the average exciton transfer efficiency in vapor-quenched films of BZP never reaches that associated with the single crystal, i.e. $\alpha=1$ and $\kappa=10^8$ sec^{-1},[23] evidences that the film components never reach the single crystalline state during the annealing experiment. However, α along with the other data discussed to this point, does indicate microcrystalline behavior. Certainly, there exists both crystalline and amorphous domains in the sample even for the highest temperature anneals used in this project.

The average exciton transfer domain size of vapor-quenched BZP can be estimated using the results of model II. <n> defines the average exciton transport domain size where exciton transfer takes place in the absence of trapping. <n> is an indicator of the crystallization of BZP revealing behavior reminiscent of α. That is, two distinctive events occur as a function of annealing temperature. 1) <n> decreases indicating a trend away from the crystalline state in the annealing range 18 to 40 K and 2) increases evidencing a trend toward the crystalline state with annealing in the range 40 to 180 K.

Because the film is composed of a mixture of

microcrystalline and disordered domains <n>, does not scale directly with the size of microcrystalline domains for the high temperature anneals (i.e. 160 to 180 K). Thus, <n> represents the average between the two types of domains. That <n> increases in the annealing range 40 to 180 K indicates an increase in the transfer domain sizes such that microcrystalline domains are increasing at the expense of disordered domains.

The results of fitting model II to radiative decay curves as a function of annealing enables the functional dependence of C on cyclic-annealing temperature to be recovered. C correlates with the number of molecules possessing intramolecular coordinates which are sufficiently different from the bulk. Such that their $T_1 \leftarrow S_0$ transition energies lie at much lower energy than the exciton band states of vapor-quenched BZP. The increase in C upon annealing in the range 18 to 40 K indicates that as the average intermolecular charge cloud overlap decreases (decreasing α) the number of molecules acting as exciton acceptors increases. Likewise as C decreases the average charge cloud overlap increases and hence the number of displaced molecules acting as exciton acceptors decreases. C decreases as expected as the sample approaches the microcrystalline limit with increasing annealing temperature.

The functional dependence of C is useful in explaining the behavior of the k_0 with annealing temperature. Comparing

figures 49 and 59 demonstrates the marked similarity in the behavior of k_0 and C for BZP with annealing temperature. What is observed upon comparison of the figures is that the changes in k_0 follow closely the changes in C with annealing temperature. This is expected since the average radiative rate of the exciton states will be shortened or lengthened by increasing or decreasing the acceptor mole fraction. Thus the dependence of k_0 on annealing temperature is best interpreted when exciton transport is considered.

The parameters k_0, σ, α, $<n>$ and C which result from modeling the radiative decay curves of neat BZP evidence the film does proceed toward the crystalline state with cyclic-annealing. Some of the parameters demonstrate similar behavior as the film is annealed. For example, k_0 of model I and C of model II behave in a very similar manner. α, on the other hand, behaves as the inverse of σ. This is no surprise since as the variance of the site energies decreases the average hop rate is expected to increase tending toward the single crystalline value. All five parameters resulting from modeling the radiative decay curves of vapor-quenched BZP indicated a continuous progression of the film components toward the crystalline state with annealing in the range 40 to 180 K. They also indicate a progression away from the crystalline state in the annealing range 18 to 40 K demonstrating a certain hierarchy of events occurs along the path of crystallization.

D. *BENZOPHENONE-d_{10} / ANNEALING BEHAVIOR*

The spectral and decay parameters associated with the cyclic-annealing of BZP-d_{10} are strikingly similar in some respects and different in others compared to BZP. It is important to note that both species are electronically identical. Therefore, any differences in the annealing behavior between the two substitutional isotopes are expected to be kinetic in nature.

The experimental results associated with BZP-d_{10} were similar to BZP by way of certain experimental parameters. For example, E_{max} and FWHM yielded the same trends with annealing temperature for both samples. However, the behavior of E_{max} and FWHM was different for BZP-d_{10} in that they both experience measurable changes over a broader annealing temperature range than BZP. Also, the model II parameter α behaved much differently above the annealing temperature of 90 K for BZP-d_{10} compared to BZP.

These observed experimental differences between neat BZP and BZP-d_{10} went beyond variations in deposition conditions and heating rates. These differences indicate kinetic differences between the path of crystallization of BZP as compared to BZP-d_{10}. The differences are only evident over the annealing range 18 to 180 K in 10 K increments. Few differences were observed for annealing over smaller temperature ranges, i.e.

18 to 50 K in 2 K increments. The experimental results indicate the possibility of measuring the sensitivity of cyclic-annealing induced crystallization for isotopically substituted compounds. What the annealing behavior of BZP-d_{10} teaches about the crystalline path of BZP is that small perturbations of the molecule (i.e. deuteration) have measurable affects on the crystallization path.

E. CW EMISSION SPECTRA OF NAPHTHALENE / BENZOPHENONE MIXTURES / ANNEALING BEHAVIOR

Spectroscopic and annealing studies at low temperature of mixed films of NAP/BZP were conducted to investigate the efficiency of exciton transfer and perturbations in packing induced by the structurally different compound NAP in vapor-deposited BZP samples. NAP acts as an exciton acceptor to BZP triplet excitons since its lowest triplet state is much lower in energy. The spectra of the three mole fractions of NAP/BZP (1:2, 1:6 and 1:16) used in this study exhibited different behavior with respect to both exciton transfer efficiency and structural impurity induced packing effects.

In the 1:16 as-deposited NAP/BZP sample BZP phosphorescence dominates the spectrum with only a small amount of NAP phosphorescence present. The as-deposited spectrum indicates the BZP emitting sites in this perturbed sample are very much like the emitting sites of the neat

sample. This is evidenced by the fact that the emission origin and band widths are similar to those of the neat sample. The low intensity of NAP phosphorescence demonstrates the poor efficiency of electronic excitation energy transport in the as-deposited sample. This observation implies that for energy transfer to a NAP acceptor, the BZP triplet exciton must traverse on the order of 20 sites (the concentration of NAP in BZP is of order .05 mole/mole). This is truly a lower limit since the relative efficiency of triplet exciton transfer from BZP to NAP is of order 15 percent.[23,24] Thus, the intensity of the NAP phosphorescence would dominate the spectrum if it were to be adjusted relative to the BZP intensity. Physically this indicates that most of the BZP triplet excitons are trapped by NAP acceptor sites before encountering a BZP acceptor.

Changes in the exciton transfer efficiency are quantitated for the minimally perturbed 1:16 NAP/BZP mixture by plotting $I_{NAP}/(I_{NAP}+I_{BZP})$ versus annealing temperature. $I_{NAP}/(I_{NAP}+I_{BZP})$ correlates with the efficiency of exciton transport. The efficiency is great if the average charge cloud overlap between NAP and BZP is large and less if the overlap is small. The transfer efficiency decreases with annealing in the range 18 to 40 K (figure 47) indicating the average charge cloud overlap decreases leaving the sample in a state with less polycrystalline character than it began with. Annealing in the range 40 to 180 K produces changes in

the transfer efficiency associated with more optimum charge cloud overlap, i.e. convergence toward polycrystalline character. $I_{NAP}/(I_{NAP}+I_{BZP})$ does not appear to converge or level off but changes continuously with annealing. In fact, the greatest changes in $I_{NAP}/(I_{NAP}+I_{BZP})$ occur for annealing temperatures above 160 K. The high temperature (160 to 180 K) behavior of $I_{NAP}/(I_{NAP}+I_{BZP})$ is similar to I_s. I_s indicates relatively large scale fluctuations in the film density in the annealing range 160 to 180 K. Both indicate convergence toward the crystalline state as the film is annealed.

The functionality of $I_{NAP}/(I_{NAP}+I_{BZP})$ is strikingly similar to I_{tot} and α for the experiments with neat BZP. This implies that the 1:16 mixed film behaves in a similar manner with annealing temperature as neat BZP samples. The marked similarity of $I_{NAP}/(I_{NAP}+I_{BZP})$ and α for BZP is demonstrated upon comparison of figures 47 and 53. $I_{NAP}/(I_{NAP}+I_{BZP})$ is a direct measure of the dependence of the exciton transfer efficiency on annealing temperature. That its behavior is essentially the same as α in the annealing range 18 to 150 K confirms the interpretation of the dispersion parameter, α as being correlated with the transport efficiency.

However, the behavior of α is different from $I_{NAP}/(I_{NAP}+I_{BZP})$ for the annealing range 150 to 180 K. In this annealing range $I_{NAP}/(I_{NAP}+I_{BZP})$ experiences its greatest increases with annealing temperature indicating BZP's triplet excitons greatest increase in the transport efficiency. α,

on the other hand, indicates the opposite behavior in the annealing range 150 to 180 K. This discrepancy is interpreted as a breakdown in the assumption of a single exciton transport rate of model II.

All indications are that the system is becoming more microcrystalline in the 150 to 180 K annealing range. As the system becomes more polycrystalline, the number of regimes possessing exciton transfer rates close to the crystal is expected to increase. Thus the annealed, vapor-quenched system may be better characterized by two exciton transfer rates, one corresponding to crystalline regions (e.g. 10^8 sec^{-1}) and another corresponding to disordered regions (e.g. 10^5 sec^{-1}).[20-24] The crystalline transfer rate will have the effect of more rapid transport to the exciton acceptors leading to more rapid depletion of the exciton states. Applying model II to a system such as this will lead to an artificially high value for the acceptor mole fraction. This conjecture is supported by the time resolved spectrum (figure 33 top) and the 1:16 NAP/BZP mixed film results for the high temperature anneals. It is also supported by the behavior of constant C in the annealing range 150 to 180 K where it is expected to be decreasing based on the behavior of $I_{NAP}/(I_{NAP}+I_{BZP})$.

The important point of the 1:16 NAP/BZP mixed film experiment is that the experimental results demonstrate very similar behavior as compared to neat BZP. Thus, this

relatively impure system can be used to learn some important points concerning the crystallization path of neat BZP. That the experimental results of this special case of crystallization are not very different from neat BZP, and that the domains containing only BZP molecules are extremely small, demonstrates just how important local interactions are in the crystallization path of BZP. In addition, the crystallization path is continuous and possesses a very specific hierarchy of events, namely that the film becomes more disordered before becoming microcrystalline. This mixed film experiment only served to support the findings of the neat experiments with regard to the nature of the BZP crystallization path.

The 1:2 NAP/BZP mixture was dominated by NAP phosphorescence with only the 0-1 carbonyl vibrational band of BZP resolved near in intensity to the background. The BZP 0-1 vibrational band disappears with increasing annealing temperature. NAP phosphorescence is the dominant feature in the spectrum at all annealing temperatures. However, subsequent to the 180 K anneal some NAP fluorescence is resolved in the high energy portion of the spectrum.

The fact that any BZP phosphorescence is visible indicates that the efficiency of exciton transfer is poor compared to the mixed single crystal. In mixed NAP/BZP single crystals NAP phosphorescence dominates the spectrum at a mole ratio of $1:10^5$ and greater in NAP:BZP.[23] The results for the 1:2 mixed film are reasonable given the poor packing

efficiency that appears to result in samples of this mole fraction prepared under such severe kinetic constraints. The disappearance of the BZP 0-1 band implies improved packing and transfer efficiency with annealing.

The spectrum of the as-deposited 1:6 NAP/BZP mixture reveals that the NAP impurity has drastically effected the packing of BZP emitting sites. The BZP emitting sites of the 1:6 mixed film are very different from those of neat BZP. This is evidenced by the very broad band spectral profile and complete absence of NAP phosphorescence (figure 40). This is in contrast to the 1:16 NAP/BZP sample and single crystals of NAP/BZP. The perturbation to the lattice structure of BZP crystals by NAP has been demonstrated to be negligible. As a result of the apparent inefficient packing in the 1:6 mole ratio sample there appears to be little or no energy transfer. Figure 41 demonstrates this by the lack of NAP phosphorescence even after a delay of 40 ms with respect to the excitation pulse. This result is rather peculiar considering the large fraction of NAP in the film.

As the 1:6 mole ratio film is annealed to higher temperatures, the distribution of different BZP intramolecular coordinates increases as evidenced by the increased band widths of the spectrum. NAP phosphorescence is observed subsequent to the 120 K anneal. By the 170 K anneal NAP phosphorescence is the dominate feature in the spectrum and the 0-0 and 0-1 carbonyl bands of BZP narrow considerably.

It is apparent that the transfer efficiency of the BZP triplet excitons to the NAP guests improved dramatically compared to the as-deposited sample. In addition, the narrowing of the BZP vibrational bands indicates some BZP intramolecular geometries are similar to the neat sample. This implies a certain amount of phase separation with the high temperature anneals since there is emission resulting from mixed domains and domains reminiscent of neat BZP.

When extremely impure NAP/BZP mixtures are produced, all sorts of unexpected things happen. The 1:2 and 1:6 mixed films were drastically perturbed in comparison to neat BZP. Spectroscopic and annealing experiments evidence the drastic effects of the structural impurity NAP on the packing of vapor-quenched BZP. These experiments evidence the extreme importance of the processes which occur at a local level along the path to crystallization. These mixed films also demonstrate improved exciton transport as crystallization took place in the high annealing-temperature limit.

CHAPTER VI

SUMMARY AND CONCLUSIONS

The special case of the crystallization of vapor-quenched BZP was investigated. Vapor-quenched films of BZP, BZP-d_{10} and mixtures of NAP/BZP were prepared at low temperatures. Cyclic-annealing plus optical spectroscopy enable crystallization to be monitored in a step-wise manner. Optical emission spectroscopy, specifically emission spectra and radiative decay measurements served to characterize transformations of the film components at particular points along the crystallization path.

Compiling and interpreting the spectroscopic data either directly or through modeling illustrated a picture of the microscopic processes related to the crystallization of vapor-quenched BZP. In particular,two kinetic models were used to extract information contained in radiative decay curves. These helped to illustrate further a picture concerning the crystallization of BZP.

The spectroscopic and light scattering data suggest important details about the crystallization of BZP. First, several types of structural transformations occur well before visible signs of crystallization emerge. BZP molecules

apparently progress through amorphous phase space in a direction opposite to the crystalline state with annealing in the range 18 to 40 K. After which, the film components proceed toward crystalline phase space with annealing in the range 40 to 180 K. This indicates a certain hierarchy of events which occur along the path to the crystalline state of BZP.

Two interdependent types of structural transformations were identified with the aid of spectroscopic observables used to elucidate the crystallization path of BZP. They were changes in the average phenyl twist angle ξ as indicated by changes in E_{max} and changes in the local structural anisotropy as indicated by changes in α and $I_{NAP}/(I_{NAP}+I_{BZP})$. Changes in the local structure are clearly a function of ξ. Thus, the two cannot be separated with regard to their importance in characterizing the crystallization path of BZP.

The effects of substitutional deuteriation on the crystallization of BZP were evidenced by experimental data. The functionality of change between BZP and BZP-d_{10} was very similar for most of the experimental parameters. However, the deuterated sample did experience measurable differences in the annealing temperature range over which parameters changed as compared to BZP. These differences relate to kinetic differences between the rates of passage of BZP-d_{10} and BZP to the crystalline state.

The effects of a guest impurity, namely NAP, on packing

and energy transfer in vapor-quenched BZP was determined. Very drastic packing effects were observed in the 1:6 and 1:2 mixed films. No packing effects of NAP with BZP were observed for the 1:16 mixed film. The 1:16 NAP/BZP mixture behaved in a similar manner as neat BZP with cyclic annealing. This mixture served as a good model for investigating the effects of annealing induced crystallization on electronic excitation energy transport in vapor quenched molecular films. The 1:16 mixed film experiment also served to demonstrate the extreme importance of localized processes on the crystallization path of BZP. The importance of localized processes was indicated by the large changes in the BZP exciton transfer efficiency and the large proportion of the impurity NAP as a film component.

The results of this project are very specific, concerning only the crystallization of BZP. They are also very specific to the manner in which the samples were prepared and manipulated. However, slightly different experimental conditions did not lead to very different crystallization behavior. Therefore, the data of this project evidenced definite trends in the crystallization processes of vapor-quenched BZP.

This study has also accomplished the development of a general technique by which optical emission spectroscopy, kinetic modeling, cyclic-annealing, and low temperatures can be used to investigate collectively the microscopic processes

material to crystallization. The ideas used in this thesis can be applied to nearly any disordered solid enabling study of crystallization events on a length scale much less than visible light.

REFERENCE LIST

1. A.P. Alivisatos, M.F. Arndt, S. Efrima, D.H. Waldeck, and C.B. Harris, *J. Chem. Phys.* **86**, 6540 (1987).

2. M. Avrami, *J Chem. Phys.*, **7**, 1103 (1939).

3. M. Avrami, *J. Chem. Phys.*, **8**, 212 (1940).

4. H. Bässler, *Phys. Stat. Sol. (b)*, **107**, 9 (1981).

5. J. Blazević and J. Colombo, *J. Ram. Spect.*, **11**, 143 (1981).

6. A. Blumen and R. Silbey, *J. Chem. Phys.*, **70**, 3707 (1979).

7. A. Blumen and J. Manz, *J. Chem. Phys.*, **71**, 4694 (1979).

8. A. Blumen, *Il Nuovo Cimento*, **63**, 50 (1981).

9. A. Blumen, J. Klafter and G. Zumofen, *Phys. Rev. B.*, **28**, 6112 (1983).

10. D. P. Craig and S. H. Walmsley, <u>*Excitons in Molecular Crystals*</u> (W. A. Benjamin, Inc., NY, 1968).

11. D. L. Dexter, *J. Chem. Phys.*, **21**, 836 (1953).

12. S. Dym, R.M. Hochstrasser and M. Schafer, *J. Chem. Phys.*, **48**, 646 (1968).

13. R. Eiermann, G.M. Pareinson, H. Bässler, and J.M. Thomas, *J. Chem. Phys.*, **87**, 544 (1983).

14. U.R. Evans, Trans. Faraday Soc., **41**, 365 (1945).

15. U. Even, K. Rademann, J. Jortner, N. Manor, and R. Reisfeld, *Phys. Rev. Lett.*, **52**, 2164 (1984).

16. W. Feller, <u>*An Introduction to Probability Theory and Its Applications*</u> (J. Wiley & Sons, Inc., NY, 1957).

17. A.S. Gaevskii, V.G. Roskolodko, and A.N. Faidysh, *Soviet Phys.- Optics and Spectroscopy*, **22**, 124 (1967).

18. D.J. Graham, *J. Phys. Chem.*, **95**, 993 (1991).

19. D.J. Graham and D.L. LaBrake, *J. Phys. Chem.*, **95**, 997 (1991).

20. L.A. Harmon and R. Kopelman, *J. Lumin.*, **31/32**, 660 (1984).

21. L.A. Harmon, Ph.D. Dissertation, The University of Michigan, 1985.

22. L.A. Harmon and R. Kopelman, *J. Phys. Chem.*, **94**, 3454 (1990).

23. R. M. Hochstrasser, *J. Chem. Phys.*, **39**, 3153 (1963).

24. T.F. Hunter, R.D. McAlpine, and M. Hochstrasser, *J. Chem Phys.*, **50**, 1140 (1969).

25. K. A. Jackson, D.R. Uhlmann and J.D. Hunt, *J. Crystal Growth*, **1**, 1 (1967).

26. K. A. Jackson, *J. Crystal Growth*, **24/25**, 130 (1974).

27. R. Jankowlak, K.D. Rockwitz, and H. Bässler, *J. Chem. Phys.*, **87**, 552 (1983).

28. Y. Kamura, K. Seki, and H. Inokuchi *Chem. Phys. Lett.*, **30**, 35 (1975).

29. Y. Kamura, I. Shirotani, K. Ohno, K. Seki, and H. Inokuchi, *Bull. Chem. Soc. Japan*, **49**, 418 (1976).

30. J. Klafter and A. Blumen, *J. Chem. Phys.*, **80**, 875 (1984).

31. P. W. Klymko and R. Kopelman, *J. Phys. Chem.*, **87**, 4565 (1983).

32. S.-K. Kook and D.M. Hanson *Chem. Phys.*, **146**, 303 (1990).

33. R. Kopelman, in *Radiationless Processes in Molecules and Condensed Phases*, edited by F.R. Fong, *Topics in Applied Physics,* Vol **5** (Springer, Berlin, 1976).

34. R. Kopelman and P. Argyrakis, *J. Chem. Phys.*, **72**, 3053 (1980).

35. R. Kopelman, *J. Stat. Phys.*, **42**, 185 (1986).

36. Y. Maruyama, T. Iwaki, T. Kajiwara, I. Shirotani, and H. Inokuchi, *Bull. Chem. Soc. Japan*, **43**, 185 (1986)

37. McClure and Hanst, *J. Chem. Phys.*, **23**, 1772 (1955).

38. E. W. Montroll and G. H. Weiss, *J. Math. Phys.*, **6**, 167 (1965).

39. H. Müller, H. Bässler, and G. Vaubel, *Chem. Phys. Lett.* **29**, 102 (1974).

40. L.M. Peter and G. Vaubel, *Phys. Stat. Sol. (b)*, **58**, 593 (1973).

41. D. Pines and D. Huppert, *J. Chem. Phys.,* **91**, 7291 (1989).

42. R. Richert and H. Bässler, *Chem. Phys. Lett.*, **118**, 235 (1985).

43. R. Richert, *Chem. Phys. Lett* **118**, 534 (1985).

44. R. Richert and H. Bässler, *J. Chem. Phys.*, **84**, 3567 (1986).

45. H. Scher and E. W. Montroll, *Phys. Rev. B.*, **12**, 2455 (1975).

46. G. Schönherr, R. Eiermann, H. Bässler, and M. Silver, *Chem. Phys.*, **52**, 287 (1980).

47. H. Seki and U. Itoh, *J. Chem. Phys.*, **72**, 2166 (1980).

48. M.F. Shlesinger and E.W. Montroll, *Proc. Natl. Acad. Sci. USA.*, **81**, 1280 (1984).

49. N. J. Tro, A. M. Nishimura and S. M. George, *J. Vac. Sci. Technol.*, **A 6**, 852 (1988).

50. N.J. Tro, A.M. Nishimura, and S.M. George, *J. Phys. Chem.*, **93**, 3276 (1989).

51. N.J. Tro, A.M. Nishimura, D.R. Haynes and S.M. George, *Surface Sci.*, **207**, L961 (1989).

52. Y. Udagawa, T. Azumi, M. Ito and S. Nagakura, *J. Chem. Phys.*, **49**, 3764 (1968).

53. C. von Borczyskowski and T. Kirski, *Phys. Rev. Let.*, **60**, 1578 (1988).

54. C. von Borczyskowski and T. Kirski, *Phys. Rev. B.*, **40**, 11335 (1989).

55. C. von Borczyskowski and T. Kirski, *Ber. Bunsenges. Phys. Chem.*, **93**, 1373 (1989).

56. K.-M. Weitzel and H. Bässler, *J. Chem. Phys.*, **84**, 1590 (1986).

57. G. Zumofen and A. Blumen, *Chem. Phys. Lett.*, **88**, 63 (1982).

58. G. Zumofen and A. Blumen, *Chem. Phys. Lett.*, **98**, 393 (1983).

DISSERTATION APPROVAL SHEET

The dissertation submitted by Dwayne L. LaBrake has been read and approved by the following committee:

Dr. Daniel J. Graham, Director
Assistant Professor, Chemistry
Loyola University of Chicago

Dr. Patrick Henry
Professor, Chemistry
Loyola University of Chicago

Dr. Charles Brodbeck
Professor, Physics
Loyola University of Chicago

Dr. Ronald A. Lovett
Professor, Chemistry
Washington University, St. Louis

The final copies have been examined by the director of the dissertation and the signature which appears below verifies the fact that any necessary changes have been incorporated and that the dissertation is now given final approval by the Committee with reference to content and form.

The dissertation is, therefore, accepted in partial fulfillment of the requirements for the degree of Ph.D.

12-10-91
_____   _____
        Date   Director's Signature